Eberhard Karls Universität Tübingen
Kepler Center for Astro and Particle Physics
and
GSI Helmholtzzentrum für Schwerionenforschung
Compressed Baryonic Matter Experiment
Darmstadt, Germany

Master's Thesis

Master of Science Astro and Particle Physics

October 1, 2025

The Assembly and Integration of a Half-unit of the Silicon Tracking System(STS) Detector

Gnana Sindhu Subramanya

Eberhard Karls Universität Tübingen
Kepler Center for Astro and Particle Physics
and
GSI Helmholtzzentrum für Schwerionenforschung
Compressed Baryonic Matter Experiment
Darmstadt, Germany

Master's Thesis

Master of Science in Astro and Particle Physics

October 1, 2025

The Assembly and Integration of a Half-Unit of the Silicon Tracking System(STS) Detector

Author:	Gnana Sindhu Subramanya
Matriculation No.:	6637976
Supervisor:	Prof. Dr. Hans Rudolf Schmidt
Secondary Supervisor:	Prof. Dr. Alberica Toia
Submission Date:	October 1, 2025

Declaration of Originality

Hereby I confirm, _____ Matr. Nr. _____,
that this assignment is my own work and that I have only sought and used mentioned tools. I have clearly referenced in the text and the bibliography all sources used in the work (printed sources, internet or any other source), including verbatim citations or paraphrases. I am aware of the fact that plagiarism is an attempt to deceit which, in case of recurrence, can result in a loss of test authorization. Furthermore, I confirm that neither this work nor parts of it have been previously, or concurrently, used as an exam work neither for other courses nor within other exam processes.

Place and date: _____ Signature: _____

Abstract

The Compressed Baryonic Matter (CBM) experiment at the Facility for Antiproton and Ion Research (FAIR) is designed to investigate the properties of strongly interacting matter at high net-baryon densities. A key component of the experiment is the Silicon Tracking System (STS), which provides high-precision tracking of charged particles produced in heavy-ion collisions. High reconstruction efficiency and vertex resolution of the STS are essential for rare probe measurements, such as open charm and di-leptons, directly linking detector performance to the core physics goals of CBM. Therefore, ensuring the proper assembly and integration of STS units is critical for the overall performance of the experiment.

This thesis focuses on the STS half-unit, aiming to develop, implement, and verify a reliable assembly and integration protocol. The protocol ensures precise placement of all parts, including ladders with mounted Front-End Board (FEB) boxes and peripheral electronic components. Prototype components were used to simulate assembly procedures, allowing safe handling before working with actual sensor modules and electronics. The key phase of the study was verification of the cable routing, which involved configuring data and power connections between FEBs and the readout chain and ensuring proper alignment with the assembly layout. Special attention was given to the mechanical constraints of the half-unit, verifying that cable bends and routing paths did not interfere with module assembly or with future integration into the full STS system. This work represents the first verification of a half-unit assembly protocol, with validation of functional tests of the FEB boxes.

Functional tests of the modules were carried out by performing configuration of the front-end ASICs (Application-Specific Integrated Circuits) mounted on the FEBs. These tests confirmed stable Equivalent noise charge (ENC) values within the expected range and thermal stability under operation, ensuring that signals could be accurately transmitted and received without degradation. The impact of pre-bent and routed cables on signal noise was evaluated, and test protocols confirmed that the current routing did not compromise electronic performance.

Thermal tests were also performed to assess the stability of the ASICs under operating conditions, verifying that the heat dissipation from them remained within safe limits and did not affect the performance. This evaluation is essential for identifying possible operational challenges and avoiding damage during long data-taking periods.

In addition to assembly and functional verification, this work provides a foundation for further optimization of the integration protocol. While the preliminary results indicate that the assembly and routing procedures are effective, additional studies are planned to evaluate the system under extended operational conditions and to confirm long-term reliability. The outcomes of this work contribute to the overall preparation of the STS half-units for integration into the CBM experiment, ensuring that the modules meet the required standards for performance and stability.

By establishing and testing a detailed protocol using prototype components, this study provides an important step towards streamlining the assembly and integration of STS half-units. It reduces the risk of errors during future assembly and validates the operational procedures of the CBM detector. The methodology and results presented here can also guide future integration with complete detector modules and support ongoing efforts to optimize the STS within the CBM experiment.

Kurzfassung

Das Compressed Baryonic Matter (CBM)-Experiment an der Facility for Antiproton and Ion Research (FAIR) ist darauf ausgelegt, die Eigenschaften von stark wechselwirkender Materie bei hohen Netto-Baryonendichten zu untersuchen. Ein zentraler Bestandteil des Experiments ist das Silicon Tracking System (STS), das eine hochpräzise Verfolgung geladener Teilchen ermöglicht, die in Schwerionenkollisionen erzeugt werden. Eine hohe Rekonstruktions-Effizienz und Vertex-Auflösung des STS sind entscheidend für Messungen seltener Sonden wie offenen Charm und Di-Leptonen, wodurch die Detektorleistung direkt mit den Kernphysik-Zielen von CBM verknüpft wird. Daher ist die Sicherstellung der ordnungsgemäßen Montage und Integration der STS-Einheiten entscheidend für die Gesamtleistung des Experiments.

Diese Arbeit konzentriert sich auf die STS-Halbeinheit und hat zum Ziel, ein zuverlässiges Montage- und Integrationsprotokoll zu entwickeln, umzusetzen und zu verifizieren. Das Protokoll gewährleistet die präzise Platzierung aller Teile, einschließlich der Leiterbahnen mit montierten Front-End-Board-(FEB)-Boxen und peripheren elektronischen Komponenten. Prototyp-Komponenten wurden verwendet, um Montageverfahren zu simulieren, sodass ein sicheres Arbeiten möglich war, bevor mit den tatsächlichen Sensormodulen und der Elektronik gearbeitet wurde. Die Schlüsselphase der Studie war die Überprüfung der Kabelführung, die das Konfigurieren der Daten- und Stromverbindungen zwischen FEBs und der Auslesekette sowie die Sicherstellung der richtigen Ausrichtung mit dem Montageplan umfasste. Besonderes Augenmerk wurde auf die mechanischen Einschränkungen der Halbeinheit gelegt, um sicherzustellen, dass Kabelbiegungen und -verläufe weder die Montage der Module noch die zukünftige Integration in das vollständige STS-System beeinträchtigen. Diese Arbeit stellt die erste Verifizierung eines Montageprotokolls für die

Halbeinheit dar, einschließlich der Validierung der Funktionstests der FEB-Boxen.

Funktionstests der Module wurden durchgeführt, indem die Front-End-ASICs (Application-Specific Integrated Circuits), die auf den FEBs montiert sind, konfiguriert wurden. Diese Tests bestätigten stabile Werte der äquivalenten Rauschladung (ENC) im erwarteten Bereich sowie thermische Stabilität im Betrieb, wodurch sichergestellt wurde, dass Signale genau übertragen und empfangen werden können, ohne dass es zu Beeinträchtigungen kommt. Die Auswirkung der vorgebogenen und verlegten Kabel auf das Signalrauschen wurde bewertet, und die Testprotokolle bestätigten, dass die aktuelle Kabelführung die elektronische Leistung nicht beeinträchtigt.

Thermische Tests wurden ebenfalls durchgeführt, um die Stabilität der ASICs unter Betriebsbedingungen zu bewerten und zu überprüfen, dass die Wärmeabfuhr innerhalb sicherer Grenzen bleibt und die Leistung nicht beeinträchtigt. Diese Bewertung ist entscheidend, um mögliche betriebliche Herausforderungen zu identifizieren und Schäden während längerer Datenerfassungsperioden zu vermeiden.

Zusätzlich zur Montage- und Funktionsüberprüfung bildet diese Arbeit eine Grundlage für die weitere Optimierung des Integrationsprotokolls. Während die vorläufigen Ergebnisse darauf hindeuten, dass die Montage- und Kabelführungsverfahren effektiv sind, sind weitere Studien geplant, um das System unter längeren Betriebsbedingungen zu evaluieren und die Langzeitzuverlässigkeit zu bestätigen. Die Ergebnisse dieser Arbeit tragen zur Gesamtvorbereitung der STS-Halbeinheiten für die Integration in das CBM-Experiment bei und stellen sicher, dass die Module die erforderlichen Standards in Bezug auf Leistung und Stabilität erfüllen.

Durch die Erstellung und Prüfung eines detaillierten Protokolls mit Prototyp-Komponenten liefert diese Studie einen wichtigen Schritt zur Optimierung der Montage und Integration der STS-Halbeinheiten. Die hier vorgestellte Methodik und die Ergebnisse können auch die zukünftige Integration mit vollständigen Detektormodulen leiten und die laufenden Bemühungen zur Optimierung des STS innerhalb des CBM-Experiments unterstützen.

Acknowledgements

This thesis has been a journey of learning, patience, and determination, and I owe my gratitude to many people who have guided, supported, and encouraged me along the way.

First and foremost, I would like to express my sincere thanks to Prof. Dr. Hans Rudolf Schmidt for his constant guidance and support throughout this work. I am equally grateful to Dr. Maksym Teklishyn, whose insights and encouragement helped me grow not only as a researcher but also in the way I approach problems with curiosity and discipline. I would also like to thank Prof. Dr. Alberica Toia, Dr. Jörg Lehnert, Dr. Adrian Rodríguez Rodríguez, Lady Maryann Collazo Sanchez, Anju Sharma, Patryk Semeniuk, and Dairon Rodríguez Garces for their explanations and technical advice, which were invaluable at every stage of this work. Their patience and willingness to discuss even the smallest details helped me understand things more deeply. Thank you all for adding warmth and laughter to everyday work life. The coffee breaks, random conversations, and moral support during stressful days made everything lighter.

I would also like to thank the entire CBM group at GSI Helmholtzzentrum für Schwerionenforschung for creating an inspiring and supportive environment. It has been a privilege to work alongside people whose dedication and precision constantly set high standards. The discussions in the lab, the troubleshooting sessions, and the quiet teamwork during the half-unit assembly and functional tests taught me lessons that went far beyond what I could learn from books. My heartfelt thanks go to Oleg Vas, who provided guidance and hands-on support during the practical stages of integration, from aligning components to verifying connections. Every shared moment, from solving issues together to celebrating small victories, made this experience deeply meaningful.

To my friends Chaitanya, Pablo, Lucia, and my friends from Steinhaus, your encouragement meant more than you know. You reminded me that I was never alone, no matter the distance. A very special thank you goes to Sharath Savasere for being my calm through every uncertainty. Your patience, faith, and quiet reassurance gave me strength whenever I doubted myself. Thank you for listening to endless stories about detectors, for celebrating small milestones, and for simply being there in every way that mattered.

To my family, I express my deepest gratitude and love. To my parents, thank you for believing in me even when I doubted myself, for your sacrifices, and for the constant love that has carried me through every phase of life. To my grandparents, whose blessings and gentle wisdom I still feel, I owe much of who I am to you.

I am truly grateful to everyone who has been part of this journey. Your guidance, support, and encouragement have made this thesis possible and this experience unforgettable, and have made it truly worthwhile.

A quote that has stayed with me from one of my favorite books, What You Are Looking for is in the Library by Michiko Aoyama, reflects my experience throughout this thesis: *"Life is one revelation after another. Things don't always go to plan, no matter what your circumstances. But the flip side is all the unexpected, wonderful things that you could never have imagined happening."* Each challenge during this work brought unexpected insights and personal growth.

List of Tables

List of Figures

Contents

1 Introduction

What is matter made of at its deepest level? What forces shaped the early universe? Can we recreate the conditions of the universe's first moments here on Earth? These questions lie at the heart of particle physics, a field dedicated to understanding the most fundamental constituents of matter and the rules that govern their interactions. Particle physics is devoted to exploring the smallest building blocks of nature. At its core, it seeks to uncover what matter is made of, how it behaves at the tiniest scales, and what hidden principles underlie its structure. The fundamental particles are described by the Standard Model, a powerful theoretical framework that has withstood decades of experimental testing. However, the Standard Model is incomplete, and new particles or interactions are expected to lie beyond its current scope. The early universe provides a unique natural laboratory beyond the capabilities of particle accelerators, where extreme temperatures and densities allowed for interactions and phenomena far beyond the reach of current experiments. In the moments following the Big Bang, the universe was in a state of unimaginable temperature and density that allowed particles and forces to behave in ways we cannot observe today. In this early phase, the universe was filled with a hot, dense plasma of fundamental particles: quarks, gluons, electrons, positrons, photons, neutrinos, and their antiparticles, all interacting frequently and existing in thermal equilibrium. As the universe expanded, it cooled, and the intensity of these interactions diminished. This cooling triggered several key transitions in the universe: quarks began to confine into hadrons, protons and neutrons combined to form light nuclei, and eventually neutral atoms began to form as electrons bound with nuclei. These events transformed the universe from a chaotic plasma of elementary particles into a structured medium capable of forming matter as we know it. Modern experiments in heavy-ion collisions aim to recreate similar energy densities in the laboratory, allowing us to explore phases of matter such as the quark-gluon plasma and test theoretical models of high-energy interactions.

1.1 Elementary Particles and the Forces they Mediate

The Standard Model (SM) stands as the most theoretically verified theory for describing the fundamental particles and their interactions, with the exception of gravity. Figure 1.1.1 provides an overview of the seventeen particles included in the SM, with twelve fermions and five bosons. Greek and Latin symbols are used to represent these particles.

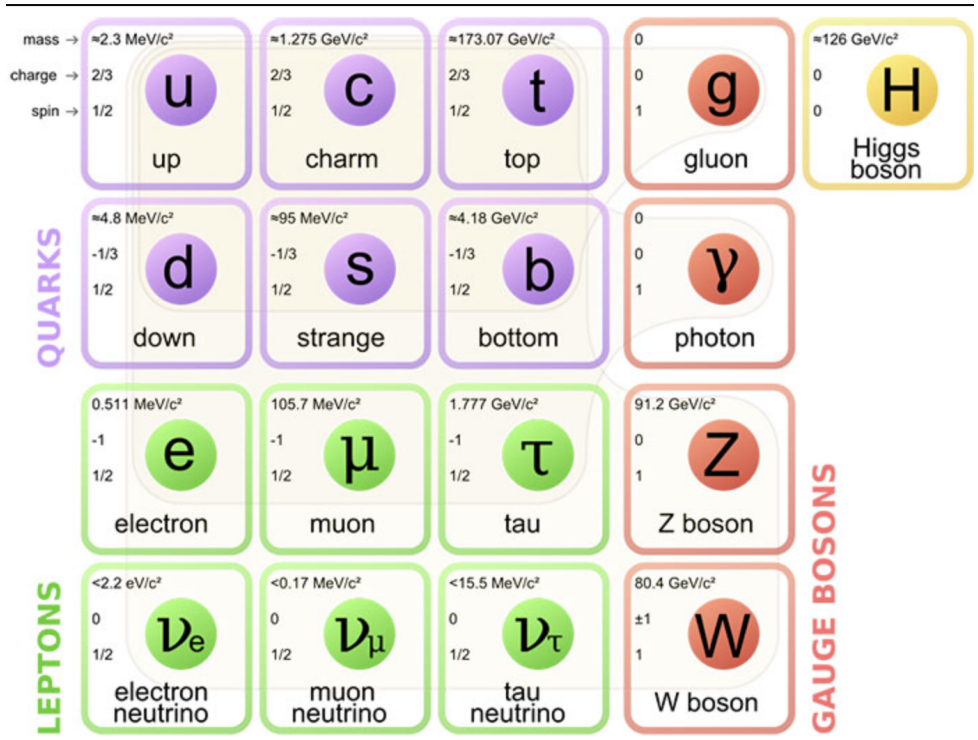

Figure 1.1.1: Overview of the Standard Model of particle physics. (Courtesy of [1])

At its core, the Standard Model classifies elementary particles into two main categories: fermions make up matter, and bosons mediate the fundamental forces. Fermions follow Fermi-Dirac statistics and obey the Pauli exclusion principle. They are organized into quarks and leptons, each appearing in three generations. The 1st generation, comprising the up and down quarks, the electron, and the electron neutrino, forms the building blocks of ordinary matter.

The 2nd and 3rd generations are made up of heavier, unstable particles, which decay rapidly into first generation particles.

The force carriers, or bosons, obey Bose-Einstein statistics. These include the photon, which mediates electromagnetism; the gluons, which mediate the strong force; and the W and Z bosons, which mediate the weak force. These bosons facilitate interactions by being exchanged between matter particles, transferring quantized amounts of energy and momentum.

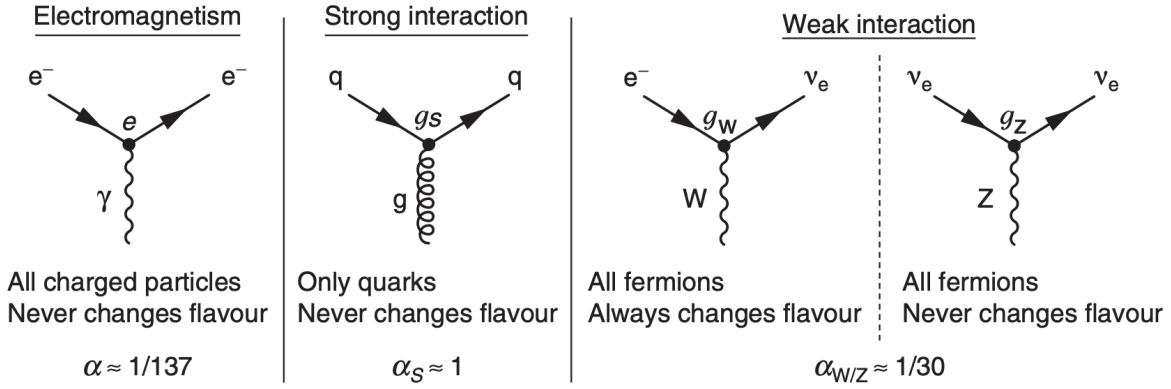

Figure 1.1.2: Feynman diagrams representing fundamental particle interactions via gauge boson exchange. (Courtesy of [2])

Feynman diagrams, shown in figure 1.1.2, provide a visual representation of particle interactions. Each diagram illustrates a three-point vertex involving a gauge boson and incoming and outgoing fermions. For each type of interaction, an associated coupling strength(g) quantifies the interaction's intensity.

1.2 QCD Matter under Extreme Conditions

Quantum field theory provides the framework for describing the strong interaction, one of the four fundamental forces of nature that holds together quarks and gluons into protons, neutrons, and other hadrons. Quarks are characterized by a quantum number known as color charge, which comes in three varieties, commonly labeled red, green, and blue.

Gluons, the mediators of the strong force, also carry color charge in the form of color–anticolor combinations [3].

Unlike the photon in electrodynamics, gluons interact not only with quarks but also with each other. This feature gives rise to the nonlinear structure of Quantum Chromodynamics (QCD) and underlies its confining behavior [4]. The distinguishing characteristic of QCD is asymptotic freedom, where the strength of interaction between quarks and gluons decreases at high energies, allowing them to move nearly freely [5]. In contrast, at low energies, the coupling becomes strong, resulting in confinement, where quarks and gluons are permanently bound within hadrons and cannot be isolated under normal conditions [6]. However, under conditions of extremely high temperature and density, such as those created in ultra-relativistic heavy-ion collisions, shortly after the Big Bang, or in the cores of neutron stars, QCD predicts a transition to a deconfined phase known as the quark-gluon plasma (QGP). In this state, quarks and gluons are no longer bound within hadrons and can move freely across extended volumes [7]. The thermodynamic properties of such deconfined matter can be characterized by an Equation of State, relating pressure, energy density, and other components [8].

Equation of State (EoS)

The Equation of State (EoS) describes how the thermodynamic quantities, such as pressure, density, energy density, and temperature, are related to one another [9]. At the extreme densities found inside neutron stars, the pressure becomes almost independent of temperature and is determined mainly by the mass density and the composition of matter. In such cases, the EoS can be expressed in a simpler form,

$$P = P(\rho).$$

In this way, the EoS captures the underlying physics of dense matter and provides essential input for modeling the structure and behavior of compact stars [10]. This framework is particularly relevant for neutron stars, which provide a unique natural laboratory to study

matter under such extreme conditions. Understanding their structure, mass, and radius through the EoS is crucial before exploring even more exotic phases of matter, such as the Quark-Gluon Plasma [11].

Neutron Stars

Neutron stars (NS) are the dense remains of massive stars that exhaust their nuclear fuel and undergo core-collapse supernova explosions. With typical masses of about 1.4 times the Sun's mass compressed into a radius of only 10–12 km, they are among the densest forms of matter in the universe [12]. Their cores reach densities several times higher than nuclear density, where exotic states such as hyperons, deconfined quarks, or meson condensates may appear [13]. The internal structure of neutron stars is determined by solving the Tolman-Oppenheimer-Volkoff (TOV) equations, which are the relativistic equations of hydrostatic equilibrium:

$$\frac{dP(r)}{dr} = -\frac{G\left[\varepsilon(r) + P(r)\right]\left[M(r) + 4\pi r^3 P(r)\right]}{r\left[r - 2GM(r)\right]} \tag{1}$$

$$\frac{dM(r)}{dr} = 4\pi r^2 \varepsilon(r) \tag{2}$$

Here, $P(r)$ is the pressure, $\varepsilon(r)$ is the energy density, $M(r)$ is the enclosed mass at radius r, and G is the gravitational constant [14]. The relation between pressure and energy density, $P(\varepsilon)$ - the EOS, is needed to solve these equations and predict the mass-radius relationship of neutron stars [15]. Observations such as pulsar timing, X-ray measurements, and gravitational-wave detections from binary neutron star mergers help constrain the EoS, improving our understanding of the composition and behavior of matter at extreme densities [16]. These insights are consistent with results from heavy-ion collision experiments on Earth, helping to advance our knowledge of QCD under extreme conditions [17]

1.3 Phase Diagram of the Quark-Gluon Plasma(QGP)

Protons and neutrons are not indivisible, but are made up of quarks bound together by gluons. These quarks and gluons are fundamental constituents of the SM, each carrying a distinct property called color charge [18]. The strong nuclear force, carried by gluons, binds quarks together and is far stronger than gravity, electromagnetism, or the weak force at the subatomic scale. This strength explains why quarks cannot normally be separated; they are permanently confined inside composite particles such as protons, neutrons, and other hadrons [18]. However, under extreme conditions of temperature and density, quark confinement can be overcome. When nucleons melt in the dense and hot environment, their components become free to move, producing a new state of matter known as the quark-gluon plasma (QGP). These conditions existed naturally just a few microseconds after the Big Bang, when the universe was sufficiently hot and dense for quarks and gluons to move freely [19,20].

Figure 1.3.1 represents matter existing as a hadron gas at low temperature and baryon chemical potential, while at high temperature it forms a deconfined quark–gluon plasma [21]. The crossover transition at low (μB) potential (T $\approx$ 155 MeV) is supported by lattice QCD, while at higher baryon chemical potential, a first-order phase transition and a critical point are hypothesized but not yet confirmed experimentally. Different heavy-ion facilities probe complementary regions of the phase diagram: the LHC and RHIC focus on high temperature and low (μB), while FAIR and Nuclotron-based Ion Collider fAcility (NICA) target the high-density regime [21].

To investigate these questions, relativistic heavy-ion collision experiments aim to recreate similar conditions on Earth. High-energy facilities such as the Relativistic Heavy Ion Collider (RHIC) at Brookhaven [22] and the Large Hadron Collider (LHC) at CERN [23] probe matter at very high temperatures and low baryon density, ideal for studying crossover behavior and QGP properties. In contrast, recently constructed facilities such as NICA in Dubna [24] and the CBM experiment at FAIR in Darmstadt [25] are designed

to probe regions of higher baryon density, providing fresh insights into the QCD phase diagram at high (μB) [25].

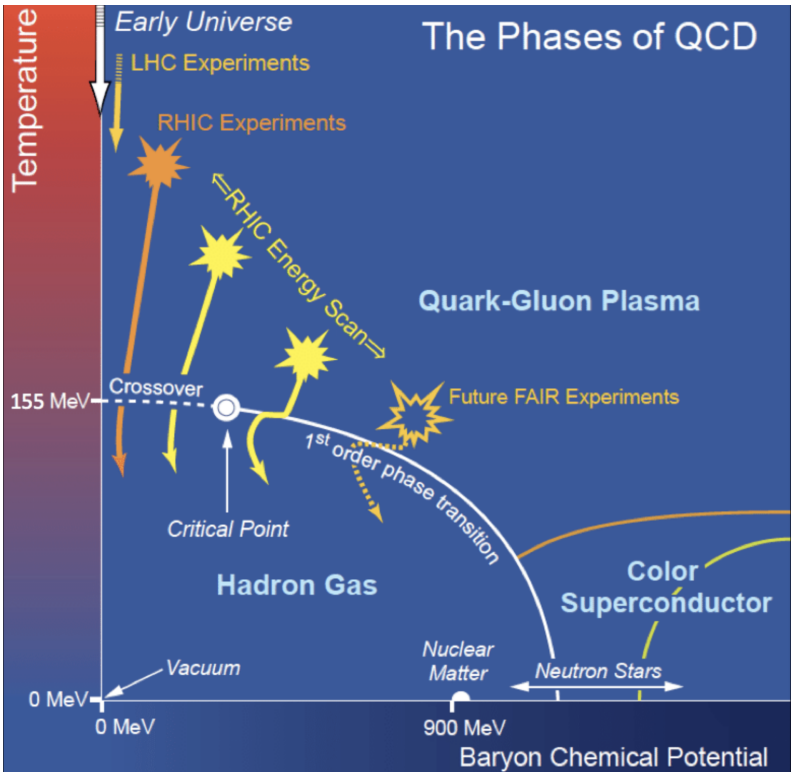

Figure 1.3.1: Shows the phases of strongly interacting matter as a function of temperature T and baryon chemical potential (μB). (Courtesy of [21])

Experiment	Beam Energy / $\sqrt{s_{NN}}$	Mode	Transition Region
CBM (FAIR, Darmstadt)	2–11 AGeV (Au ions, SIS100 fixed-target)	Fixed-target	1st order transition, critical point, high μ_B
RHIC (Brookhaven)	$\sqrt{s_{NN}}$ = 7.7–200 GeV	Collider	Crossover at low μ_B, search for critical point
LHC (CERN, Pb–Pb)	$\sqrt{s_{NN}}$ = 5.02 TeV per nucleon pair	Collider	High T, low μ_B; crossover
NICA (Dubna, MPD)	$\sqrt{s_{NN}} \approx$ 3–9 GeV	Collider / hybrid	High μ_B; 1st-order transition; critical point

Table 1: Heavy-Ion Facilities and QGP Studies (Courtesy [26,27])

Table 1 summarizes the beam energies and the types of QCD transitions explored by these experiments. Collectively, these facilities provide broad coverage of the QCD phase diagram, enabling detailed studies of QGP formation, phase transitions, and the properties of strongly interacting matter.

1.4 Physics Goals of the CBM Experiment

To achieve its objectives, CBM utilizes heavy-ion collisions, such as Au+Au at beam energies in the range of 2-11 AGeV provided by the SIS-100 accelerator at FAIR. This energy regime is particularly suited for producing dense baryonic matter at moderate temperatures, allowing the experiment to probe both collective phenomena in the medium and the properties of individual particles emerging from the collision zone. The high interaction rates achievable in CBM enable the study of rare probes that carry crucial information about the early and dense stages of the collision [28]. To explore these extreme conditions in detail, CBM examines these rare particles that reveal different aspects of the dense matter created in the collisions.

Study of Di-Leptons

One of the primary probes of interest is the study of di-leptons, including electron-positron and muon–antimuon pairs. Di-leptons interact only electromagnetically and thus pass through the medium largely unaffected, providing a clean signal of the high-density conditions. CBM aims to investigate the in-medium modifications of vector mesons (ρ, ω, ϕ), which can reveal how the properties of hadrons change in dense nuclear matter [28,29]. Furthermore, di-lepton measurements provide access to thermal radiation from the medium, helping to characterize the temperature and evolution of the system, as shown in figure 1.4.1 [29].

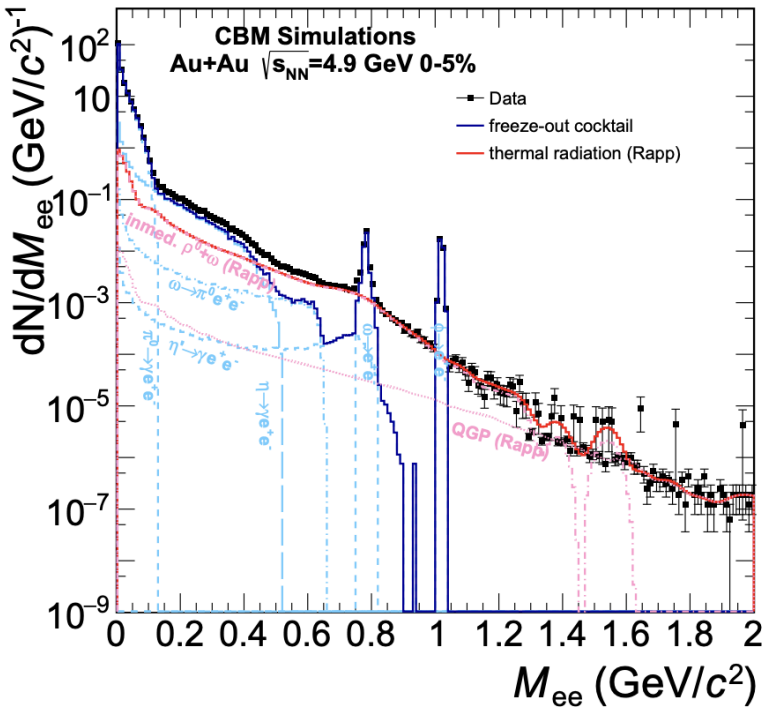

Figure 1.4.1: Highlighting the contributions from individual meson decays (blue) and thermal radiation components (red), the dielectron spectrum for central Au+Au collisions at $\sqrt{s} = 4.9$ GeV is predicted. (Courtesy of [31])

Study of open and hidden charm

Another major focus of CBM is the production of both open charm (D mesons) and hidden charm (charmonium states such as J/ψ). Charm hadrons are produced rarely in heavy-ion collisions, but their behavior is highly sensitive to the medium. By analyzing production rates, momentum distributions, and suppression patterns of charm particles, CBM can probe the properties of dense nuclear matter and search for signatures of de-confinement or QCD phase transitions in the high-density regime [28,30].

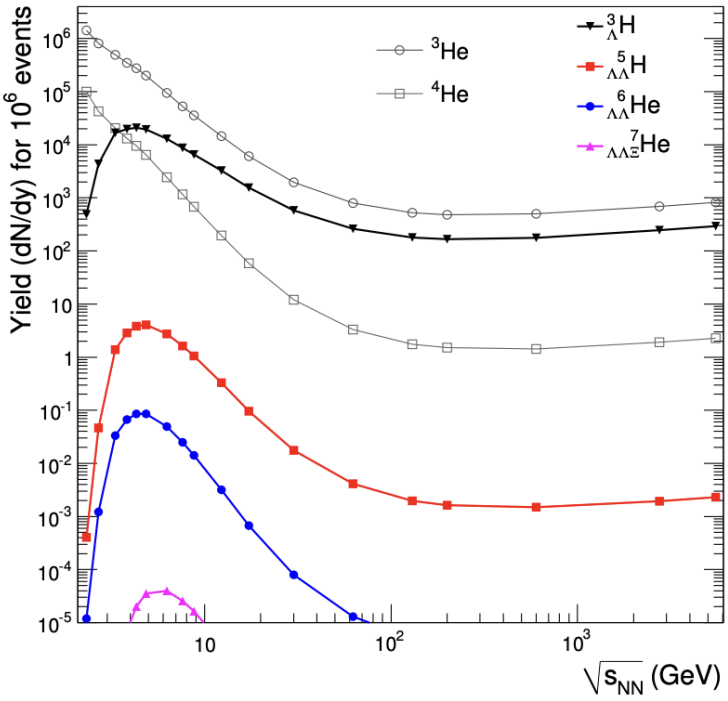

Figure 1.4.2: The thermal model predicting strange particle production in Au+Au collisions. (Courtesy of [28])

Study of Strangeness and Hypernuclei

Another important aspect of CBM is the study of strangeness and hypernuclei. Strange quarks, that are absent in ordinary nuclear matter, appear in collisions as strange and multi-strange baryons (Λ, Ξ, Ω), providing insight into the dynamics of dense matter and equilibration processes. Hypernuclei, particularly those containing double Λ hyperons, allow the study of hyperon-nucleon and hyperon-hyperon interactions, which are essential for understanding the structure of neutron stars and the so called hyperon puzzle [31]. By measuring decay patterns, and interactions as shown in figure 1.4.2, CBM investigates exotic degrees of freedom and the role of strangeness in high-density QCD matter.

2 Overview of the Facility for Antiproton and Ion Research (FAIR)

The Facility for Antiproton and Ion Research (FAIR) is one of the most advanced accelerator facilities, located in Darmstadt, Germany, designed to explore the fundamental properties of matter under extreme conditions [32,33]. Constructed as an extension of the existing GSI Helmholtz Centre for Heavy Ion Research, FAIR integrates a new high-performance accelerator complex with the extensively developed GSI infrastructure [32]. At the heart of FAIR's accelerator lies the SIS100 synchrotron, a superconducting accelerator ring with a circumference of approximately 1,100 m [32,34].

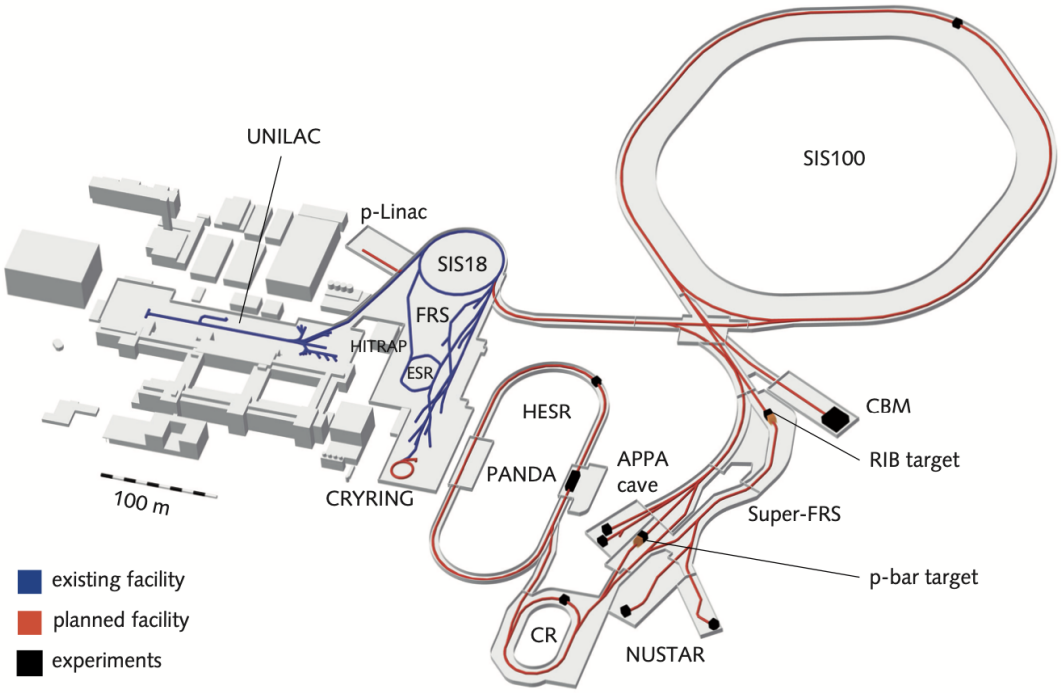

Figure 2.0.1: Overview highlighting the SIS100 synchrotron, which provides high intensity beams from the existing GSI campus (blue) to the CBM experiment in the planned FAIR facility (red). (Courtesy of GSI/FAIR Darmstadt)

It receives beams from the SIS18 synchrotron, which serves as its injector, and is capable of accelerating heavy ions to energies of up to 11 GeV per nucleon and protons up to 30 GeV [33,35]. FAIR will use beams from the SIS100 synchrotron, including protons up to 29 GeV, gold ions up to 11 AGeV, and nuclei with Z/A = 0.5 up to 14 AGeV. In the future, the facility might be extended with the SIS300 synchrotron, which will accelerate protons up to 90 GeV, gold ions up to 35 AGeV, and nuclei with Z/A = 0.5 up to 45 AGeV [36]. Figure 2.0.1 shows the schematic layout of the FAIR accelerator, including the SIS18 injector, the SIS100 synchrotron, experimental halls, and beamlines.

The scientific program at FAIR is organized into four major collaborations, each addressing a distinct domain of modern physics [32] :

- **APPA – Atomic physics, Plasma Physics, and Applications.**
- **CBM – Compressed Baryonic Matter experiment, focusing on nuclear matter at high baryon densities.**
- **NuSTAR – NUclear STructure, Astrophysics, and Reactions.**
- **PANDA – AntiProton ANnihilation at DArmstadt, dedicated to hadron physics with antiprotons.**

Once operational, FAIR will deliver high-intensity beams, enabling experiments on heavy elements to investigate dense nuclear matter similar to that found in neutron stars [36].

2.1 The Compressed Baryonic Matter Experiment(CBM)

The Compressed Baryonic Matter (CBM) experiment at FAIR is designed to investigate nuclear matter at extreme densities and aims to explore the part of the QCD phase diagram where a first-order phase transition and the critical endpoint are expected, providing insight into how matter behaves under conditions of very high μB and moderate temperature [36].

CBM is designed to handle extremely high interaction rates,which is essential for studying rare probes such as charm particles, hypernuclei, and multi-strange hadrons, which provide sensitive signals of dense nuclear matter. The experiment features a fixed-target setup, allowing continuous collection of collision events and enabling precision measurements of observables such as particle production, flow patterns, and fluctuations [36,37].

The detector concept is based on fast, radiation hard subsystems arranged in a compact geometry around the target [37]. CBM's electronics are designed for free streaming readout, meaning data are continuously acquired and time stamped without relying on a conventional hardware trigger [38]. This approach allows the system to handle 10^7 events per second, with real-time event reconstruction and selection performed by a high-performance computing system [38]. Such a framework ensures that rare signals are captured efficiently while maintaining precise tracking, vertexing, and particle identification [39].

2.2 Overview of Sub-detectors in the CBM setup

This section provides a detailed description of the various detectors of the CBM experimental setup, highlighting the specific roles each detector plays within the overall system. Figure 2.2.1 illustrates a schematic representation of the major detectors comprising the system [36,40]:

- Beam Monitor detector (BMON): Provides precise reference timing for collisions and continuously monitors the beam profile and stability to ensure accurate and safe measurements.
- Superconducting Magnet: Generates a stable magnetic field to bend he path of a charged particle, for accurate measurement of the momentum.
- Micro Vertex Detector (MVD): Provides high resolution vertex reconstruction close to the interaction point, enabling identification of short lived particles such as D mesons and hyperons.

- Silicon Tracking System (STS): Precisely tracks charged particle trajectories within the magnetic field and reconstructs their momentum. Positioned inside the dipole magnet, the STS is designed to handle high track densities and contributes to vertex reconstruction for heavy ion collisions.

- Ring Imaging Cherenkov (RICH): Identifies electrons by detecting Cherenkov light rings. Electron identification is essential for studying di-lepton production, which probes the early stages of heavy-ion collisions.

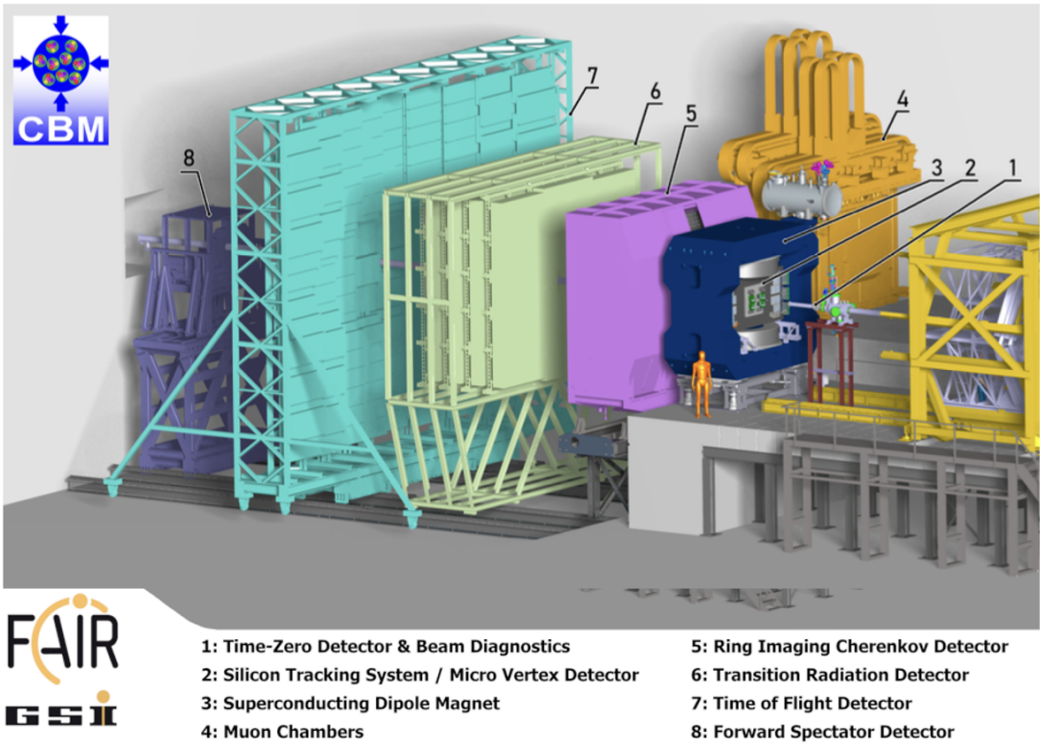

Figure 2.2.1: Overview of the CBM experimental setup illustrating the arrangement of its sub-detectors. (Courtesy of [41])

- Muon Chambers (MUCH): Detects and tracks muons by filtering out other particles using absorber layers. It measures muon pairs from vector meson decays, providing insight into modifications of hadrons.

- Transition Radiation Detector (TRD): Distinguishes electrons from heavier charged particles by detecting transition radiation photons. The TRD complements the RICH in electron identification and improves overall particle identification.

- Time of Flight (ToF): Measures particle flight times to determine velocity, aiding particle identification by separating hadrons such as pions, kaons, and protons.
- Forward Spectator Detector (FSD): Measures the energy of spectator fragments to provide information about the collision geometry and the orientation of the event plane. These measurements allow an evaluation of the nuclear interactions and serve as necessary input for the analysis of collision dynamics.

Beam Monitor (BMON)

The BMON system provides the start time (T_0) for time-of-flight measurements and continuously monitors the beam upstream of the target. It consists of a T_0 station positioned along the beam axis and a halo station positioned slightly to the side of the central beam path, allowing it to monitor the beam halo as shown in figure 2.2.2. Both stations use polycrystalline CVD diamond sensors that are about 1 × 1 cm^2 in size and 70–100 µm thick, with double-sided strip metallization (16 × 16 strips); this allows accurate measurements of both the timing and the position of the beam [42].

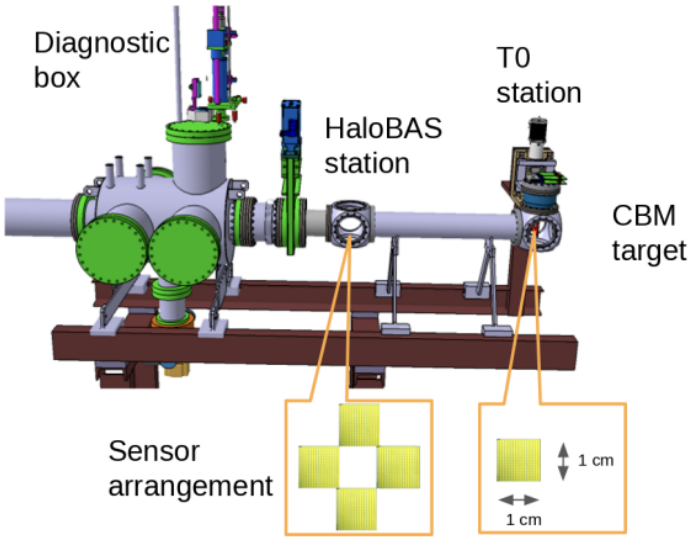

Figure 2.2.2: Schematic of the CBM BMON system with T timing and beam halo monitoring stations. (Courtesy of [42])

The sensors are mounted on motorized supports and can be safely moved away from the beam when required. The signals are amplified by front-end preamplifiers and processed through PreAmplifier Discriminator (PADI) ASICs, which convert the analog signals into digital pulses. These are further digitized by GSI Event-driven Time to Digital Converters (GET4 TDCs) to record precise arrival times. The signals are sent to the main Data Acquisition System (DAQ) for physics measurements and simultaneously to a safety system that monitors the beam [42].

Superconducting dipole magnet

The CBM experiment employs a superconducting dipole magnet with a magnetic power of 1 T · m and an H-type design as shown in figure 2.2.3. It is positioned directly downstream of the target, and the magnet houses the STS and MVD detectors. This configuration allows the detectors to track particle trajectories accurately, identify primary and secondary vertices, and measure particle momenta. The magnet provides a ±25° vertical and ±30° horizontal acceptance, ensuring that particles emitted within these angles are detected [43].

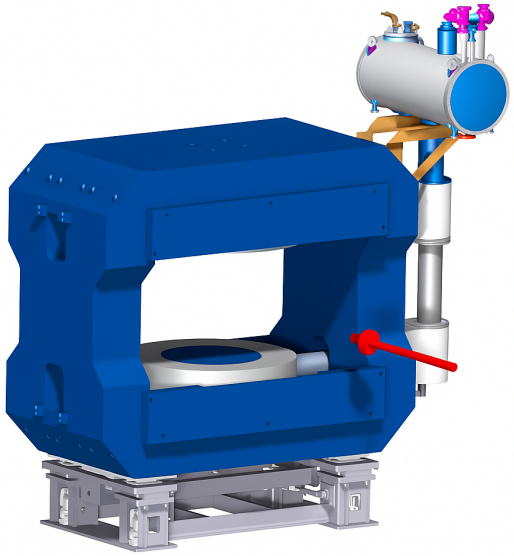

Figure 2.2.3: The Superconducting dipole magnet. (Courtesy of [44])

Micro Vertex Detector (MVD)

MVD, as illustrated in figure 2.2.4, is located inside the superconducting dipole magnet, 5 to 20 cm downstream of the target. Its main purpose is to measure the primary and secondary vertices of particles produced in heavy-ion collisions, particularly short-lived particles such as open charm mesons and hyperons.

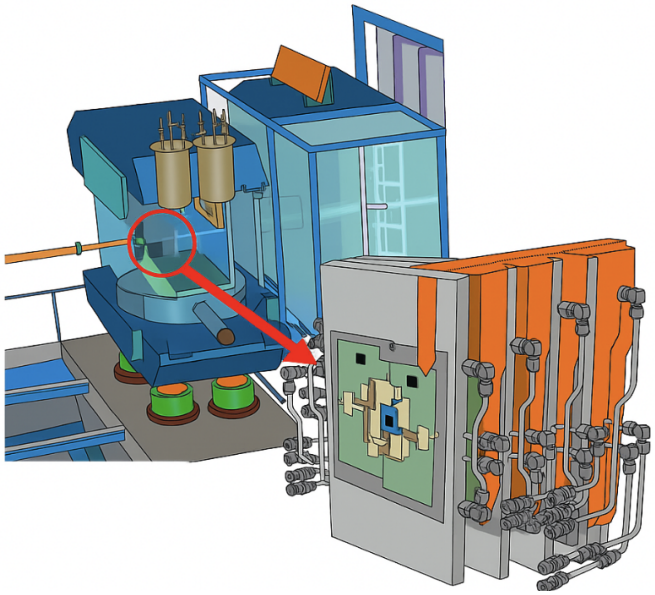

Figure 2.2.4: The MVD inside the superconducting dipole magnet. (Courtesy of [45])

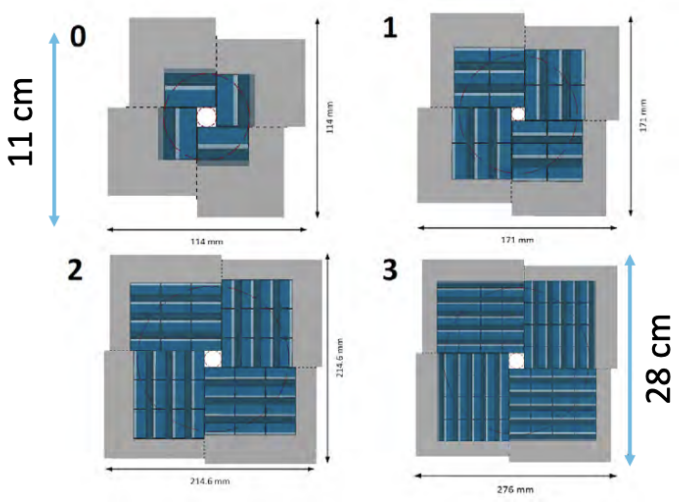

Figure 2.2.5: The four MVD detector stations, and arrangement of MAPS sensors in each station. (Courtesy of [45])

The MVD consists of four stations as seen in figure 2.2.5, with 8, 40, 84, and 160 Monolithic Active Pixel Sensors (MAPS) in stations 1 through 4, respectively, arranged around the beamline [44]. These sensors are crucial for detecting decay vertices of short-lived particles. MAPS provide high spatial resolution, can withstand the high radiation environment, and have a low material budget. These features enable the detector to reconstruct particle trajectories with high precision. [45,46]

Silicon Tracking System (STS)

The Silicon Tracking System (STS), as the central tracking detector in the CBM setup, is placed inside the dipole magnet, where the magnetic field enables precise momentum measurement and plays a key role in reconstructing charged particle trajectories. Further technical details are discussed in Section 3.

Ring Imaging Cherenkov Detector (RICH)

RICH detector, as shown in figure 2.2.6, identifies electrons by detecting Cherenkov radiation, which is emitted at a characteristic angle, forming a ring pattern. Located about 1.6 m downstream of the target, the RICH uses a gaseous radiator, primarily CO_2, and a segmented mirror system coated with aluminum and a thin MgF_2 layer to reflect Cherenkov light onto a plane of Multi-Anode Photomultiplier Tubes (MAPMTs). The MAPMTs' multiple anodes record light at different positions simultaneously, and by analyzing these signals, the detector reconstructs the Cherenkov rings, measures their angles, determines particle velocity, and efficiently separates electrons and positrons from pions and other charged particles [47,48].

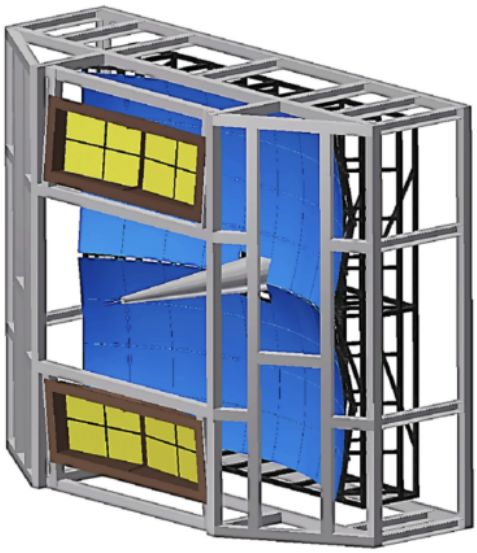

Figure 2.2.6: The RICH detector used for electron identification. (Courtesy of [48])

Muon Chambers System (MUCH)

The MUCH detector as seen in figure 2.2.7, is designed to detect di-muons ($\mu^+\mu^-$) produced in heavy-ion collisions, which are observed when rare probes such as low mass vector mesons (ρ, ω, φ, etc.) decay. The MuCh system consists of five hadron absorber layers, including a 60 cm carbon plate followed by iron plates of 20 cm, 30 cm, 35 cm, and 100 cm thickness, designed to stop most hadrons while allowing muons to pass. The muons are tracked and identified by a combination of absorber layers, Gas Electron Multipliers (GEMs), and multi-gap Resistive Plate Chambers (mRPCs). The system comprises four detector stations. Stations 1 and 2 are equipped with GEMs for precise tracking, while Stations 3 and 4 utilize Resistive Plate Chambers (RPCs) and mRPCs for high-precision timing [49].

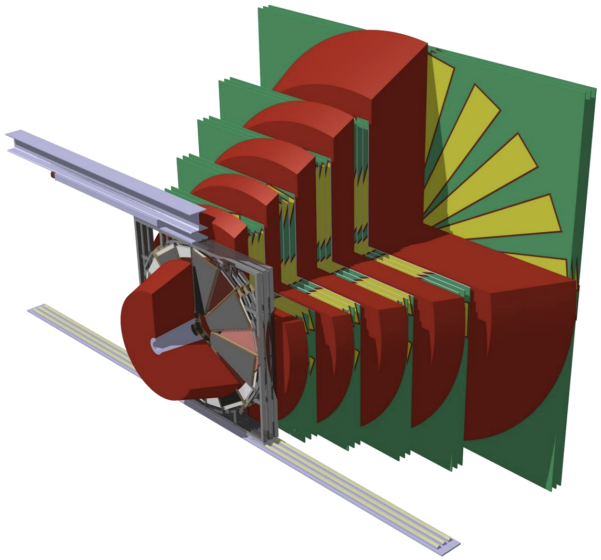

Figure 2.2.7: The MUCH detector designed for di-muon detection. (Courtesy of [49])

Transition Radiation Detector (TRD)

The TRD detector, as seen in figure 2.2.8a, identifies electrons with momenta above 1.5 GeV/c, similar to the capabilities of the RICH detector. It works on the principle of transition radiation, which occurs when a charged particle traverses from one material to another with different dielectric properties. The effect is much stronger for electrons than for heavier particles, so the detector can separate electrons from pions. The TRD uses Multi-Wire Proportional Chambers (MWPCs) in combinations with pad planes to measure particle tracks accurately. It is positioned approximately 4–5 m downstream of the target, after the RICH detector, which increases the chances of identifying higher-momentum electrons [50].

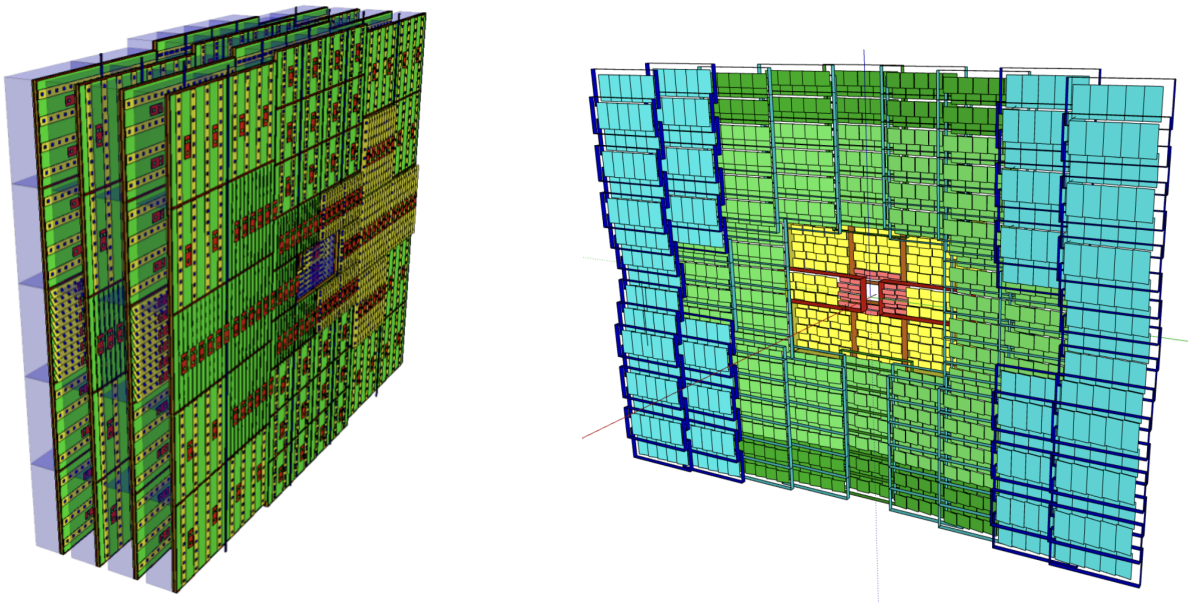

Figure 2.2.8: (a)The TRD detector design (Courtesy of [50 (Left side)); (b)The TOF detector design (Courtesy of [51 (right side)])

Time of flight (TOF)

The TOF detector, as seen in figure 2.2.8b, is positioned approximately 10 m downstream from the target and covers an active area of about 120 m^2. It is used to identify charged particles, mainly hadrons such as pions, kaons, and protons, by measuring their time of flight along with their momentum and track length to determine their mass. The detector is composed of Multi-Gap Resistive Plate Chambers (MRPCs), which provide excellent. time resolution and high detection efficiency, helping in precise particle identification. Particles with the same momentum can have different masses, which causes their times of flight to differ, allowing the TOF detector to distinguish between them [51].

Forward Spectator Detector (FSD)

The FSD, as seen in figure 2.2.9a, measures spectator fragments from heavy-ion collisions to provide information on the collision geometry and the event plane orientation. It is placed downstream of the target along the beam axis, where most spectator fragments travel, and consists of a lead-scintillator calorimeter made up of 44 modules, each measuring 20 $\times$ 20 cm^2, as seen in figure 2.2.9b arranged in a horizontal, elongated layout around the beam. A small central hole in the four central modules allows the main beam of particles to pass through without hitting the detector. The scintillator light in each module is read out by micropixel avalanche photodiodes (MAPDs), and the signals are processed by dedicated front-end electronics integrated with the CBM data acquisition system. Using these measurements, the FSD can estimate the number of participating nucleons, characterize the collision geometry, and determine the orientation of the event plane, providing critical input for the CBM physics [52].

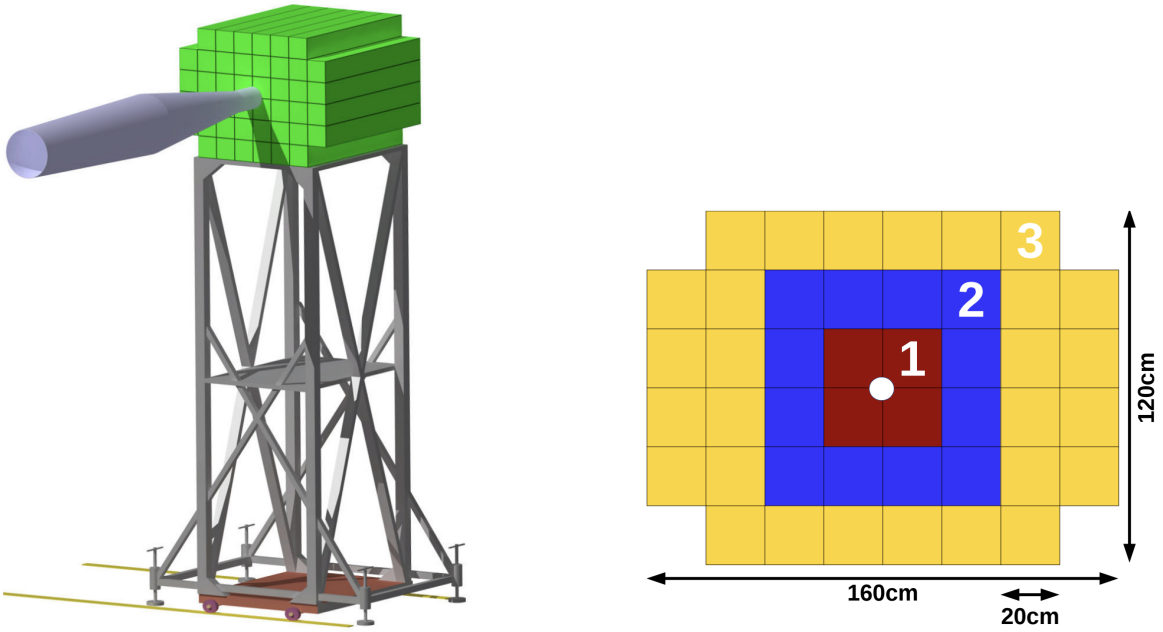

Figure 2.2.9: (a) The PSD detector design (Courtesy of [52]); (b) The modules (Courtesy of [52])

3 Silicon Tracking System (STS)

The Silicon Tracking System (STS) is positioned 30 cm to 100 cm downstream of the fixed target inside the dipole magnet, covering polar angles from approximately 2.5° to 25° as seen in figure 3.0.1, and it serves as the central detector for charged particle tracking. By precisely measuring the curvature of particle trajectories in the magnetic field, the STS achieves a tracking efficiency higher than 95% and a momentum resolution of nearly 1.5% for particles with momenta above 1 GeV/c [53]. This high accuracy is essential for studying short-lived particles, which provide insight into QCD matter at high μB [54,55].

The STS comprises eight tracking stations, as seen in figure 3.0.2. These stations include 20 half-units, comprising 106 ladders that support 896 modules mounted on carbon-fiber (CF) structures. The CF structures provide mechanical support while keeping the material budget low and matching the thermal expansion properties of silicon sensors, minimizing stress from temperature variations [57]. This arrangement ensures precise module alignment and optimal placement for Front-End Boards (FEBs) and cooling systems [55,56]. The STS employs double-sided silicon microstrip sensors (DSMS)(more in Section 4.1.1), which convert particle interactions into measurable electrical signals [57,59]. Each module is connected to FEBs via ultra-thin aluminum-polyimide micro-cables [59]. The FEBs house custom STS-XYTER (STS X and Y coordinate, Time and Energy Read-out chip) ASICs (Application Specific Integrated Circuits), which amplify, shape, and digitize signals from the micro-strip sensors [60,61]. Each ASIC handles 128 input channels with low noise and low power consumption. The system is designed not only for precise momentum measurement but also for timing analysis. The ASICs provide time stamps of nanosecond precision, allowing the detector to differentiate between overlapping events in CBM's continuous, free-streaming data acquisition [55,56,61].

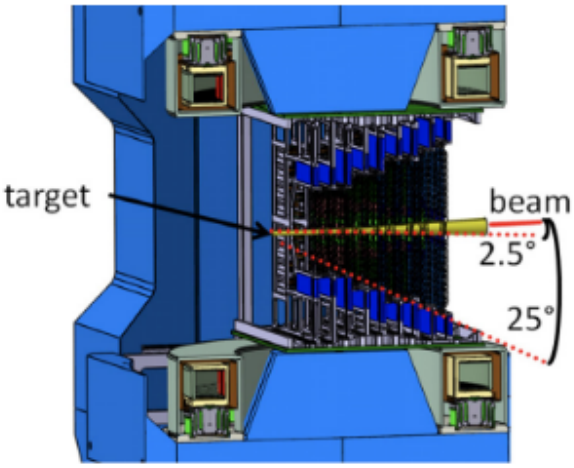

Figure 3.0.1: The STS detector placed inside the dipole magnet. (Courtesy [54])

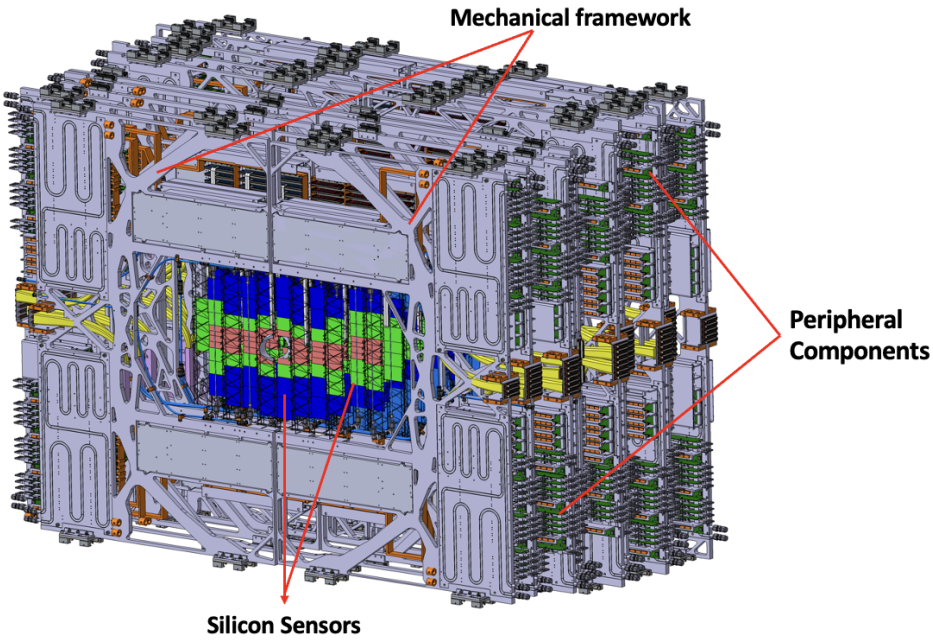

Figure 3.0.2: 8 Tracking stations of STS detector with modules arrangement. (Courtesy of O. Vasylyev (GSI, Darmstadt))

Supporting self triggered, continuous readout at interaction rates of up to 10 MHz, the FEBs generate high data volumes (several gigabytes per second), which are processed by the first-level event selection (FLES) computing system, demonstrating the close integration between the detector and computing infrastructure [55,56,59].

The detector's design is guided by several essential requirements, summarized below in Table 2 [54,55]:

Design Requirement	**Description**
High tracking accuracy	Ensure particle trajectories are reconstructed with high precision, aiming for momentum resolution of about 2% or better.
Minimal material interference	Limit the material in each tracking station to $\leq 1\%$ of a radiation length to reduce scattering and preserve measurement accuracy.
Radiation Hardness	Maintains reliable detector operation under high particle fluxes, and ionizing doses near 1 Mrad without loss of performance [62].
Continuous high-rate readout	Supports continuous self-triggered data at high interaction rates, and is capable of tracking hundreds of particles simultaneously.
Front-end reliability	Guarantee stable performance of electronics under long-term exposure to radiation.
Thermal management	Efficiently removes heat from sensors and electronics to maintain stable operating temperatures and prevent performance degradation [63].

Table 2: Key Design Requirements of the Silicon Tracking System (STS)

The STS units are enclosed in a thermal box that maintains a stable environment by controlling temperature and humidity, preventing condensation that could damage the sensors. Each FEB dissipates a few watts of heat and is mounted on cooling blocks to ensure optimal operating conditions [63]. Overall, the detector dissipates roughly 50 kW of thermal power, mainly from the front-end and readout electronics, with smaller contributions from the sensors and low-voltage data and power cables [59,63], which is effectively removed by a cooling system.[63].

While this section outlines the overall function of the STS, the following chapters will focus specifically on the integration and characterization of the STS half-unit, detailing mechanical assembly and performance assessments carried out during prototyping and full-scale mock-up phases.

4 Modules and Ladders as a Functional Unit

Building upon the general design of the STS, this section provides a detailed examination of its fundamental structural units: The modules and ladders.

4.1 STS Detector Module

The module, as seen in figure 4.1.1, is the fundamental building block of the STS detector, comprising two FEBs connected via ultra-thin microcables. Each FEB hosts eight ASICs that are connected to the strip sensors.

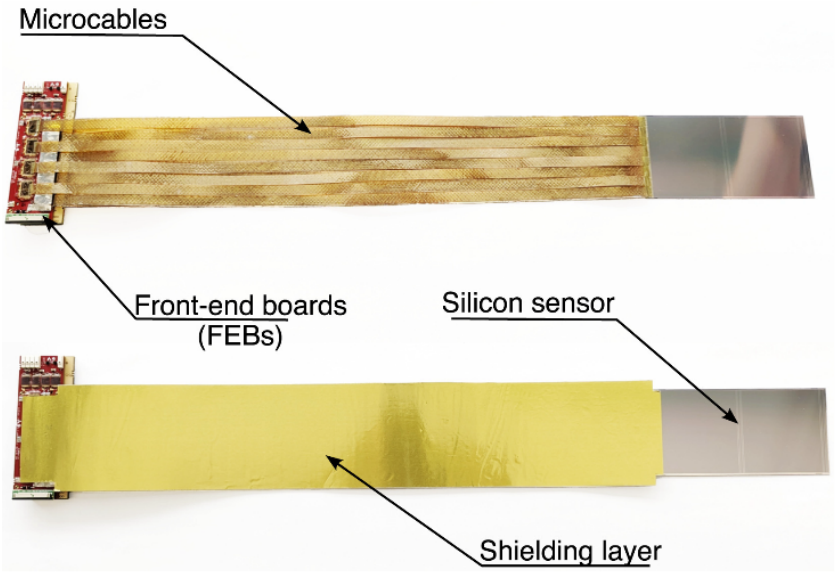

Figure 4.1.1: Module of sts detector[58]

4.1.1 Microstrip Sensors

Silicon is widely used as a detector material because its bandgap of 1.12 eV gives an optimal balance between signal strength and low thermal noise. In comparison, germanium has a smaller bandgap (0.66 eV), which leads to more leakage current and noise, while diamond's much larger bandgap (5.5 eV) takes more energy to create electron–hole pairs, producing weaker signals. In silicon, about 3.6 eV is needed to create a single electron–hole pair.

Silicon detectors are made by doping silicon with p-type and n-type impurities to form p–n junctions, which create an internal electric field. This field separates the electron–hole pairs produced by passing particles, directing electrons to the n-side and holes to the p-side. The p-type region is doped with acceptors like boron, while the n-type region uses donors such as phosphorus or arsenic. When these regions meet, electrons from the n-side diffuse into the p-side and recombine with holes, while holes from the p-side diffuse into the n-side. This creates a depletion region at the junction, almost completely free of mobile charge carriers. Applying a reverse-bias voltage pushes electrons and holes away from this region, widening it and strengthening the internal electric field. This field is essential for quickly collecting the charges generated when a particle passes through the sensor. In the STS, the sensors are made from n-type silicon. n^+ strips are created by doping one side, and p^+ strips are doped on the other side, forming multiple p–n junctions across the sensor. This is the active region, where charged particles passing through generate electron–hole pairs. The doping levels of the p^+ and n^+ regions are carefully optimized to maximize detection efficiency.

When a charged particle passes through a silicon sensor, it loses energy primarily through ionization of silicon atoms, generating electron-hole (e-h) pairs. The sensor's internal electric field drives electrons toward the n-side and holes toward the p-side, as shown in figure 4.1.2, generating a tiny current pulse proportional to the particle's energy loss.

The amount of charge collected in the sensor is directly related to the energy a particle loses while passing through silicon, which can be described using the Bethe-Bloch formula:

$$-\frac{dE}{dx} = K\frac{z^2 Z}{A}\frac{1}{\beta^2}\left[\frac{1}{2}\ln\frac{2m_e c^2\beta^2\gamma^2 T_{\max}}{I^2} - \beta^2 - \frac{\delta}{2}\right]$$

where:

- $K \approx 0.307$ MeV $\cdot$ cm^2/g is a constant,
- z is the charge of the incoming particle,
- Z and A are the atomic number and mass of the medium,
- $\beta = v/c$ is the particle velocity relative to the speed of light,
- $\gamma = 1/\sqrt{1-\beta^2}$ is the Lorentz factor,
- $T_{\max}$ is the maximum kinetic energy transferred to an electron in a single collision,
- I is the mean excitation energy of the medium,
- δ is the density effect correction.

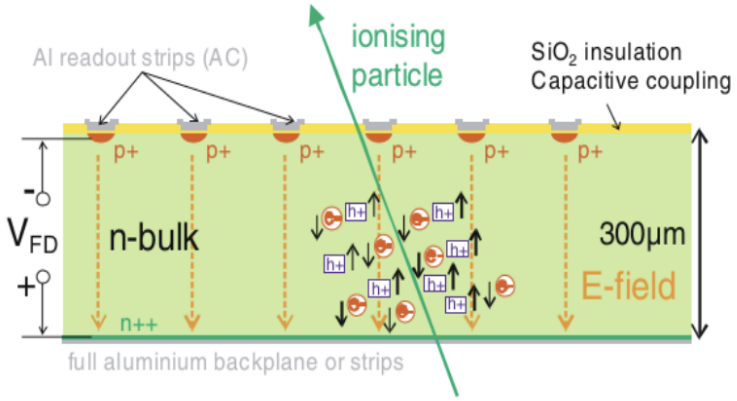

Figure 4.1.2

The pulse passes through preamplifiers, which convert the collected charge into a measurable voltage while preserving timing and pulse shape. The amplified signal is then digitized for particle tracking.

Compared to other silicon detectors, such as pixel sensors, micro-strip sensors provide an excellent balance between high spatial resolution, large sensitive area coverage, and low power consumption. They consist of a thin, high-purity silicon wafer with narrow conductive strips fabricated on both sides [66, 67]. Single-sided strip sensors measure coordinates along one axis, whereas DSMS has n-side strips oriented vertically (along the y-axis), and the p-side strips are at a small stereo angle of 7.5°, as shown in figure 4.1.3a, which is essential for 3D track reconstruction and minimizing ghost hits. This configuration allows 2D hit reconstruction (x, y).

Each side of the sensor contains 1024 strips with a pitch of 58 µm, allowing precise spatial measurements across the sensitive area. The sensors are available in four main sizes, as shown in figure 4.1.3b, with strip lengths of 22 mm, 42 mm, 62 mm, and 124 mm, with a fixed width of 62 mm, produced by Hamamatsu K.K.

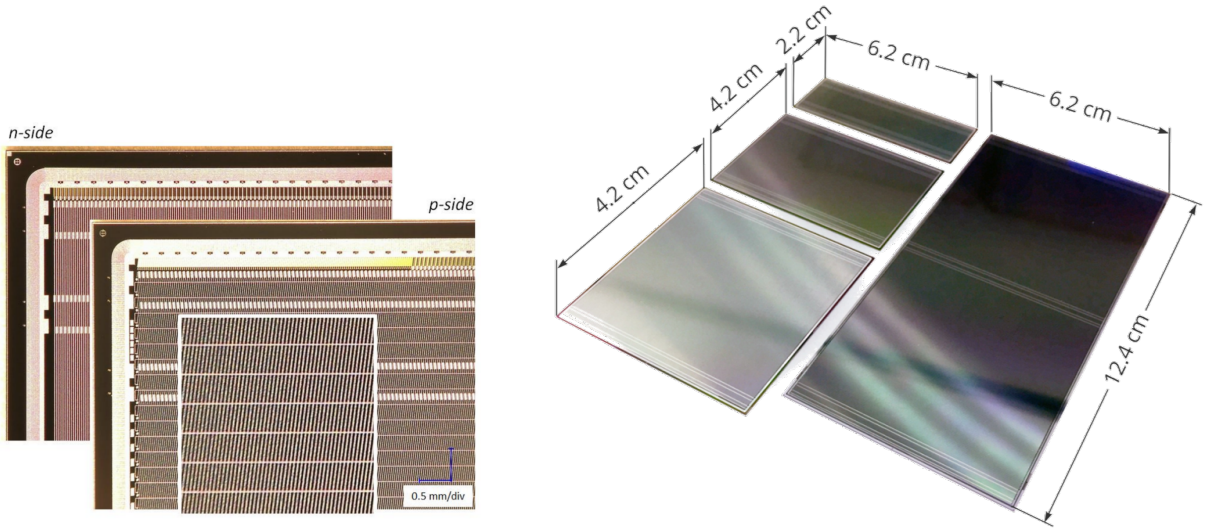

Figure 4.1.3: (a) The n-side and p-side of the silicon wafer [68]; (b) STS silicon micro-strip sensors: same width of 6.2 cm, available in four strip lengths (2.2, 4.2, 6.2, and 12.4 cm) for different module requirements [70].

The strips collect the analog signals generated when charged particles pass through the silicon. These signals are transmitted through low-mass microcables to the front-end electronics (FEEs), where they are amplified and prepared for digitization and further processing [66,67,58]. The sensors are optimized for radiation hardness, ensuring stable operation even under high particle fluxes over long periods [66,67].

4.1.2 Ultra light Aluminium–Polyimide Microcables

The ultra-light aluminium–polyimide microcables act as the connection between the silicon strip sensors and the FEEs [68]. Their job is to carry the signals coming directly from the sensors without adding distortion. They achieve this by combining very thin polyimide insulation with fine aluminium traces. Because the materials are extremely light, the cables add almost nothing to the overall material budget[69].

Aluminium is chosen because it combines low mass with good electrical conductivity and strong resistance to radiation, all of which are essential for the STS environment [68,69]. The architecture of the microcables, consisting of a multilayer stack is seen in figure 4.1.4. This also includes outer shielding layers that provide crucial protection against electromagnetic interference (EMI) and reduce crosstalk, ensuring the integrity of the analog signals transmitted between the sensors and FEEs by minimizing noise pickup in the challenging high-rate radiation environment [72]. Inside the stack, aluminium conductors only a few micrometers thick are deposited directly on the polyimide base. This design maintains a very low capacitive load, typically 0.4–0.6 pF/cm, due to the 2 µm Foamtac II spacer that minimizes the capacitance, which is crucial for reducing electronic noise at the FEE input [58,73].

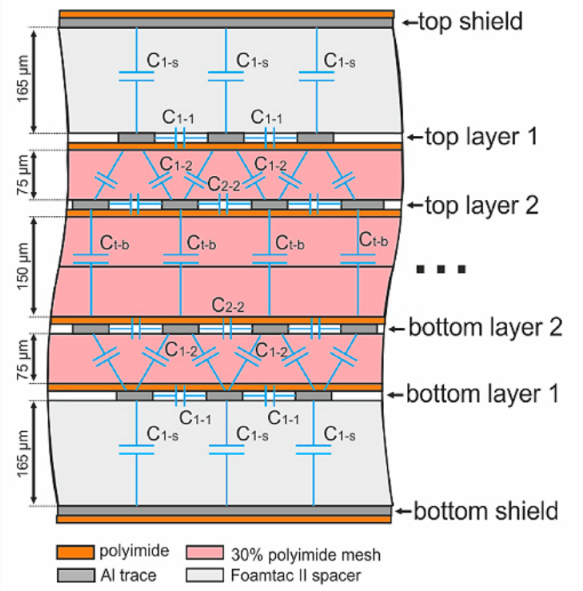

Figure 4.1.4: Ultra thin microcables. (Courtesy of [71])

Altogether, the careful choice of materials, multilayer shielding, and low capacitance make sure that even the tiny signals from the sensors are transmitted reliably, helping the STS maintain its high precision [65].

4.1.3 Front End Boards(FEBs)

The FEBs are a vital part of the STS, acting as the immediate electronic interface between the silicon sensor modules and the downstream DAQ system [54,69]. Each FEB is a highly integrated board hosting readout ASICs (8 per sensor side, each with 128 channels), designed to process all 2048 output channels from a single sensor [68]. Connections to the sensors are made via ultra-thin microcables, ensuring signal integrity [64]. Each FEB receives two voltage levels, 1.8 V and 1.2 V, delivered through four low-noise, low-dropout (LDO) regulators, ensuring clean and stable power for the ASICs and minimizes the noise that could affect the sensitive analog signals [68]. The FEB layout shown in figure 4.1.5 highlights the 16 ASICs mounted on the two boards. The hardware (HW) addresses are numbered on the ASICs. The mapping between ASIC numbers to the respective HW address is summarized in Table 3 allowing clear identification of the readout channels.

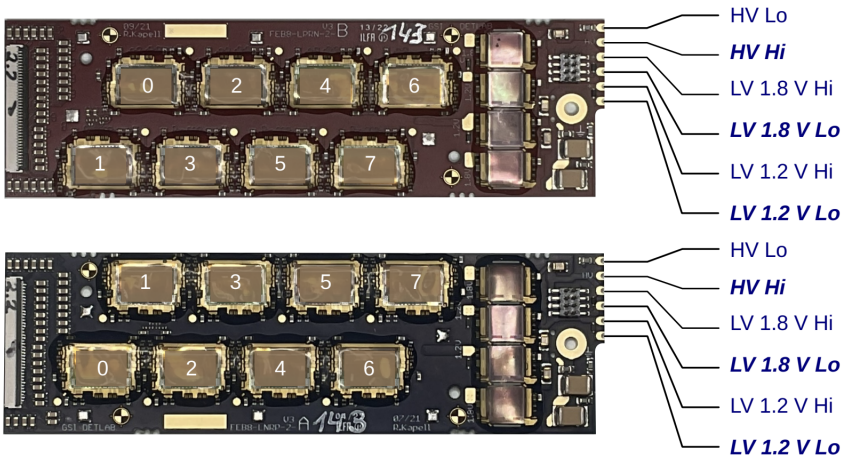

Figure 4.1.5: Front-End Board with SMX ASIC (Courtesy of [68])

ASIC Number	FEB-8A (HW Address)	FEB-8B (HW Address)
0	7	1
1	6	0
2	5	3
3	4	2
4	3	5
5	2	4
6	1	7
7	0	6

Table 3: Mapping of ASIC numbers (0–7) to their corresponding HW addresses for the two FEB types, FEB-8A and FEB-8B.

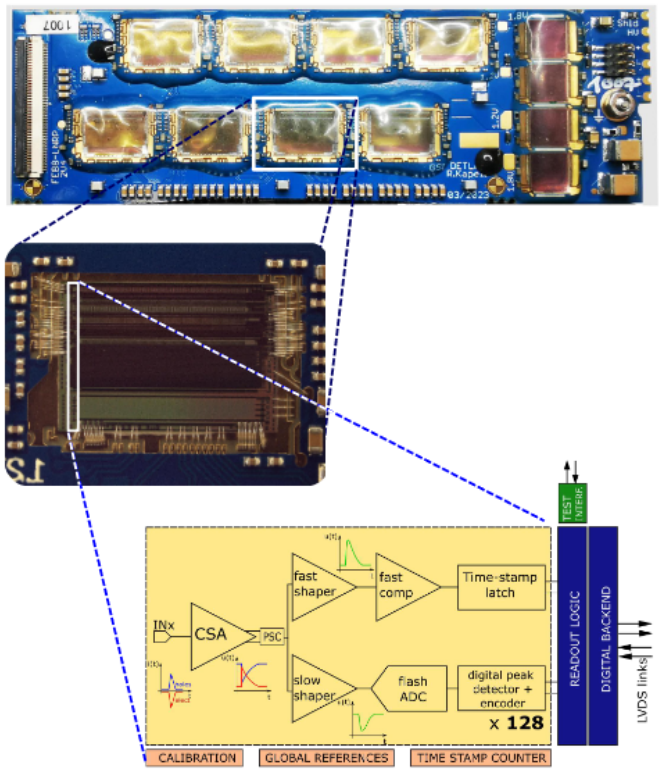

Figure 4.1.6: Front-End Board and Block diagram of the SMX ASIC (Courtesy of [68])

The STS-XYTER ASIC, as shown in figure 4.1.6, was developed at GSI. These ASICs integrate several critical functionalities [58,71] such as

- **Charge Sensitive Amplifier (CSA):** Converts the small charge from the silicon sensor into a measurable voltage signal. It is optimized for low noise and fast response, ensuring the integrity of the signal is preserved for further processing [71].
- **Fast and Slow Shaping Amplifiers:** The two shaping amplifiers work in parallel to optimize both timing and amplitude measurements [71].
  - **Fast Shaper:** Produces a narrow, fast pulse to provide precise timing information. This allows the system to accurately time-stamp events, which is crucial in high rate environments with closely spaced hits.
  - **Slow Shaper:** Produces a broader pulse that takes longer to reach its maximum (longer peaking time), improving the signal-to-noise ratio and allowing more accurate measurement of the particle's deposited charge.

- **Fast Comparator:** Monitors the fast-shaped signal and triggers when it exceeds a set threshold. This initiates timing and data processing, ensuring relevant events are correctly captured [71].
- **Flash Analog-to-Digital Converter (Flash ADC):** Digitizes the shaped analog signals directly on the ASIC. This supports high speed readout while minimizing signal distortion, enabling reliable data acquisition [71].
- **Time Stamp Latch:** Records the precise time when a signal crosses the threshold. This associates the timing information with the amplitude for each hit, which is essential for accurate event reconstruction [71].
- **Digital Peak Detector and Encoder:** Captures the peak amplitude of the slow-shaped pulse and encodes it for downstream transmission. This ensures that amplitude information is accurately formatted for further analysis [71].

A distinctive feature of the FEBs is their support for a triggerless, free-streaming readout mode, enabling continuous data acquisition without hardware triggers crucial for capturing rare or closely spaced events without loss [58,69]. The ASICs on the FEBs monitor functions including temperature, voltage, and current, to ensure stable operation and early detection of potential issues [58,69]. Thermal management is provided by mounting the FEBs on a cooling block, ensuring reliable performance during sustained operation [63].

4.1.4 Module Testing

To ensure that each STS module functions accurately and meets quality standards, a comprehensive testing procedure is carried out. This process helps identify early potential issues and determine appropriate solutions, ensuring that only fully functional modules proceed to the next stage of testing. Module testing is performed in three successive stages [58,73]:

1. Electrical characterization of the silicon sensor via current-voltage.
2. Functional verification and calibration, including noise evaluation.
3. Assessment of thermal stress performance through repeated thermal cycling.

Current-Voltage (IV) Measurements: IV testing is a fundamental step in characterizing a silicon sensor, helping detect defects before modules are integrated into larger assemblies such as ladders or half-units. This test enables the identification of potential defects at an early stage [73]. Sensors are biased according to their assigned grade - Type A up to 500 V, Type B up to 350 V, Type C up to 250 V, and Type D up to 200 V. During an IV scan, a high voltage is gradually applied across the sensor, as seen in figure 4.1.7, and the resulting leakage current is measured. At a certain voltage, known as the breakdown voltage, the current rises sharply, marking the maximum safe operating voltage.

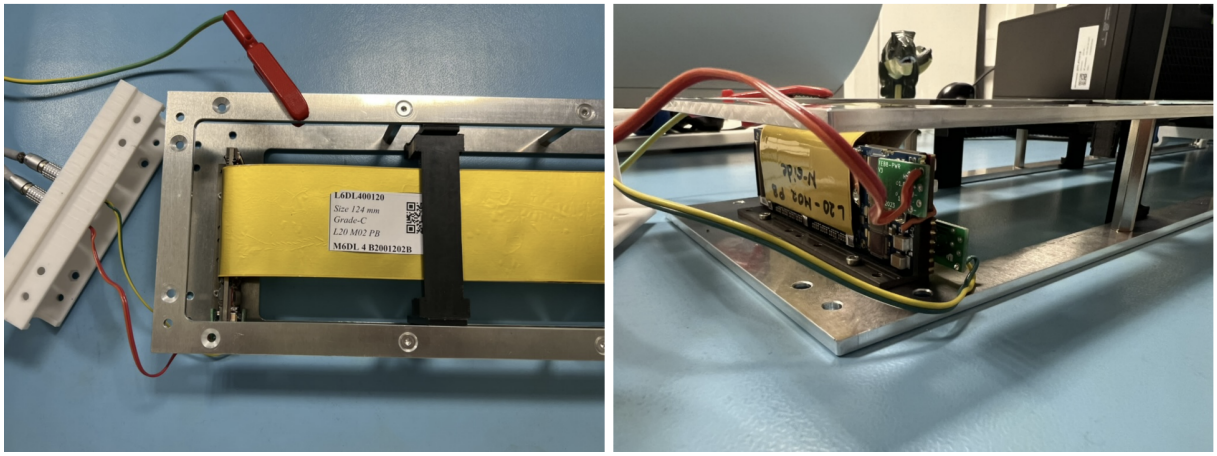

Figure 4.1.7: Ground connection clipped to the carrier, and High voltage is supplied through the FEBs: n-side(left FEB) and p-side(right FEB) connected to the sensors via microcables.

The shape of the IV curves provides a good indication of sensor quality. Only modules with stable electrical behavior and low leakage currents proceed to further functional testing. As shown in plot 4.1.8, the IV curve of module M3DL1T0001120A2 shows stable behavior and continues on to the next stage of testing. Modules exhibiting unusual current

increases or early/slow breakdowns undergo additional treatments, such as cleaning the sensor edges and storing the modules in a controlled humidity environment, to restore functionality [73].

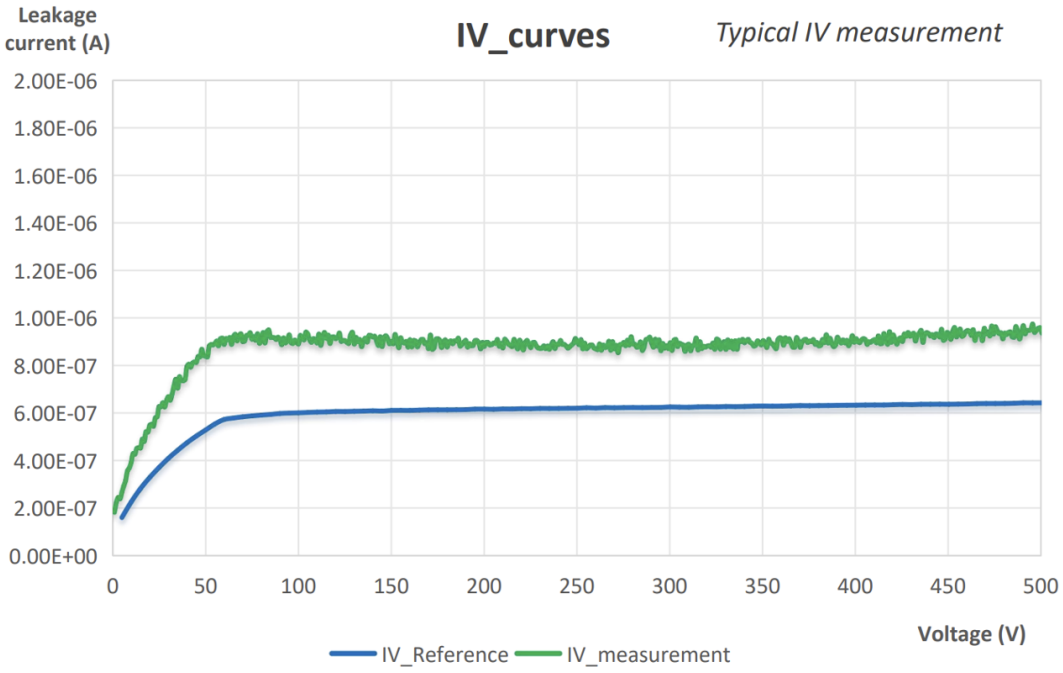

Figure 4.1.8: Current–Voltage (IV) curve of module M3DL1T0001120A2 (Grade A), showing stable behavior.

Functional characterization of the module: After electrical verification, the modules undergo functional testing. For this purpose, each module is connected to a GBTx-Emulator (EMU) board, which acts as the interface between the readout electronics (FEBs) and the DAQ system. The EMU handles configuration, communication, and data collection from all ASICs [58,73]. The connection is made via readout cables connecting the FEBs to the EMU. The setup also includes a cooling block with circulating water to stabilize module temperature, and a panel providing low-voltage (LV) and high-voltage (HV) supplies as seen in figure 4.1.9. Once powered on, the LV supply is switched on to monitor FEB power consumption, typically ranging from 1.1 to 3.0 A. The HV is then gradually applied symmetrically to both sides of the FEB up to 75 V, corresponding to an operational voltage of 150 V across the module [58].

Figure 4.1.9: Three setups for module functional tests

The module is then run through calibration steps, beginning with data link initialization and synchronization to establish reliable uplink and downlink communication with each ASIC. Once communication is verified, register configuration parameters are set, and multiple write/readback actions are performed. Following the configuration, key parameters such as power consumption, temperature, and VDDM (a potential used to evaluate the analog response) are recorded and verified [58].

Next, channel-to-channel threshold corrections are determined by injecting fixed charge pulses using the ASIC's internal pulse generator. The resulting discriminator responses are analyzed to extract ADC thresholds and gain, which characterize the linearity and uniformity of the ADC response [58].

Trim DAC (Digital-to-Analog Converter) parameters are stored in calibration files for each ASIC. Fixed charge pulses are sent again to each channel, while recording the response of all discriminators through S-curve scans to confirm uniform response across channels [73]. Another critical part of module testing is the noise performance study, which estimates the module's noise and compares it with analytical expectations. This step allows identification of noisy or non-functional channels, ensuring that only properly functioning modules proceed further [58,73].

Noise performance of the modules

After calibration, the module's noise performance is evaluated. Noise is quantified using the Equivalent Noise Charge (ENC), derived from S-curve scans of each channel. In these scans, the discriminator response is recorded as a function of injected charge; the slope of the S-curve provides the noise level, while the mean corresponds to the channel threshold [73]. The total noise includes contributions from the ASIC's intrinsic noise, the sensor capacitance, and the microcable capacitance.

As seen in the plot 4.1.10, the green dashed line represents the noise contribution from the sensor and microcables, while the intrinsic ASICs noise is approximately 350e ENC, is indicated by the yellow dashed line [58,68,73]. The total ENC can be broken down according to its sources: L_{sensor} and L_{cable} denote the lengths of the sensor and microcable, respectively, and the factor 25 e/pF characterizes the dependence of ASIC noise on input capacitance.

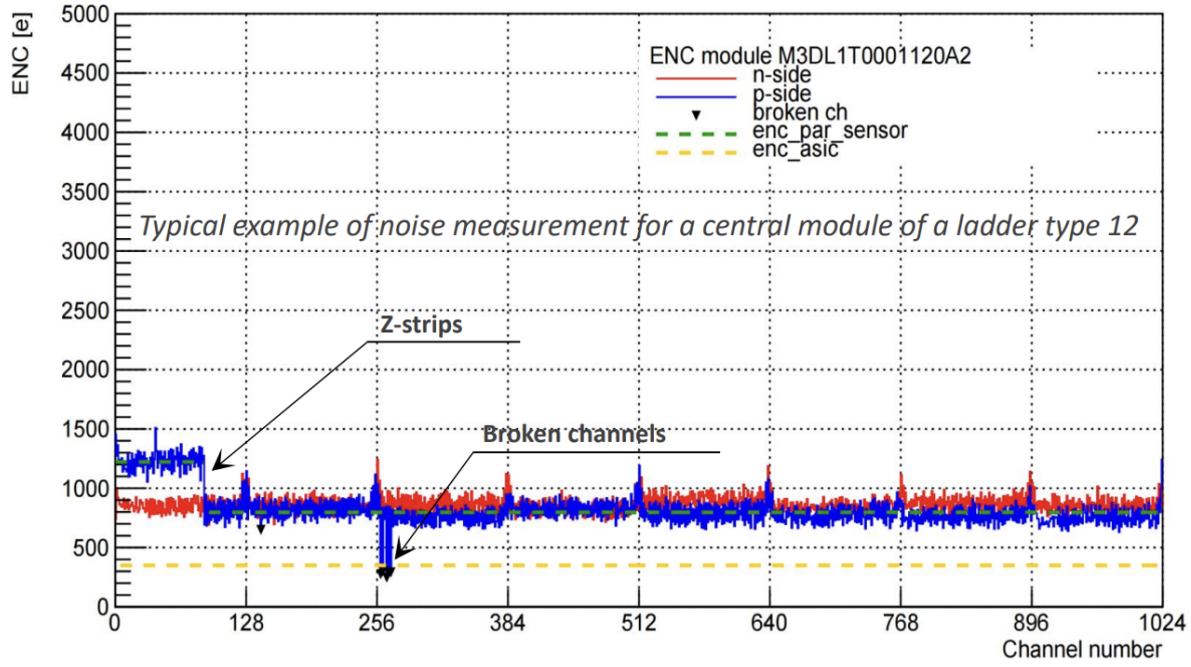

Figure 4.1.10: Noise performance (ENC) analysis across all channels of module M3DL1T0001120A2

Each sensor strip has a capacitance of 1.02 pF/cm, and the effective capacitance per unit length of the microcable, including contributions from neighboring traces and coupling to the shielding layer, is 0.38 pF/cm [73]. The resulting ENC can be expressed as [81]:

$$\text{ENC [e]} = \Big[\underbrace{L_{\text{sensor}} \cdot 1.02 \text{ pF/cm}}_{\text{Sensor}} + \underbrace{L_{\text{cable}} \cdot 0.38 \text{ pF/cm}}_{\text{Microcable}} \Big] \cdot 25 \text{ e/pF} + \underbrace{350 \text{ e}}_{\text{ASIC}} \tag{3}$$

By comparing the measured noise with analytical expectations, noisy modules and non-functional channels can be identified. This process ensures that only modules exhibiting stable, low-noise behavior advance to the next stage of testing. For each module, a detailed report is generated, summarizing noise patterns, signal response, threshold uniformity, which is critical for reliable performance in the final detector assembly [58,68].

Thermal stress test

After functional verification, modules undergo a thermal burn-in test to ensure long-term stability and to identify early failures. The modules are exposed to repeated thermal cycles, typically down to -20 °C [68,73]. This not only simulates the expected operating conditions of the STS experiment but also introduces a safety margin beyond the nominal temperature, allowing potential weaknesses such as increased leakage currents, mechanical stress, or degraded performance under temperature variations to be revealed.

The burn-in test leverages the principle that thermal cycling accelerates stress mechanisms in semiconductor devices. Temperature changes affect leakage currents, charge carrier mobility, and bias stability in both sensors and ASICs. Sub-zero cooling also challenges mechanical interfaces and bonding connections due to differential thermal expansion between materials. Modules are placed in a dedicated test chamber as seen in figure 4.1.11, equipped with copper cooling plates connected to a chiller for precise temperature control. Continuous nitrogen gas flow maintains low humidity, preventing condensation on sensitive electronics [73]. During each cycle, the module's sensors are biased at operational voltage while the readout and FEBs remain connected to monitor stability under thermal stress [68].

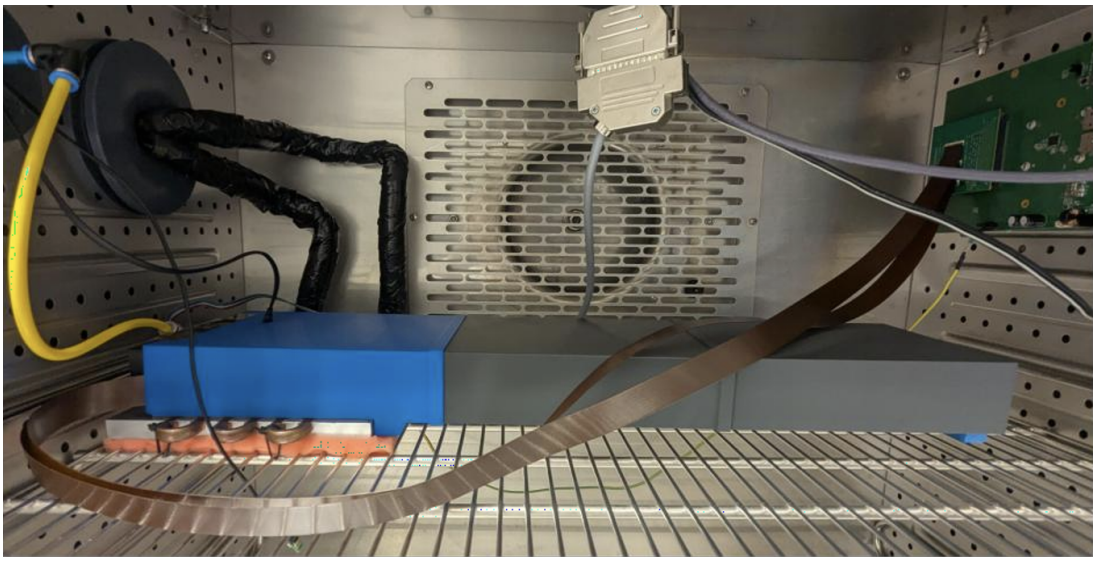

Figure 4.1.11: Thermal test setup for modules with integrated cooling plate and readout connections

Temperature ramps are controlled with stabilization periods at each level to ensure equilibrium. Key parameters, including ASIC communication, sensor leakage current, and ENC, are observed throughout the cycles to detect any degradation. A burn-in run is considered successful if communication with all ASICs remains stable, no systematic degradation is observed, and all planned thermal cycles are completed. Passing this test confirms that the modules are thermally robust and ready for integration into the STS ladders, representing the final step before full ladder assembly [73].

4.2 STS Ladder Integration

The STS ladders form the primary mechanical support structure for the detector modules. Figure 4.2.1 shows a general view of a detector ladder. The concept of using CF structures was initially developed for the barrel geometry of the Inner Tracking System (ITS) in the ALICE experiment. For STS, this design was largely retained, with minor modifications to suit the experimental geometry and operational requirements [74]. CF provides an excellent balance between mechanical strength, rigidity, and low material contribution, which is critical for high-precision tracking while reducing multiple scattering effects [76].

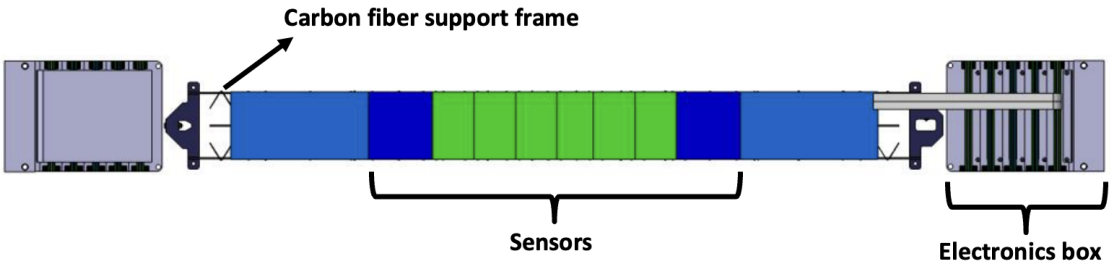

Figure 4.2.1: Computer-Aided Design (CAD) representation of a standard detector ladder with sensors and electronics box mounted at each end (Courtesy of [75]).

Each ladder supports multiple detector modules, that consists of silicon sensors, micro-cables, and shielding layers. The modules must be precisely aligned along the ladder to maintain the spatial resolution necessary for accurate reconstruction of charged particle trajectories [76]. A typical ladder can accommodate 2–10 modules; the weight and mechanical stresses require careful design to prevent bending [76,77]. Excessive deformation could introduce mis-alignments that compromise tracking accuracy and introduce systematic errors. To eliminate this issue, ladders are fabricated with carefully controlled stiffness and mechanical tolerances, ensuring they maintain their shape under load and throughout the experiment's lifetime [77]. Special attention is given to central ladders positioned close to the beamline, as seen in figure 4.2.2. These ladders include cutouts and semi-rings that are stiff, allowing the beam to pass through without compromising rigidity. Structural integrity and stiffness of both standard and central ladders were validated through a series of prototype tests, which confirmed that the selected materials and design are adequate for stable operation under experimental conditions [74,77]. A visual overview of the different ladder types and arrangements is shown in figure 4.2.3. This CAD representation highlights the variety of ladder configurations used within the STS, illustrating how modules are positioned along the frames while maintaining precise alignment, mechanical stability, and minimal material contribution [77].

Overall, STS ladders provide a lightweight, rigid, and precisely aligned backbone that integrates multiple detector modules while ensuring stable performance and minimal contribution to the overall material budget [74,76].

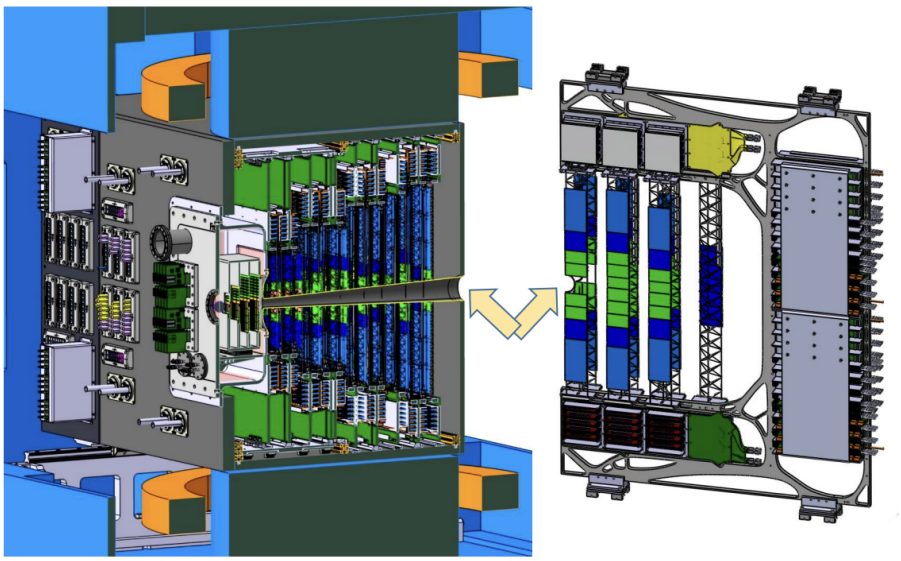

Figure 4.2.2: CAD representation of a central ladder frame.((Courtesy of O. Vasylyev (GSI, Darmstadt))

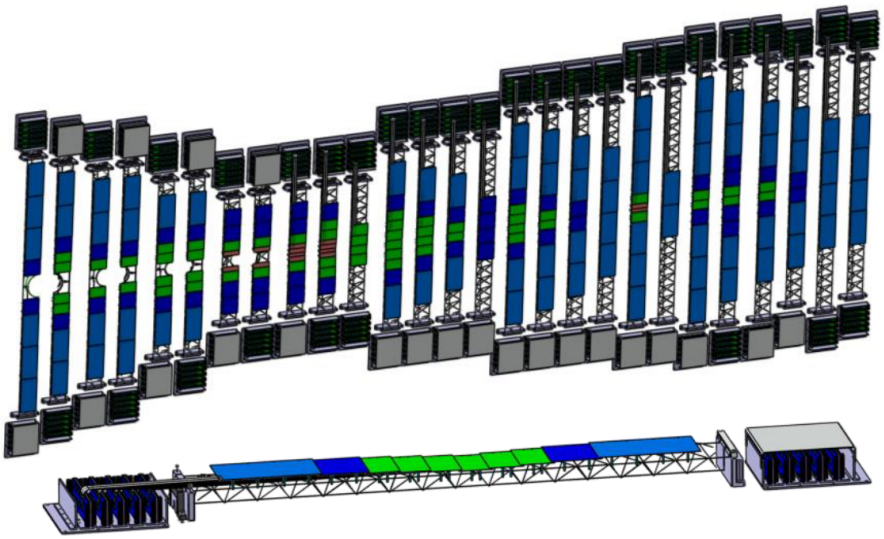

Figure 4.2.3: CAD representation of multiple ladder configurations. (Courtesy of O. Vasylyev (GSI, Darmstadt))

Electronics box (FEB Integration) The readout electronics of each module in the ladder are housed in dedicated electronics boxes (hereafter referred to as FEB box) located at the ends of the ladder [54]. These assemblies consist of FEBs associated with each module. A single half-ladder typically requires ten FEBs to ensure complete readout of all modules, as seen in figure 4.2.4. The FEBs are arranged to minimize electrical interference and enable efficient cooling, while the readout channels maintain stable operation and remain accessible for testing and maintenance [79,80].

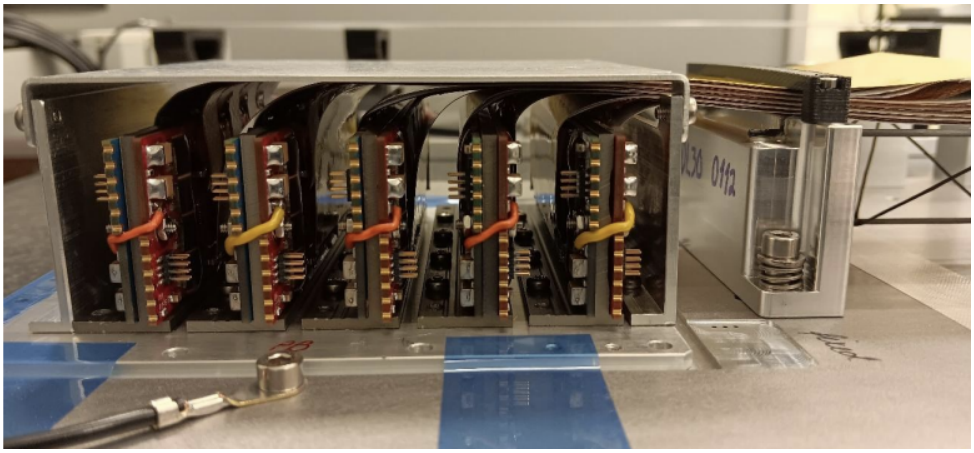

Figure 4.2.4: Arrangement of FEBs arranged together forming a complete FEB box for a half-ladder readout.

A CAD image of a fully assembled ladder, with FEB boxes positioned on both ends, forms a complete mechanical and electronic unit ready for integration into the STS (See figure 4.2.1). The design of the FEB box also accounts for thermal management [54]. FEBs generate heat during operation, and proper spacing, thermal conduction paths, and potential integration of cooling interfaces ensure that operating temperatures remain within safe limits [63]. This prevents performance degradation, maintains low-noise operation, and ensures long-term stability. By combining the mechanical ladder structure with the integrated FEB box, each ladder becomes a self-contained, stable subsystem. This integration guarantees precise alignment, stable readout, and efficient thermal management, forming the backbone of the STS and enabling reliable high-resolution particle tracking in the CBM experiment [76,80].

4.2.1 Ladder testing

After individual modules have been verified, the next step is ladder testing. A ladder is a structure that holds multiple modules together, typically up to ten, and serves as a higher-level assembly in the STS detector [81,82]. While module testing focuses on the performance of a single module, ladder testing as seen in figure 4.2.5 evaluates the modules collectively to ensure that they not only function individually but also work reliably as a coherent unit [81,83]. Ladder testing is essential because interactions between modules such as shared readout electronics, and signal cross-talk can introduce issues that are not visible in single module tests. It verifies system level integration, confirming that multiple modules operate together as intended. In addition, ladder testing provides a more realistic assessment of the thermal and electrical behavior under conditions closer to actual detector operation [81]. By identifying potential issues early at the ladder level, the overall reliability and performance of the STS detector can be maintained [82].

The procedure at the ladder level follows the same principles as module testing, including electrical characterization (IV measurements), functional verification, calibration, and noise evaluation [83]. However, the scale and complexity of testing increase because multiple modules are monitored simultaneously, making cable management, readout, and power distribution more critical.

Electrical Characterization (IV Measurements): As with module testing, the first step in ladder testing is electrical characterization using IV measurements. However, at the ladder level, this is performed simultaneously for all modules. Each sensor is biased according to its assigned grade, and the resulting IV curves are analyzed for abnormal behavior such as early breakdown or unusually high leakage currents. Modules showing issues can be temporarily disconnected, treated individually, and then reintegrated. This ensures that the fully assembled ladder exhibits stable electrical behavior and low leakage currents, extending the verification from single-module performance to multi-module operation [81,83].

Functional Verification and Calibration: Ladder functional testing builds on the procedures established during module testing, but evaluates multiple modules at once. The ladder is connected to the GBTx-EMU board via readout cables, and a cooling system maintains uniform temperatures across all modules. Low-voltage currents are monitored for each FEB, and high voltage is gradually applied to fully deplete all sensors. Calibration steps data link initialization, ASIC synchronization, register configuration, and monitoring of key parameters such as power, temperature, and VDDM are performed for every module. Calibration pulses are sent to all channels of each ASIC to determine threshold corrections, ADC gains, and uniformity across the ladder. S-curve scans and equivalent noise charge (ENC) measurements are used to identify noisy or faulty channels [58]. Faulty modules may be treated individually and reintegrated, maintaining the overall integrity of the ladder [81].

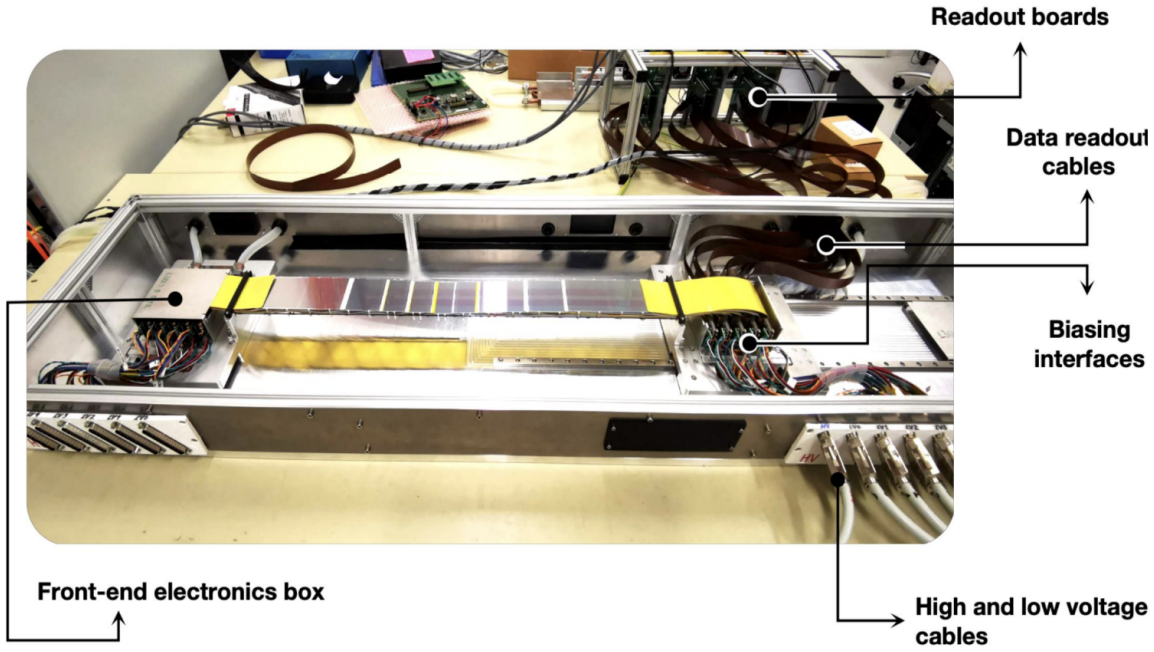

Figure 4.2.5: Ladder functional test setup showing connections for cooling and readout. (Courtesy of [83])

Finally, results from all modules are compiled into a comprehensive report summarizing noise performance, signal response, threshold uniformity, and other critical parameters [81]. While module testing ensures the functionality of individual modules, ladder testing confirms that multiple modules operate coherently as a single unit a key requirement for reliable performance in higher level detector assemblies [82].

5 Half-Unit(HU) Assembly and Integration

5.1 Structural Overview of the Half-Unit

In the STS, each unit provides the mechanical framework for arranging sensors on ladders together with readout electronics. A unit consists of two half-units, positioned symmetrically on the left and a right of the vertical axis enclosing the beam pipe at the center. Each half-unit is equipped with dedicated low-voltage, sensor bias voltage (high voltage), optical fibers, and cooling, enabling independent installation and operation [54].

The HU is the primary structural unit of the STS, serving as both the mechanical backbone and the functional core where ladders and readout electronics are integrated. Structurally, it is an aluminum C-frame, designed to support multiple ladders and accommodate peripheral components such as Readout Boards (ROBs), Power Boards (POBs), and cooling blocks [85]. These components are positioned outside the detector acceptance to reduce the material budget while still ensuring efficient readout and thermal management. The C-frame itself is mechanically symmetrical [84].

Altogether, the STS comprises 20 half-units distributed across 8 tracking stations. The outermost upstream and downstream stations are covered by a single half-unit, while the remaining stations each consist of paired upstream (STSu) and downstream (STSd) half-units, forming continuous sensor surfaces without gaps [86]. The stations are generally spaced 105 mm apart, except between stations 3 and 4, where there is an extra 5 mm gap because station 3 is split into STSu and STSd [86]. Each half-unit is labeled according to its position as UL (Upper Left), UR (Upper Right), DL (Down Left), or DR (Down Right), which helps identify its location within a unit and along the beamline for assembly and cabling purposes. At the upstream end, an additional single half-unit completes the coverage. This configuration, with 8 half-units upstream and 12 downstream, ensures full tracking coverage while accounting for the bending of particle trajectories in the dipole

magnet as seen in figure 5.1.1a. Collectively, these 20 half-units constitute the eight stations forming continuous tracking surfaces [85,86]. Figure 5.1.1b depicts the arrangement of Unit 3, Downleft (DL) half-unit.

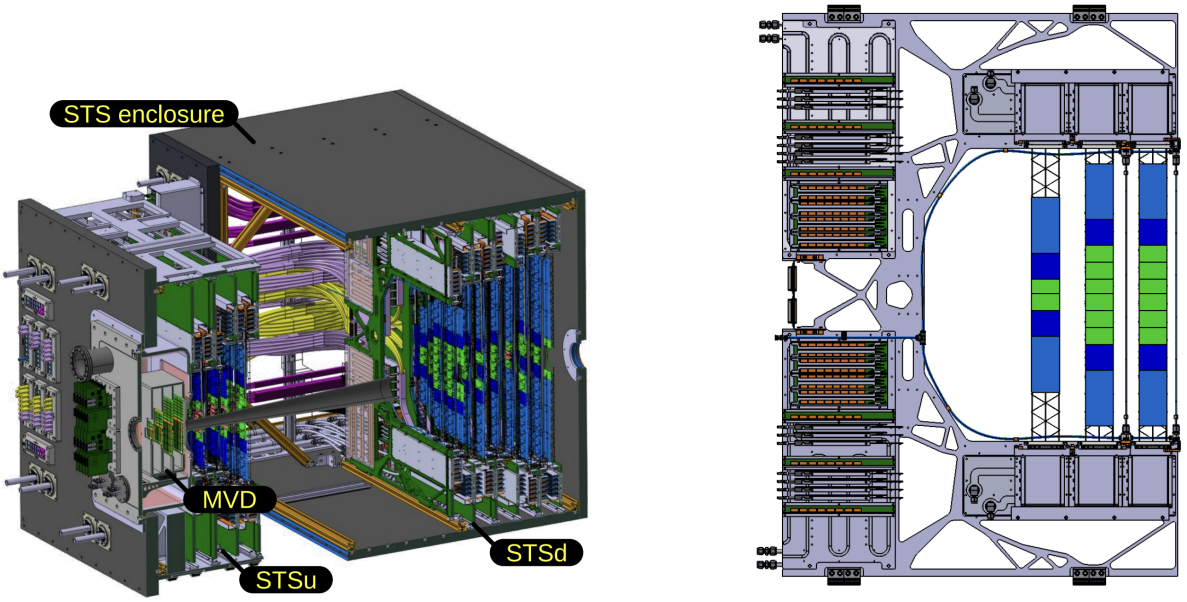

Figure 5.1.1: (a) CAD illustration of the STS enclosure, showing the relative positions of the MVD, STSu, and STSd subdetectors. (Courtesy of [68,75]) (b) Structural view of CBM STS Half-Unit 3 DL, displaying the ladders, FEB boxes, and peripheral components.(Courtesy of O. Vasylyev (GSI, Darmstadt))

To verify the design, integration, and assembly procedures, mockup studies were carried out. Non-functional ladders and full-scale prototype models of the POBs, ROBs, and FEB boxes were produced for this purpose. These mockups allowed verification of the mechanical fit, alignment, component accessibility, and the overall assembly workflow prior to building the final detector stations. The tests were carried out on the Unit 3 DL half-unit C-frame. The following sections describe in detail the integration methods, cabling sequence, and assembly procedures for the HU.

5.2 Building Blocks of HU

The Half-Unit (HU) integrates multiple mechanical, electronic, and thermal components to form a complete functional unit. The following subsections provide an overview of these building blocks and their respective roles within the HU.

5.2.1 C-Frame: Integration and Alignment Framework

The C-frame is a key structural component, providing a strong foundation for integrating ladders and associated electronics [85]. Its design emphasizes mechanical stability, precise alignment, and minimal material use to ensure optimal detector performance.

Made from a high-strength aluminum alloy, the C-frame strikes an ideal balance between rigidity and low mass, ensuring that ladders are installed sequentially and supporting peripheral components, such as readout and power boards, which are positioned outside the detector acceptance to minimize material in the particle path [85,87]. Its C-shaped cross-section, as seen in figure 5.2.1, provides easy accessibility and minimal interference during assembly. In addition, the C-frame provides space for cable routing and cooling systems without interfering with the ladders. Its hardness ensures that mechanical vibrations or small temperature changes do not affect alignment, which is essential for accurate measurements and reliable detector performance over time [87,88].

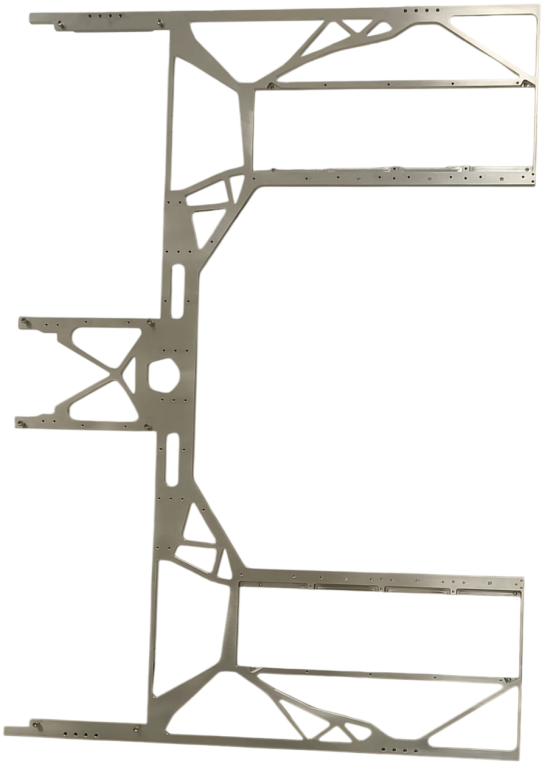

Figure 5.2.1: Photograph of the C-frame of Unit-03DL

Cooling Blocks for FEB Boxes and Peripheral Components

The cooling blocks are essential for thermal management, dissipating the significant heat generated by the readout and powering electronics. These are mounted on the C-frame and are cooled via a liquid cooling system using water glycol as the coolant [80,89,90].

The FEB cooling blocks: consist of a finned aluminum cooling plate as seen in figure 5.2.2. The plate is designed to maximize the surface area for heat exchange, ensuring efficient thermal dissipation [89,80]. The coolant circulates through the cooling plate, absorbing heat from the FEBs. The coolant's low viscosity and high thermal stability at low temperatures make it ideal for this application [89,90].

Thermal Interface Materials (TIMs) are employed between the FEBs and the cooling plate to enhance thermal conductivity and ensure effective heat transfer and are compatible with the operating environment [90,91]. The system is designed to maintain the FEBs at a stable operating temperature, preventing thermal runaway and ensuring consistent performance of the electronics [89,80].

Figure 5.2.2: Photograph of the FEB cooling plate of the C-frame of Unit-03DL

Peripheral Cooling Blocks: Manages the thermal load of other components, such as those responsible for power distribution and data transfer. The peripheral cooling blocks, as seen in figure 5.2.3, feature internal cooling channels through which the coolant flows, absorbing heat from the components they are designed to cool [80,92].

Figure 5.2.3: Photograph of the peripheral cooling plate of the C-frame of Unit-03DL

Similar to the FEB cooling blocks, these peripheral cooling blocks are constructed from aluminum alloys, chosen for their thermal conductivity and lightweight properties. The cooling blocks are mounted outside the detector's acceptance region [80].

The combined cooling solutions for the FEBs and peripheral components are integrated into a comprehensive thermal management system that ensures the CBM STS operates within its thermal specifications [80].

Peripheral Components

Peripheral components are essential for signal readout and power management. These include ROBs, RPOBs, and FPOBs, which are positioned outside the detector acceptance. These components are mechanically supported by the C-frame and integrated with dedicated cooling blocks to ensure stable and reliable operation. Each peripheral component is described in detail in the following sections, including its function:

- **The STS-ROB (Silicon Tracking System Read-Out Board):** as seen in figure 5.2.4, serves as the central communication hub between the FEE modules and the FPGA(Field programmable gate array)-based backend. Its primary functions include sending control commands via the downlink path to the front-end modules and distributing clock signals both to these modules and to the slave GBTx (Giga-Bit transceiver) chips on the board. Detector data flows in the opposite direction through the uplinks, where it is forwarded to the backend for further processing. The core of the STS-ROB is a GBTx chip operating in master configuration, supported by additional GBTx devices acting as slaves, as well as a GBT-SCA (Slow Control Adapter) chip that provides control and monitoring capabilities [92]. An essential component of the board is its optical modules: VTRx(Versatile Transceiver) and VTTx (Versatile Twin Transmitter). The VTRx functions as a bidirectional transceiver, allowing the reception of commands and transmission of status data.

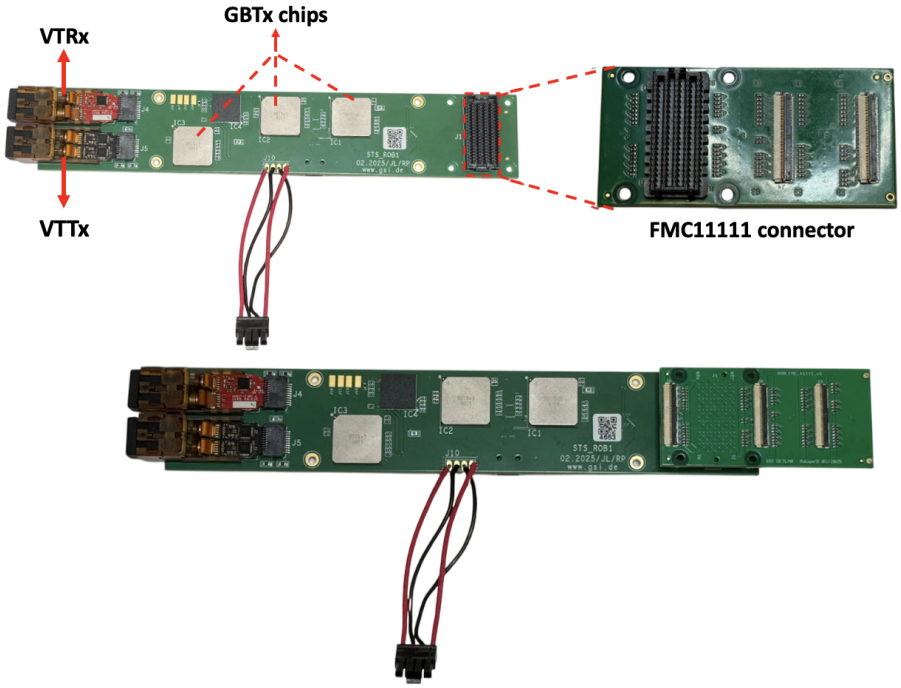

Figure 5.2.4: FEASTSSS.

The VTTx modules are unidirectional transmitters that send data received from the slave GBTx devices via the uplink [93,94]. These modules convert electrical signals into optical ones, enabling fast and reliable data transfer to the backend. This allows the STS-ROB to maintain long distance communication with high signal integrity [93]. The ROB interfaces with the FEEs through an FMC connector, which serves as the interface between the FEEs and the STS readout system. Signals from the FEEs are routed via data cables to the FMC, following a defined mapping [93]. The FMC connector is plugged into the STS-ROB, as shown in figure 5.2.4, where the signals pass through three GBTx ASICs before reaching the optical modules. These modules convert the electrical signals into optical signals, which are transmitted via optical fibers to the backend electronics and finally processed by the FPGA. This ensures high-speed, reliable data transfer from the front-end modules to the backend system [93].

- **The RPoB (Readout-Powering Board):** is a specialized, radiation tolerant power supply module designed to provide the required operating voltages for the STS ROBs. Its primary function is to ensure stable and efficient power distribution in a high radiation environment. The RPoB is based on FEAST DC-DC converters, developed at CERN [94]. These converters have an input voltage in the range of 6 V to 12 V and generate two stable low voltage outputs: 1.5 V and 2.5 V as seen in the figure 5.2.5 [95]. The converters are designed for high efficiency, low noise, and radiation tolerance, which are essential for maintaining reliable operation. The 1.5 V output powers the GBTx ASICs, which are critical components of the high speed data read-out chain.

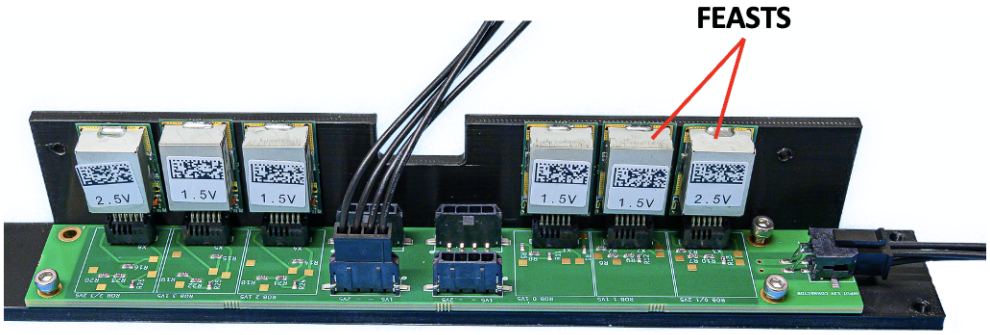

Figure 5.2.5: RPoB PCB with FEAST DC–DC converters

The 2.5 V output powers the optical transceiver modules, ensuring stable optical data transfer between the STS and the DAQ system. A single RPoB can supply power to up to four STS-ROBs, making it a efficient solution. Within the C-frame, it functions as a radiation tolerant power interface, ensuring reliable and stable operating conditions for the readout system [95].

- **The FPoB (Front-end Powering Board):** The powering of the STS FEE relies on the FPoB, which is designed to provide regulated voltages to the FEBs. Each FPoB is capable of supplying four modules simultaneously. The FPoB is built on a 6 layer PCB with 210 , μm copper thickness [96].

Thick copper layers were chosen to minimize voltage drops, and the stack up is optimized for electromagnetic compatibility (EMC) [96]. The board layout, shown in figure 5.2.6, features the 8 input voltage channels of the PoB and is split between the FEASTMP DC–DC converters, arranged in two rows of eight, producing voltages of 2.4 V and 3.0 V [95]. These outputs are further stabilized by low-dropout regulators (LDOs) on the FEBs, producing the final ASIC operating voltages of 1.2 V and 1.8 V. Four output connectors on the right-hand side connect one detector module each (4 modules × 2 FEBs × 2 FEAST converters per FEB, totaling 16 FEAST outputs) [95]. This provides stable power delivery over long cables and minimizes voltage drops.

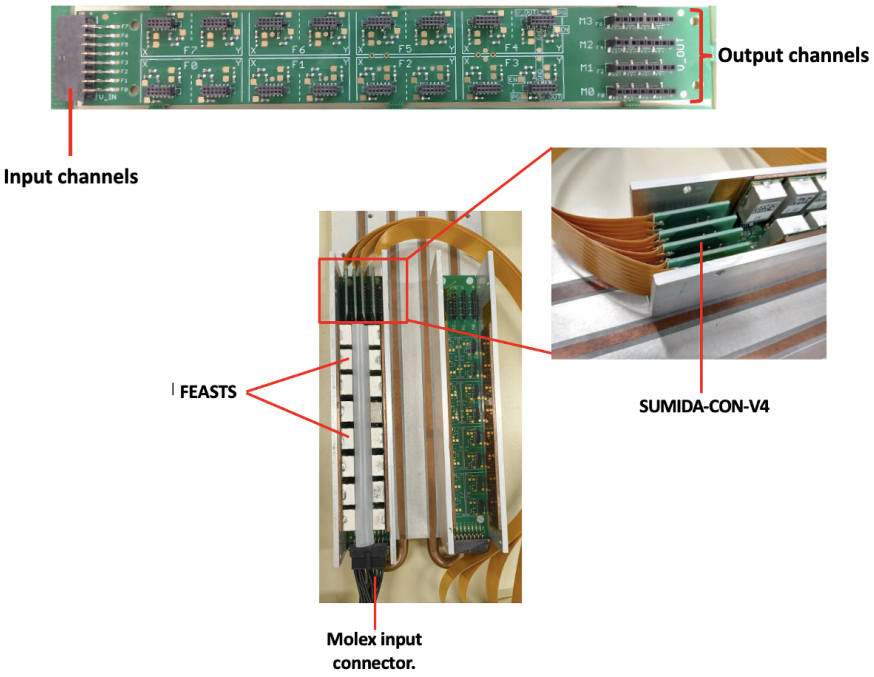

Figure 5.2.6: FPoB PCB with input/output connectors and FEAST DC–DC converters.

The typical current per input channel is approximately 1.5 A. The FEAST outputs are interfaced through SMD Samtec sockets, while the Sumida PANTA FIX power cables [97] from the modules are soldered at one end to the FEBs and the other end to the SUMIDA-CON-V4 connector, which are plugged into the sockets on the board.

This arrangement ensures a secure, low-resistance connection for reliable current delivery. A low voltage, slightly below 12 V, is supplied to the FPoB via a Molex MicroFit input connector.

This combination of FEAST converters, LDOs, cabling, and carefully designed PCB layers provides stable, low-noise, and radiation-tolerant power to the FEBs, ensuring reliable operation of the STS FEE.

- **Ladders:** The design and characteristics of the ladders have already been explained in detail in Section 4.2. Here, the ladders are mounted on the half-unit, and the power and data cables are connected, as described in the following section.

6 HU Integration and Assembly protocol

The integration of the HU is a key stage in the construction of the detector, as it directly influences both the mechanical stability and the long-term performance of the system. The HU acts as the basic structural unit that holds ladders, power distribution boards, readout electronics, and the cooling plates. Each of these components has specific requirements for alignment, tolerances, and electrical connections. Failure to meet these conditions during assembly can lead to misalignment or excess mechanical stress, which may compromise the efficiency and reliability of the detector. To address these risks, a standardized and clearly defined assembly protocol was developed within the scope of this work. This reduces the likelihood of errors in alignment, mounting, and cable routing. A well-defined sequence of mounting, positioning, and verification steps not only helps maintain assembly quality but also aims to ensure consistency when the process is repeated on a larger scale. Before assembling the real components, the sequence was tested and improved using full-scale 3D printed mockups of the HU components [98]. These mockups provided a safe way to examine the mechanical interfaces, check clearances, and adjust handling procedures without risking damage to sensitive hardware. It allowed verification that the assembly steps from ladder installation to the positioning of power and readout boards could be carried out efficiently under realistic conditions. The insights gained from these mockup trials were used to establish the final protocol, which serves as a guideline for the assembly with real components, while the complete procedure with actual hardware is still to be carried out. The Integration and Assembly Protocol, detailing preparation, mounting, and verification, is outlined below.

6.1 Mounting and the integration protocol

The integration process begins with positioning the C-frame mounting frame (CFMF), which serves as the primary mechanical support. The frame is adjusted to match the

CAD-specified height for the respective C-frame variant. These adjustments are carried out manually with a measuring tape and verified at multiple points to minimize deviations. For secure mounting, sliding wagons and 3D-printed rail adapters are secured together as seen in figure 6.1.1, and then are mounted along the upper and lower edges of the frame and initially fastened loosely with screws.

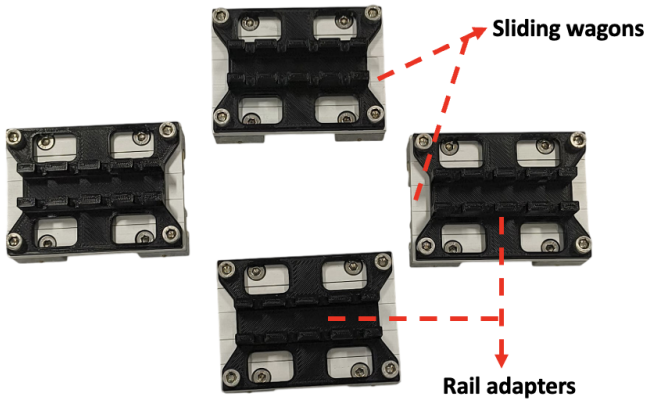

Figure 6.1.1: The sliding wagons with attached 3D-printed rail adapters.

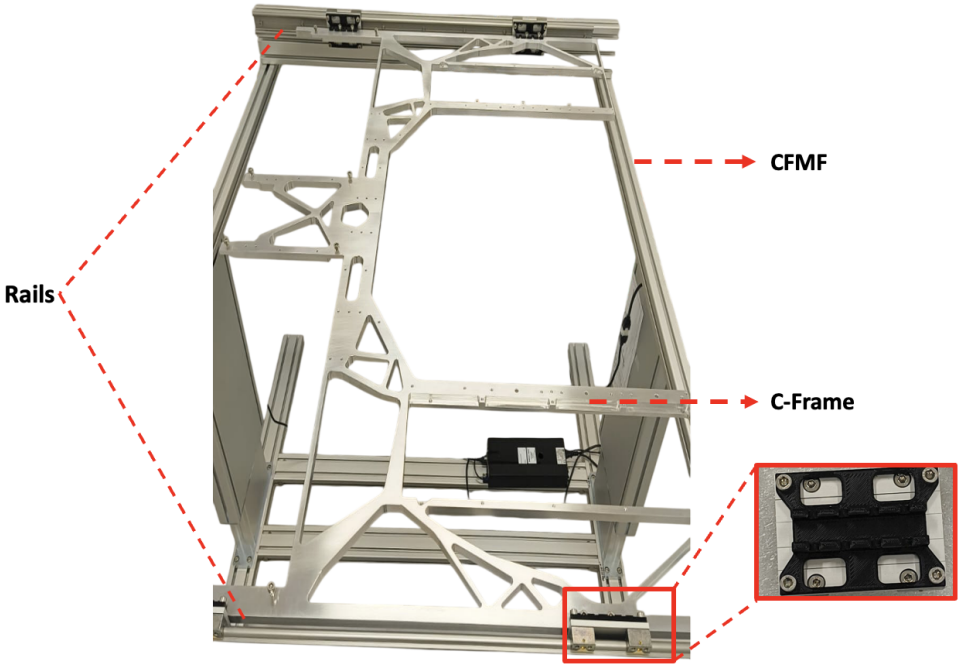

Figure 6.1.2: C-frame guided along rails on sliding wagons.

The C-frame is then carefully guided along the rails using the sliding wagons to ensure smooth insertion, as seen in figure 6.1.2. If necessary, minor adjustments are made to achieve precise alignment. This process may be repeated as needed to ensure that the C-frame is stable and properly aligned at all mounting points.

The mounting process is completed by performing a final verification of the height, orientation, and alignment of the frame. By carefully following a stepwise procedure, this ensures precise and safe assembly while facilitating efficient installation of ladders and FEEs, without introducing mechanical stress or misalignment. Once the C-frame is stable and the adapters are tightened, it is moved horizontally.

6.1.1 Installation of Thermal and Peripheral Components

Following the mechanical setup, the thermal management and peripheral systems are integrated to ensure the HU operates reliably under experimental conditions. Since the detector electronics are highly sensitive to temperature fluctuations, dedicated measures are implemented to dissipate heat during continuous operation and prevent thermally induced failures.

The thermal cooling blocks are mounted first on the HU, while the peripheral components are represented with 3D-printed models [100]. These models allow verification, including checking that the cooling plates specified mounting holes align correctly, ensuring that components fit properly, and that no size or dimensional issues arise when mounting the real parts. This step is necessary to detect any misalignments at an early stage, to observe how the handling works in practice, and to evaluate how easily other parts can be mounted around them during assembly.

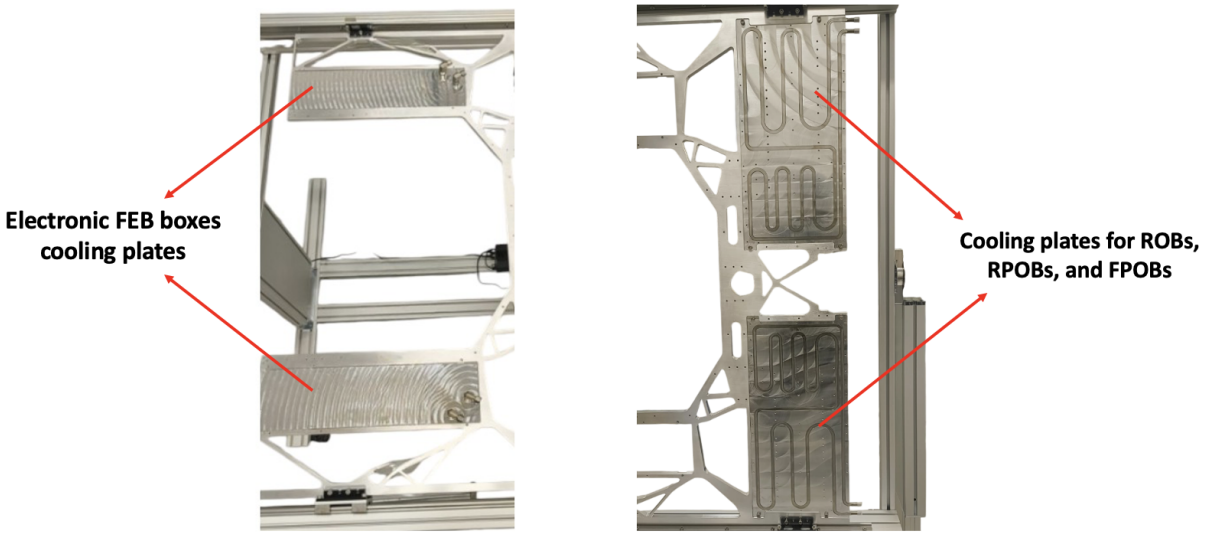

Figure 6.1.3: Four aluminum cooling plates mounted on the C-frame to provide thermal management for FEBs and peripheral components.

Four aluminum cooling plates are arranged within the structure, with one positioned above and one below for the FEBs, and one above and one below the peripheral components, as shown in figure 6.1.3. Aluminum is selected for its high thermal conductivity and mechanical strength, enabling efficient heat removal without adding significant weight. In the mockup, the cooling block primarily represents the actual thermal setup.

Thermal interfaces are installed following the placement of the cooling plates. Subsequently, the peripheral components, such as the ROBs, PPOBs, and FPOBs, are mounted on their respective interfaces as seen in figure 6.1.4, ensuring close thermal coupling and minimizing temperature gradients across the unit. Even in the mockup, ensuring proper contact is important to replicate realistic assembly constraints and prepare the unit for full integration with active electronics.

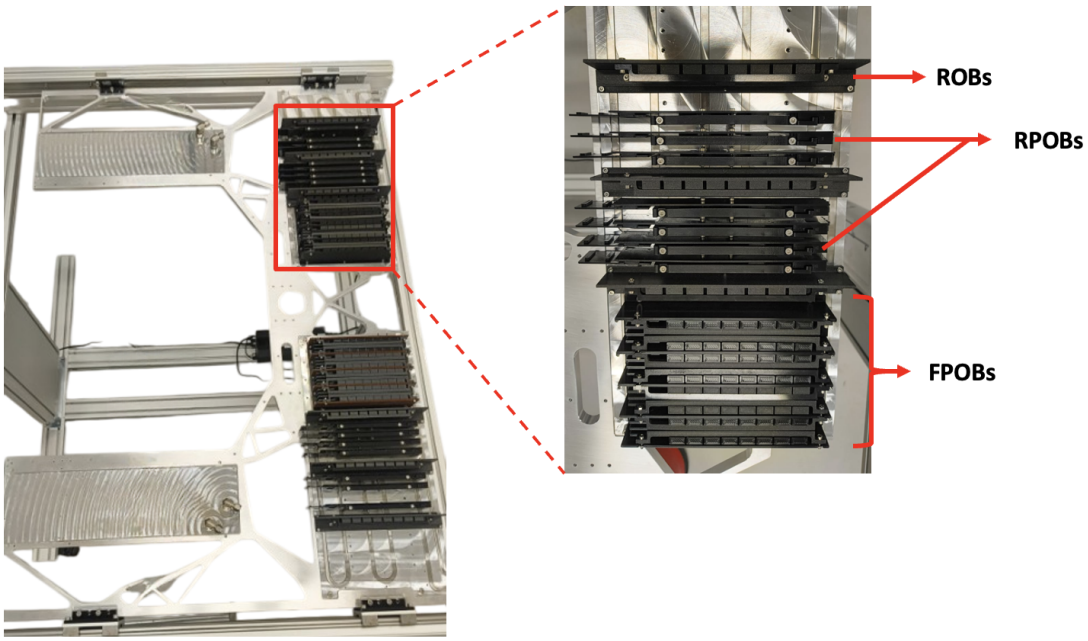

Figure 6.1.4: Arrangement of ROBs, RPOBs, and FPOBs on the C-frame.

6.1.2 Ladder Installation Procedure

The installation of ladders onto the C-frame is performed sequentially, starting from the open side and progressing toward the closed side (see fig 6.1.5a). Each ladder is carefully handled using a specially designed pick-up tool that prevents mechanical damage during installation. Proper handling is essential to maintain the delicate structure of the ladder and avoid misalignment. Initially, the ladder is secured at its bearing points and then fixed through the FEB boxes as shown in figure 6.1.5b. This holds the ladder firmly in place and prevents mechanical deformation that could compromise the alignment of the sensor modules. Ensuring stable positioning at this stage is critical, as even minor deviations can affect the overall performance of the sensors and ladder. Once the ladders are properly secured, the read-out cables are routed to the ROBs and RPOBs, while power cables are routed to their respective FPOBs (see fig 6.1.6).

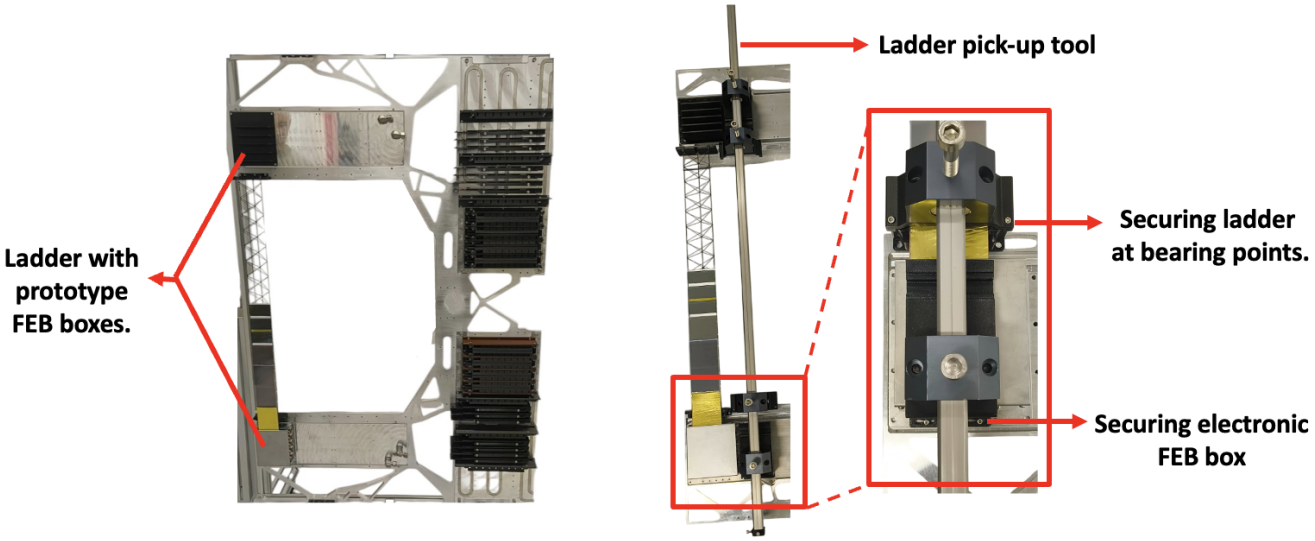

Figure 6.1.5: (a) Sequential placement of ladder and FEB box from the open side (left side). (b) Securing the ladder and FEB box using the pick-up tool (right side).

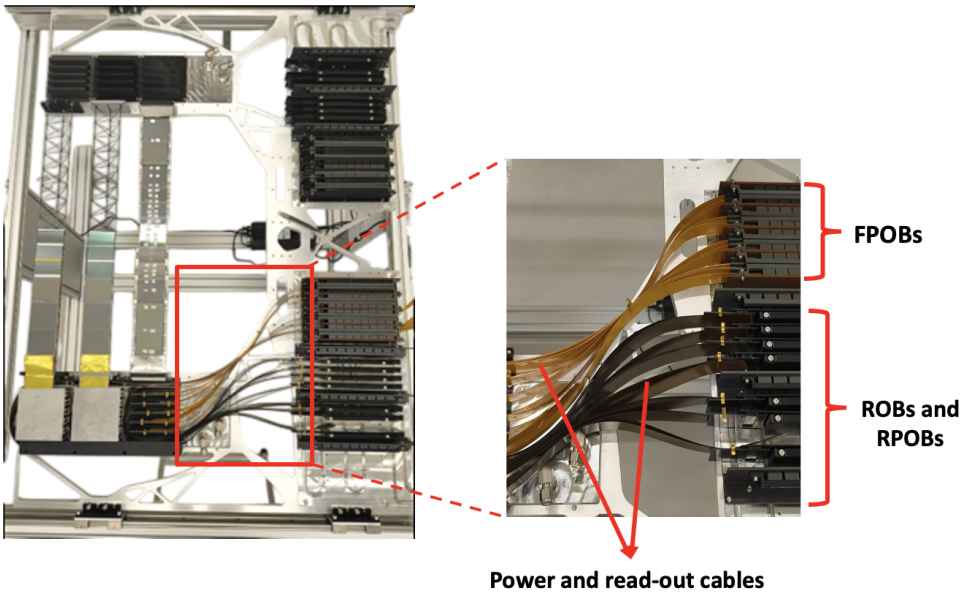

Figure 6.1.6: Routing of cables to the corresponding peripheral components.

After completing all electrical connections, the cable duct for the read-out cables is installed to organize and secure the cables. Throughout the process, attention is given to minimizing cable tension and maintaining proper separation between power and read-out lines to reduce interference and ensure reliable signal transmission. This systematic procedure is repeated for each ladder sequentially along the C-frame. Applying this method throughout ensures mechanical stability, accurate alignment, and proper functioning of the detector.

6.1.3 Cable Connection Sequence

The cable routing follows a structured and efficient flow to ensure stability and guide further connections. In this cabling exercise, only the FEBs were placed in the FEB

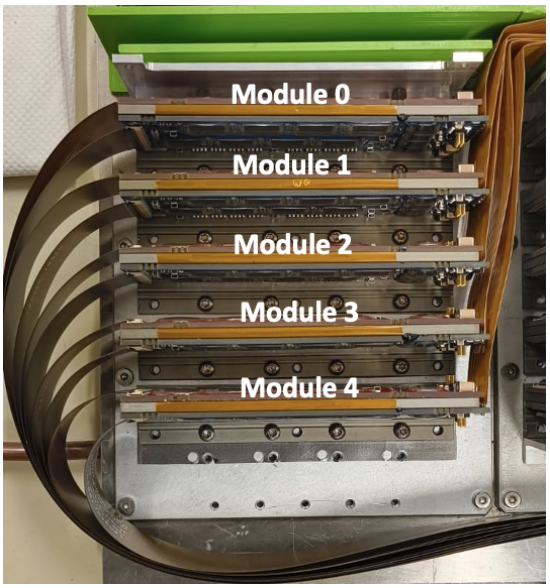

Figure 6.1.7: Sequential connection of data and power distribution cables across the modules of FEB box 1.

boxes, without the sensor modules and microcables; these FEBs are treated as representative modules, allowing the routing procedure to be practiced safely before full integration with assembled ladders and sensors. Data cable routing starts from the left side at module 4 (bottom of the FEB box) and proceeds sequentially

through modules 3, 2, 1, and 0 as seen in figure 6.1.7. For each module, the readout cables are guided below the FEB box to the corresponding ROBs and RPOBs. This is followed by soldering the power distribution cables on the right side (see fig 6.1.7) of the FEB box, starting from module 0 at the top of the FEB box and continuing sequentially through modules 1, 2, 3, and 4. For each module, the cables are guided above the FEB box to the respective FPOBs. This ordered routing pattern is then applied to all subsequent FEB boxes, ensuring that the connections follow a uniform path.

As shown in figure 6.1.8, the cabling sequence was practiced on the remaining FEB boxes. For the second FEB box, connecting the data cables to the modules was slightly more challenging due to the narrow openings. To manage this, the cables were pre-bent and guided carefully through the modules to fit properly while avoiding additional mechanical stress; however, the process remained feasible with proper attention.

In contrast, soldering the power cables to the modules was relatively simple, as the connectors were on the opposite side providing easier access and less mechanical constraint before the next ladder was installed. During this exercise, a third FEB box was mounted on the C-frame to practice soldering of power cables, under realistic assembly conditions (see fig 6.1.9). This practice allowed the procedure to be safely refined before applying it to fully assembled ladders and sensor modules. In the actual setup, both data and power cable connections are expected to remain manageable due to improved accessibility. Finally, cable ducts were installed to secure all data cables, maintaining uniform separation, minimizing overlap and mechanical stress, and improving reliability and ease of future maintenance.

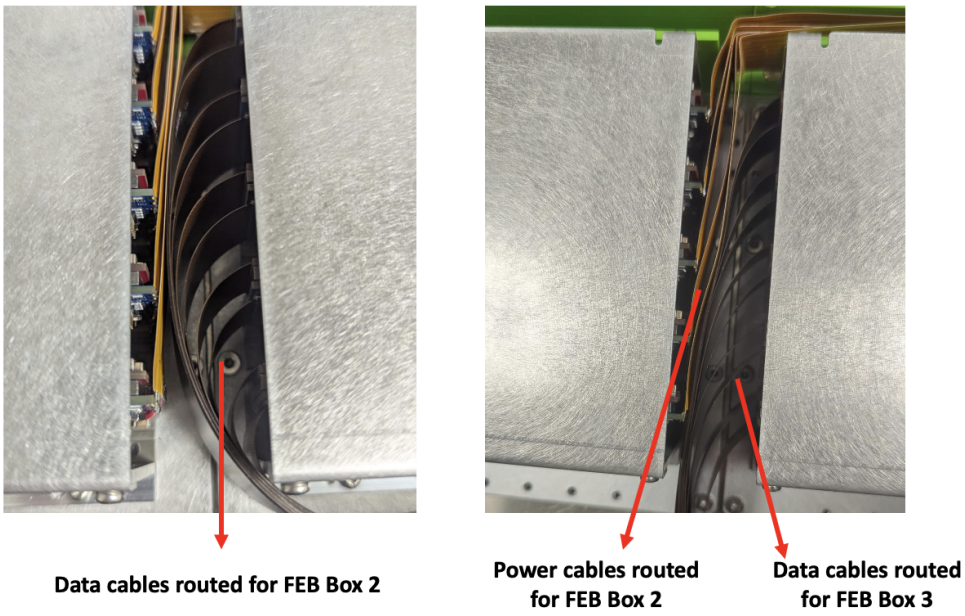

Figure 6.1.8: Sequential connection of data and power distribution cables across the modules of FEB boxes 2 and 3.

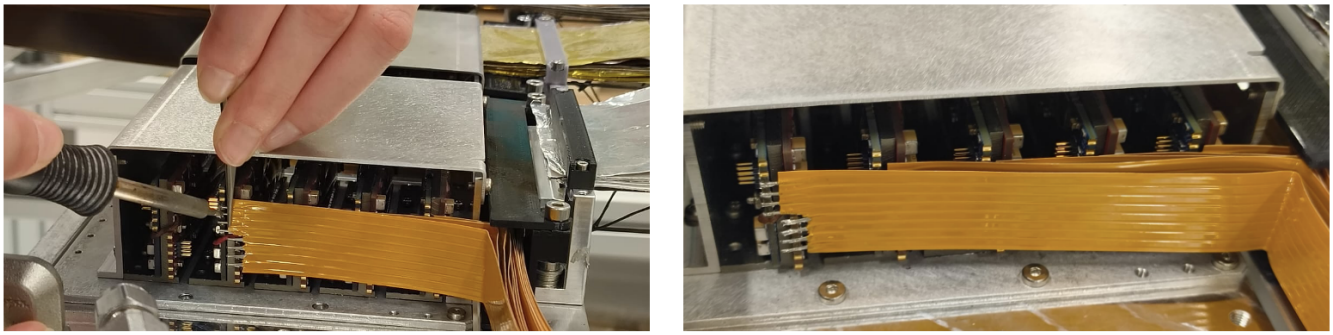

Figure 6.1.9: Soldering power cables on the third FEB box mounted on the C-frame.

After completing the routing, functional tests were performed on the modules to confirm correct cable connections, routing flow, and signal integrity, as discussed in the next section. This approach provides a structured and reliable framework for cable installation, verification, and maintenance across all modules, while accommodating minor routing challenges at the inner FEB boxes. This approach provides a structured and reliable framework for cable installation, verification, and maintenance across all modules, while accommodating minor routing challenges at the inner FEB boxes.

6.2 Functional Testing and Powering of FEB Boxes with FPOB

After the cable routing procedure was completed, the modules underwent functional testing to confirm proper cable connections, assess signal integrity, and verify that the cabling sequence could be reliably implemented in the actual detector setup. Two FEB boxes were tested to measure their noise performance (ENC), confirming that the cabling protocol functions as intended. Additionally, the tests provided an opportunity to evaluate the routing of data and power cables, particularly in compact areas of the inner FEB boxes where pre-bending was necessary. This exercise confirmed that the slight bending required does not compromise the performance of the modules. Overall, these tests validated the cabling procedure and confirmed reliable practices for installation and verification.

Powering of the modules was achieved by soldering the power cables to Sumida connectors, which were then plugged into the FPoB. The FPoB distributes stable, regulated voltages to the modules via FEAST modules and LDO regulators. The FPoB is connected to a low-voltage supply delivering slightly below 12 V, ensuring safe operation. Data cables were connected to EMU boards, while modules were powered individually through the FPoB, without ladders or additional detector components. Both the FPoB and FEB boxes were mounted on their respective cooling plates, with active thermal management provided by a LAUDA chiller, enabling complete powering of the modules while maintaining effective cooling of the cables, thereby ensuring robust thermal management throughout the system.

Functional evaluation included monitoring the equivalent noise charge (ENC), VDDM voltage stability, and temperature of the ASICs. The ENC was measured for all operating ASICs, and the values were consistent with theoretical expectations. ENC plots for all modules of FEB Boxes 1 and 2 are shown in figures 6.2.1 – 6.2.10. The prototype electronics FEB Boxes were used to study the equivalent noise charge (ENC) of all ASICs across ten modules, complementing the functional evaluation presented in Section 5.4. The ENC average values were calculated across all 1024 channels, with typical ASIC noise around ≈ 350 e. independent of the setup.

The average ASIC noise performance was first measured on FEB Box 1 across five modules. Modules 0 and 1. One p-side ASIC in Module 0 failed, with the affected channels indicated in the plot, while Module 1 performed as expected. Modules 2, 3, and 4. Module 2 performed as expected. In Module 3, two p-side and three n-side ASICs failed, with the affected channels indicated in the plot, and in Module 4, four p-side ASICs failed while the fifth ASIC exhibited highly irregular ENC behavior across channels. Next, the average noise performance was measured on FEB Box 2. Modules 0 and 1, both performing as expected. Modules 2, 3, and 4. Modules 2 and 4 performed as expected, while in Module 3, three ASICs failed: two are indicated in the plot, and the third exhibited highly irregular ENC behavior across channels. All ASIC failures were cross-checked via their hardware addresses, confirming that they were due to corrupted registers rather than mechanical damage to the cables. Overall, despite these few ASIC failures, the noise performance of all modules met expectations, confirming the validity of the FEB Box design and the cable routing configuration across both FEB boxes.

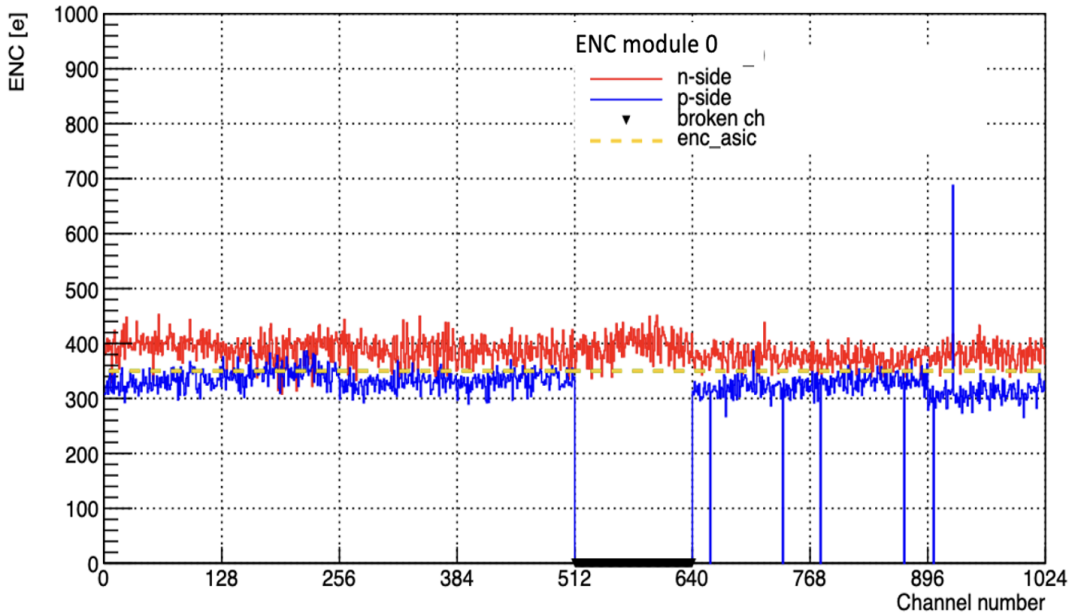

Figure 6.2.1: Average ASIC noise performance for Module 0 of FEB Box 1.

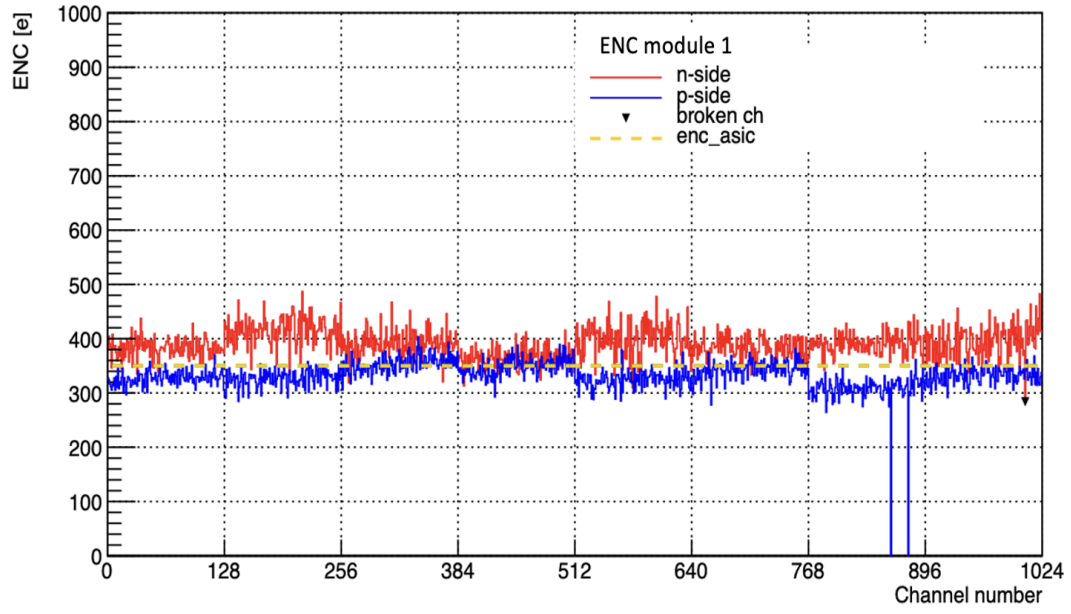

Figure 6.2.2: Average ASIC noise performance for Module 1 of FEB Box 1.

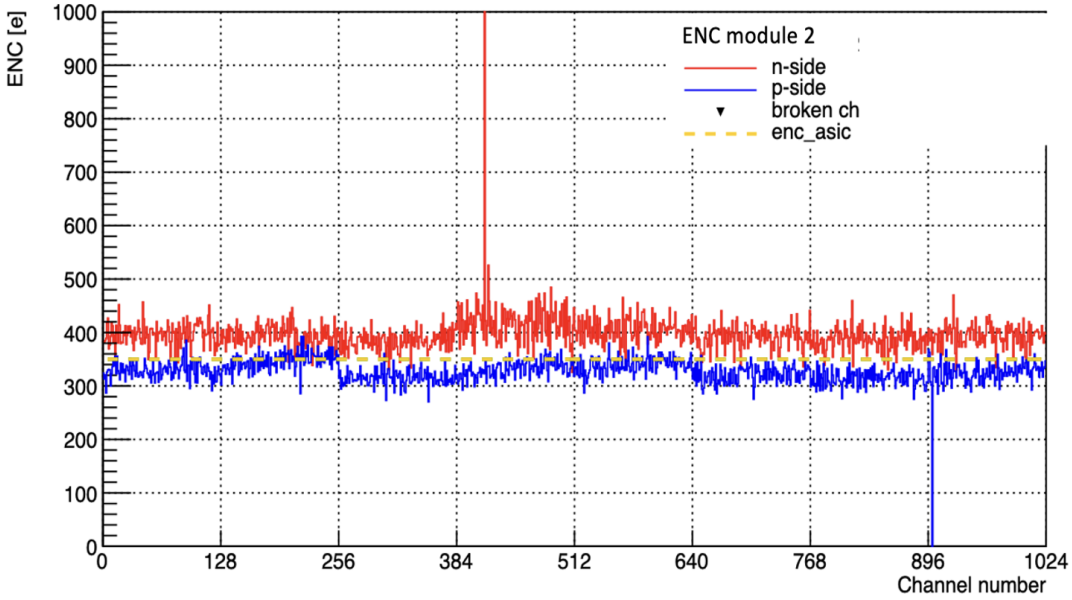

Figure 6.2.3: Average ASIC noise performance for Module 2 of FEB Box 1.

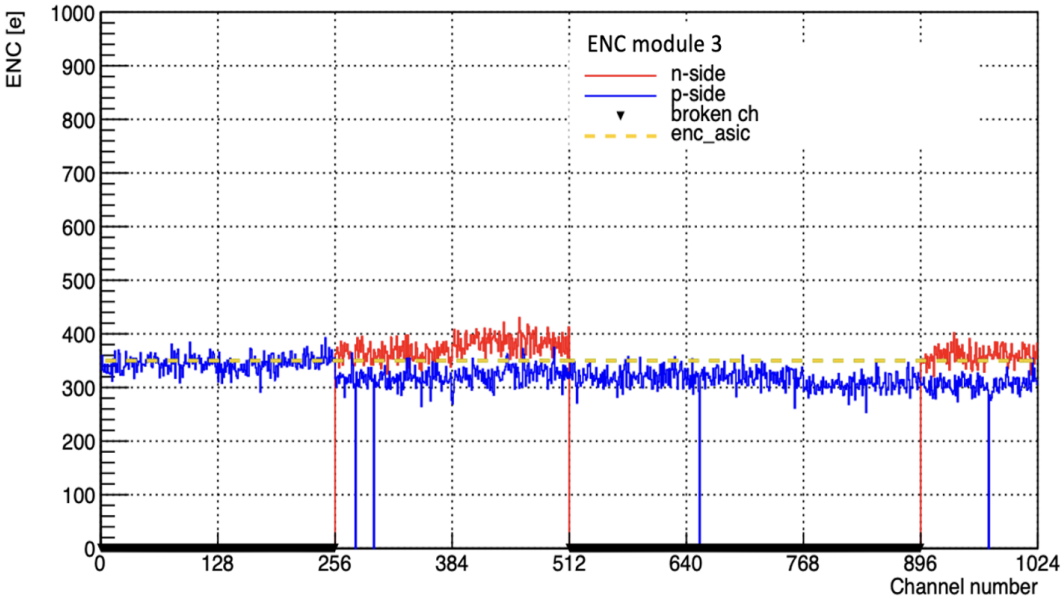

Figure 6.2.4: Average ASIC noise performance for Module 3 of FEB Box 1.

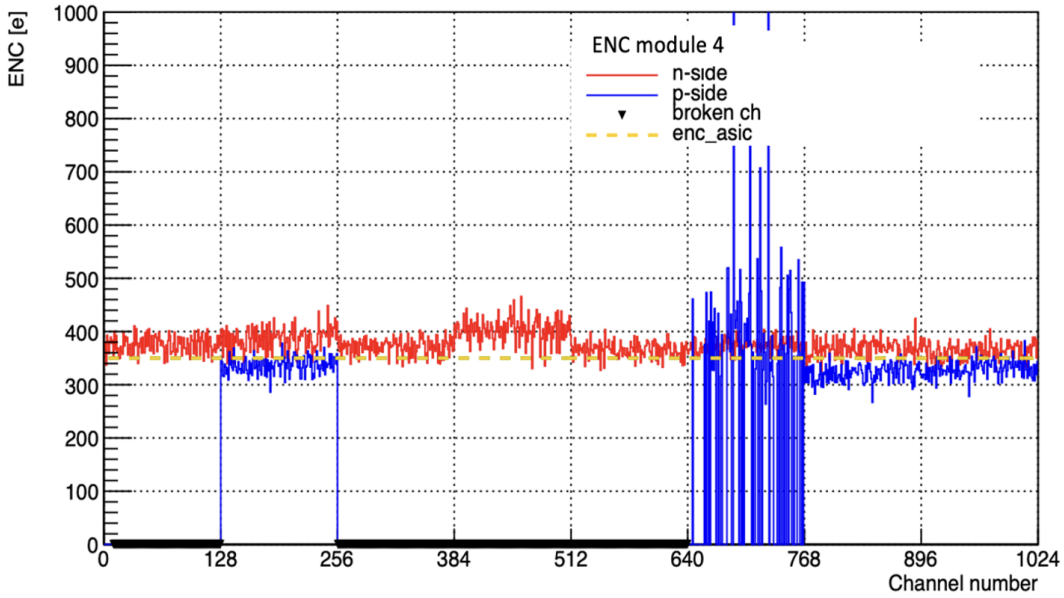

Figure 6.2.5: Average ASIC noise performance for Module 4 of FEB Box 1.

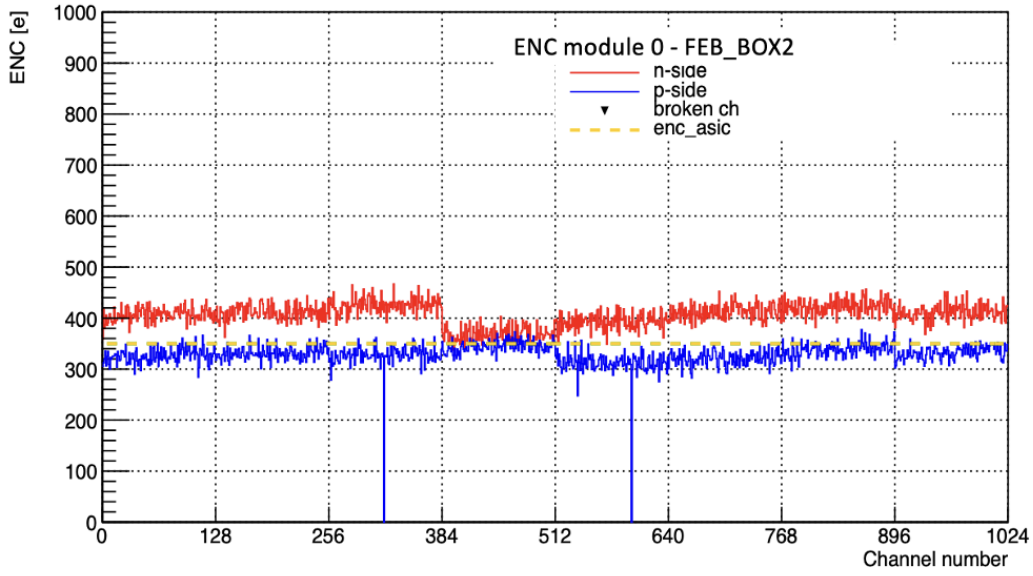

Figure 6.2.6: Average ASIC noise performance for Module 0 of FEB Box 2.

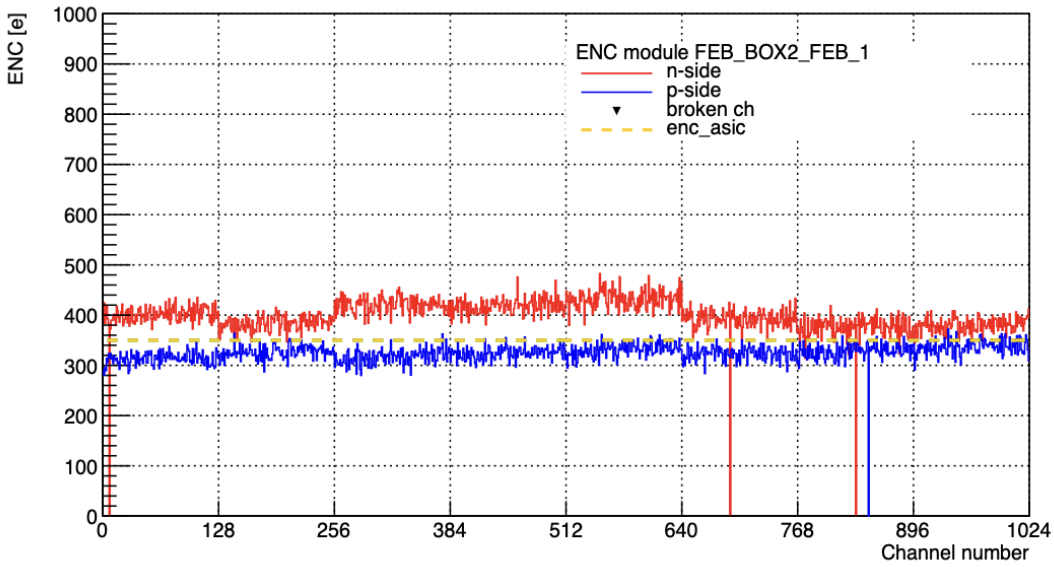

Figure 6.2.7: Average ASIC noise performance for Module 1 of FEB Box 2.

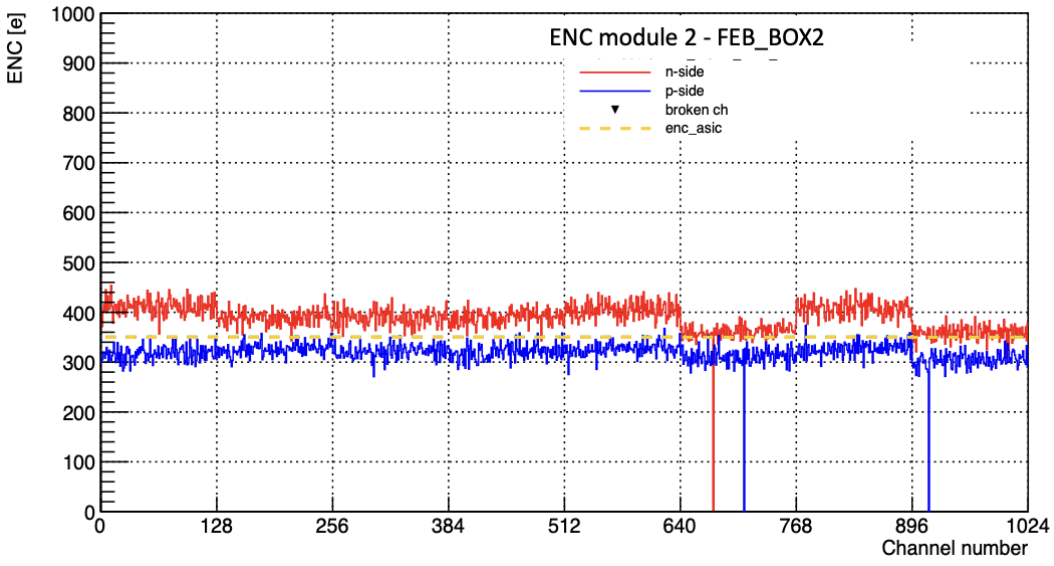

Figure 6.2.8: Average ASIC noise performance for Module 2 of FEB Box 2.

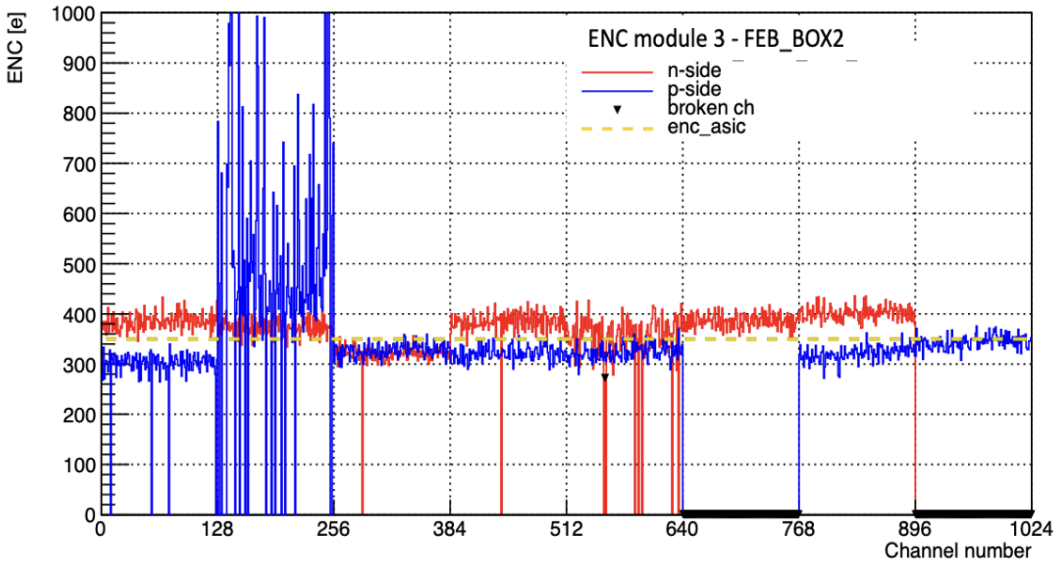

Figure 6.2.9: Average ASIC noise performance for Module 3 of FEB Box 2.

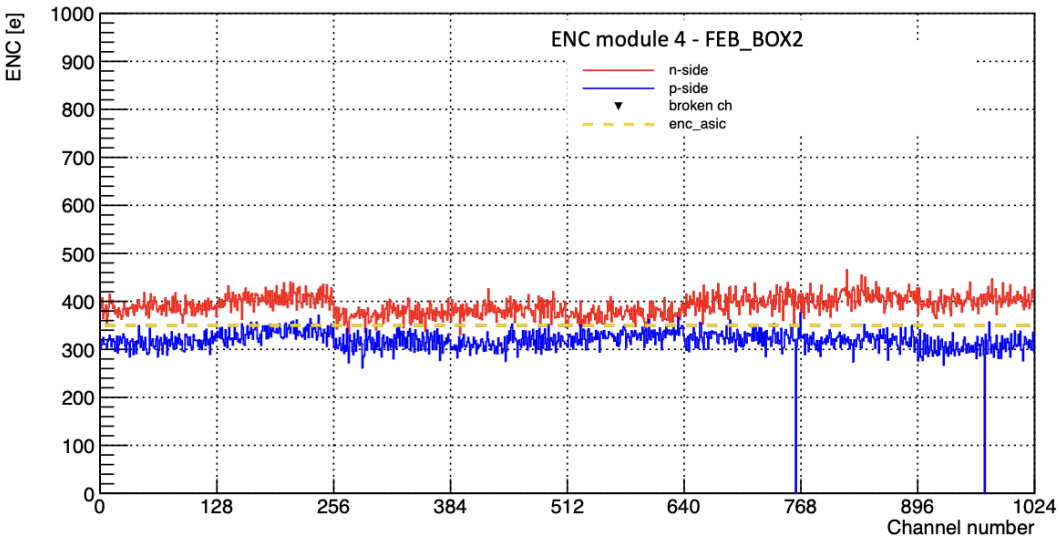

Figure 6.2.10: Average ASIC noise performance for Module 4 of FEB Box 2.

Thermal imaging was performed on all modules of FEB Box 1 as an additional precaution to verify the temperature distribution, identify potential hotspots, and confirm that all ASICs operated within safe thermal limits throughout the tests. FEB Box 1 was chosen as a typical module to allow a detailed analysis before extending tests to other boxes. Appropriate emissivity settings were applied to ensure measurement accuracy. The observed discrepancy of 10–15 °C is expected, as it arises partly from the chosen emissivity and because the thermal camera measures the surface temperature of the ASICs, whereas the configured temperatures reflect their operational heating. All ASICs in the modules remained well below the target operating temperature of 60 °C. Quantitative thermal results for FEB Box 1 with representative thermal images corresponding to the measurements captured using a thermal camera are summarized in figures 6.2.11 - 6.2.15. These specifically show the thermal images of the n-side and p-side for Modules 0–4 of FEB Box 1, respectively. The temperatures obtained from the measurements of the thermal camera are presented in Tables 4 - 8, alongside the temperatures recorded during the configuration of the tests. The thermal images show no significant hotspots across any of the modules, indicating that the thermal management, including the system's inherent cooling setup, was effective and ensured safe operation of all modules under the applied test conditions. The observed temperature differences between the thermal camera measurements and the configured test temperatures, as seen in the tables, remain within acceptable limits.

Furthermore, these thermal measurements provided a visual assessment of relative temperatures across modules, reinforcing that all ASICs remained within safe operating limits. The tests highlighted practical lessons for integration. The cabling protocol proved effective even under limited space constraints, and pre-bending of data cables did not significantly affect noise performance. These results confirm that cable routing in confined spaces is feasible. Power distribution cables remained accessible, and the FPoB successfully supplied stable voltages, validating its suitability for real detector operation. While additional tests on more FEB boxes would strengthen statistical confidence, these preliminary results confirm the methodology and provide a foundation for future integration of FEBs with complete detector modules.

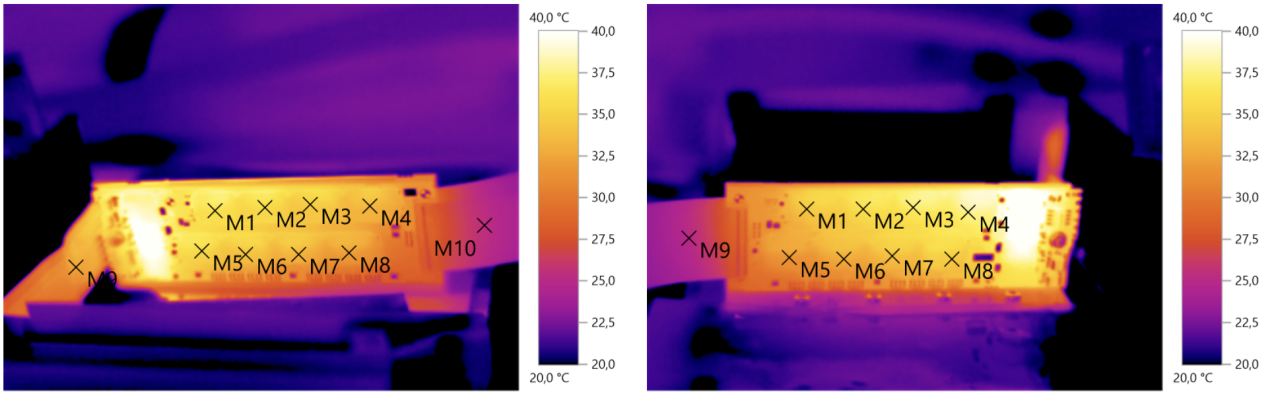

Figure 6.2.11: Thermal images of Module 0: n-side(left) and p-side (right).

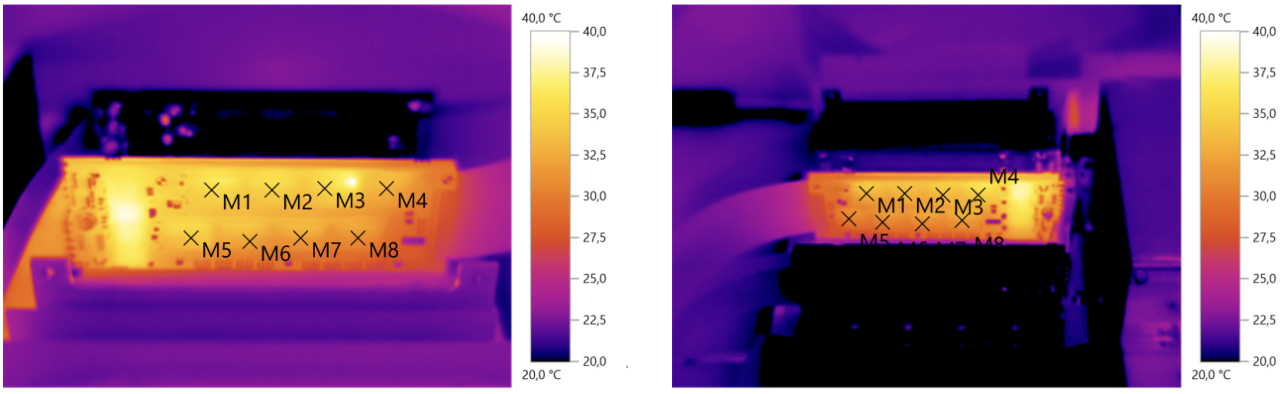

Figure 6.2.12: Thermal images of Module 1: n-side(left) and p-side (right).

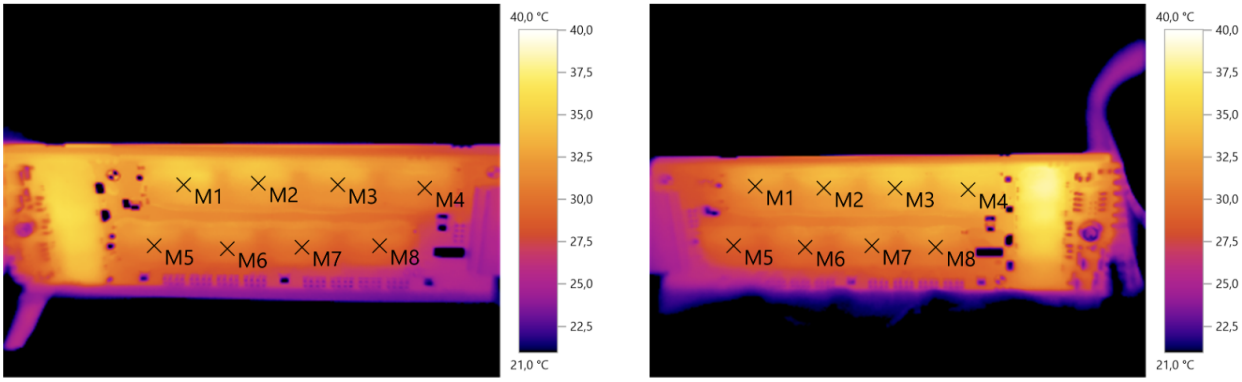

Figure 6.2.13: Thermal images of Module 2: n-side(left) and p-side (right).

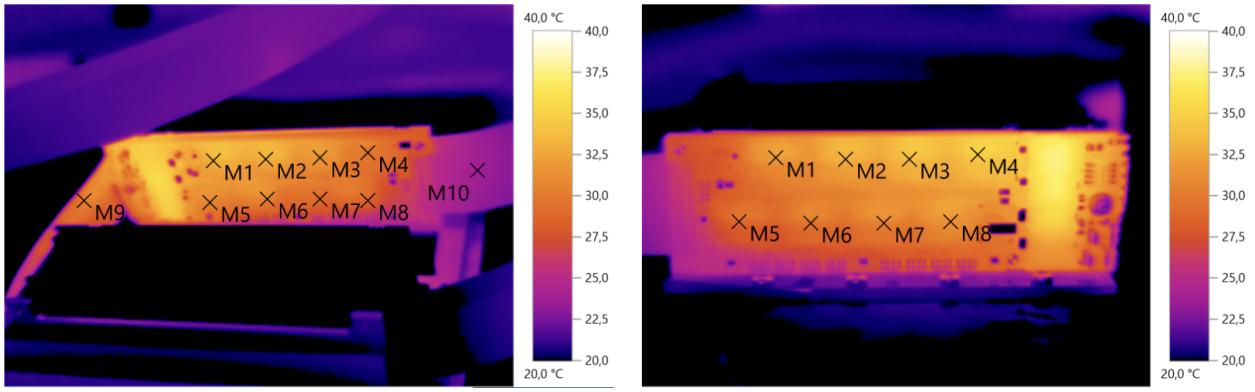

Figure 6.2.14: Thermal images of Module 3: n-side(left) and p-side (right).

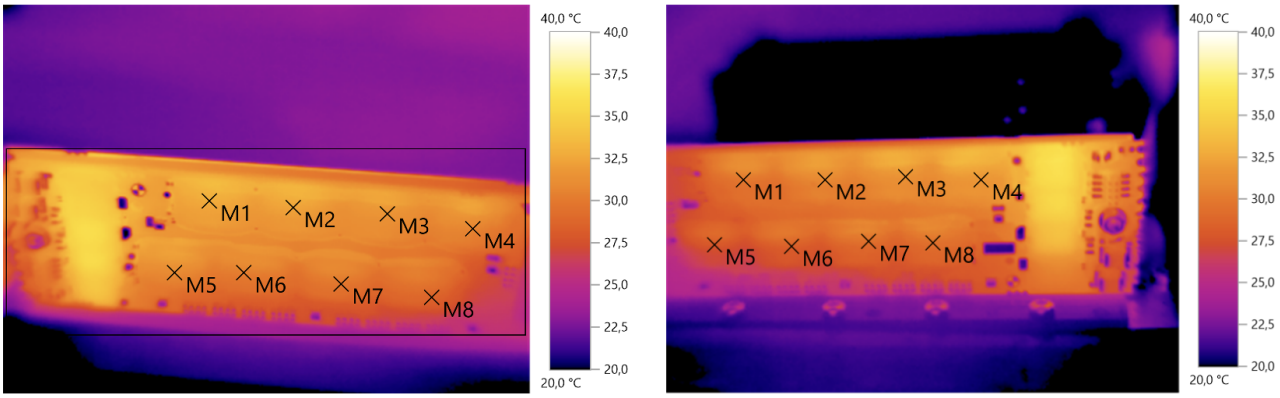

Figure 6.2.15: Thermal images of Module 4: n-side (left) and p-side (right).

POLARITY	HW ADDRESS	Configured Temperature (°C)	Temperature Recorded by Thermal Camera (°C)
P	0	44.4	34.5
P	1	44.4	36.1
P	2	53.9	37.1
P	3	47.5	37.8
P	4	47.5	31.8
P	5	-	32.7
P	6	50.7	34.0
P	7	44.4	34.5
N	0	47.5	36.2
N	1	44.4	35.7
N	2	47.5	34.8
N	3	34.9	33.6
N	4	50.7	35.5
N	5	50.7	34.1
N	6	44.4	33.3
N	7	47.5	32.2

Table 4: Thermal temperatures and configured test temperatures of Module 0 of FEB BOX 1 for P-side and N-side ASICs.

POLARITY	HW ADDRESS	Configured Temperature (°C)	Temperature Recorded by Thermal Camera (°C)
P	0	38.0	33.4
P	1	47.5	33.3
P	2	38.0	33.7
P	3	38.0	34.9
P	4	41.2	30.3
P	5	50.3	30.5
P	6	47.5	30.9
P	7	50.3	32.1
N	0	51.2	32.7
N	1	44.4	32.4
N	2	53.9	31.6
N	3	57.1	31.2
N	4	50.7	31.4
N	5	47.5	30.1
N	6	47.5	30.5
N	7	53.5	38.7

Table 5: Thermal temperatures and configured test temperatures of Module 1 of FEB BOX 1 for P-side and N-side ASICs.

POLARITY	HW ADDRESS	Configured Temperature (°C)	Temperature Recorded by Thermal Camera (°C)
P	0	50.7	31.5
P	1	44.4	33.0
P	2	53.9	33.5
P	3	43.5	34.2
P	4	47.5	38.6
P	5	57.1	49.6
P	6	53.9	30.5
P	7	57.1	32.5
N	0	44.4	32.7
N	1	44.4	32.4
N	2	48.0	31.6
N	3	44.4	41.2
N	4	47.5	44.2
N	5	55.1	30.5
N	6	50.7	45.7
N	7	47.5	48.0

Table 6: Thermal temperatures and configured test temperatures of Module 2 of FEB BOX 1 for P-side and N-side ASICs.

POLARITY	HW ADDRESS	Configured Temperature (°C)	Temperature Recorded by Thermal Camera (°C)
P	0	53.9	32.0
P	1	47.5	33.1
P	2	38.6	33.8
P	3	44.4	34.9
P	4	38.0	39.0
P	5	44.4	39.7
P	6	57.1	30.5
P	7	57.1	41.5
N	0	50.7	33.0
N	1	-	33.0
N	2	-	31.7
N	3	-	40.0
N	4	44.4	40.7
N	5	50.7	30.4
N	6	-	40.9
N	7	-	38.5

Table 7: Thermal temperatures and configured test temperatures of Module 3 of FEB BOX 1 for P-side and N-side ASICs.

POLARITY	HW ADDRESS	Configured Temperature (°C)	Temperature Recorded by Thermal Camera (°C)
P	0	38.0	31.2
P	1	34.9	31.6
P	2	42.0	32.3
P	3	-	33.2
P	4	-	38.1
P	5	-	39.2
P	6	34.9	30.5
P	7	-	44.4
N	0	43.0	32.7
N	1	41.7	32.2
N	2	44.4	31.4
N	3	41.2	41.0
N	4	41.2	42.3
N	5	48	30.4
N	6	46.6	45.0
N	7	42.5	45.1

Table 8: Thermal temperatures and configured test temperatures of Module 4 of FEB BOX 1 for P-side and N-side ASICs.

6.3 Challenges and Limitations

The assembly of the HU required careful planning to ensure that all components could be integrated smoothly and safely. During the early stages of execution, various practical issues were encountered, making it necessary to adjust the initial ideas. The main challenges were the reliability of the 3D-printed mockup parts, the sequence of ladder mounting, and the proper approach to connecting and routing the cables to the FEB boxes. Addressing each of these issues was essential to demonstrate that the assembly procedure could be performed under realistic conditions without compromising either mechanical stability or electrical functionality.

A technical difficulty arose when the 3D printer malfunctioned, causing delays in producing the mockup components. These mockups included peripheral electronics, selected FEB boxes, and cable ducts, which were crucial to recreate realistic assembly conditions before attempting the procedure with the actual components. Repeated printer failures occasionally produced parts that were deformed and unusable for reliable alignment, cable routing practice, or general testing. Several components had to be reprinted. While these problems did not prevent the continuation of tests, they introduced inefficiencies and emphasized how strongly the workflow depends on accurate mockup parts.

Next, the challenge involved the sequence of ladder mounting. In the initial assembly plan, the ladders were intended to be mounted starting from the inner side of the C-frame and progressing outward. This approach initially appeared logical from a mechanical standpoint, as it provided a seemingly straightforward sequence for placing the ladders in order. However, when this sequence was tested using the mockup, it became evident that the arrangement created significant difficulties in accessing the power and data cables. Once the ladders on the inner side were installed, the available space for routing and soldering cables to the ladders became constrained, making proper cable connections challenging. As a result, the ladder mounting sequence was revised to prioritize cable accessibility over the initially proposed mechanical sequence. The revised approach was subsequently adopted, ensuring that sufficient space was available for routing and connecting cables to all modules while maintaining mechanical stability and proper alignment of the ladders.

A third limitation was encountered during the functional testing phase when powering the FEB boxes with the FPoB. One of the Molex connectors responsible for supplying low voltage to the FPoBs was damaged. Although a single FPoB is capable of powering four modules simultaneously, the broken connector limited the testing to only three modules at a time. This incident resulted in additional time for the testing procedure and highlighted the importance of careful handling of the power distribution components. It also emphasized the need to have spare connectors readily available during assembly and commissioning to avoid delays and ensure uninterrupted operation.

Overall, the HU assembly workflow proved to be well-structured and realistic, despite the practical challenges encountered during testing. The importance of mockup tests was highlighted by planning and verification, ensuring that assembly procedures were feasible, cable routes remained accessible, and powering through the FPoB was reliable. These lessons provide valuable pointers for future integration with fully functional components. While minor adjustments may still be necessary when assembling the actual HU with ladders, FEEs, and soldered connections. The step-by-step protocol provides a reliable guide, enabling subsequent assembly steps to proceed efficiently while showing the workflow's effectiveness under realistic conditions.

7 Summary

This work demonstrates that the assembly and integration of the STS half-unit (HU) is technically feasible and operationally reliable. The step-by-step assembly protocol developed in this study, together with functional testing of the FEB boxes, enabled verification of both mechanical alignment and electrical performance. These hands-on exercises provided valuable practical findings and established a clear framework for future HU assemblies.

Mockups of the ladders and other components played a key role in this study, allowing the arrangement of the components on the HU to be evaluated without exposing actual ladders or electronics to risk. FEB boxes were employed to perform cable routing and functional verification. This approach contributed to the identification of potential difficulties in advance, ensured accessibility of all connection points, and allowed accurate execution of assembly steps.

Functional tests with the FEB boxes confirmed that the assembly protocol performed reliably under representative operating conditions. The electrical and thermal performance of the HU was stable, with consistent power delivery to the ASICs, proper communication, and expected configuration throughout the system. Temperature monitoring and noise levels (ENC) remained consistent across modules, indicating that neither the cable layout nor the powering scheme introduced unwanted disturbances and that the electronics operated within expected ranges. Thermal imaging verified that the cooling system maintained the modules safely, with no significant hotspots. Altogether, these results show that the protocol maintains both electrical and thermal integrity, providing a solid foundation for the reliable operation of the HU.

From a broader perspective, several lessons emerged from these exercises. They revealed unexpected difficulties and provided opportunities to refine the assembly protocol without risk. Ensuring easy access for cable handling remained a central factor in the integration strategy. Handling of connectors and cables is crucial, as clear routing paths and easy access to connectors are necessary to carry out the assembly smoothly and accurately.

Even small imperfections can affect test continuity and overall assembly performance, highlighting the need for careful attention to both mechanical and electrical aspects. These experiences highlighted that successful integration requires a balance between mechanical precision and practical adaptability, with lessons learned from each iteration contributing to improved assembly procedures and reliability.

Overall, this study shows that the STS HU can be assembled reliably, maintaining both structural stability and consistent functional performance. The assembly protocol, particularly the cable routing procedure, was carefully tested and validated through functional evaluations, providing detailed insights into component handling, connection integrity, quality assurance, and performance verification. This study establishes a strong foundation for future HU integrations and contributes to defining standardized best practices for detector assembly and integration within the CBM STS.

The upcoming work will focus on integrating the half units into multi-station sections and assessing their impact on overall system performance, including mechanical stability, alignment, and detector functionality. This will involve developing and implementing procedures for assembling, aligning, and validating HUs, along with quality assurance protocols for integrated assemblies, including mechanical checks, alignment verification, and performance testing under realistic conditions. Using full-scale mockups and functional prototypes, integration steps such as mounting, cabling, and thermal connection will be carried out and evaluated for their effect on system performance.

In this next phase, the goal is to build and qualify larger STS structures that bring the system closer to its final detector configuration. The focus will be on developing practical assembly and installation strategies, optimizing power and cooling connections, and ensuring stable readout performance once everything is integrated. The work will also check that the assembled structures remain stable and reproducible during operation. Altogether, these activities will help finalize the integration procedure and prepare the STS for installation and commissioning in the CBM experiment.

8 References

1. Hobbs, B. (2017, July 15). The Standard Model of particle physics is brilliant and completely flawed. ABC Science. https://www.abc.net.au/news/science/2017-07-15/the-standard-model-of-particle-physics-explained/7670338

2. M. Thomson, Modern Particle Physics, 2013 edition.

3. E.S. Fraga, "QCD under extreme conditions: an informal discussion," in Proceedings of the 2013 CERN–Latin-American School of High-Energy Physics, Arequipa, Peru, 6–19 March 2013, edited by M. Mulders and G. Perez, CERN-2015-001, pp. 157–167, https://cds.cern.ch/record/1617402/files/157-167%20Fraga.pdf

4. R.T. Cahill, On the Importance of Self-Interaction in QCD, Australian Journal of Physics, vol. 44, no. 3, pp. 105–134, 1991, https://www.publish.csiro.au/ph/pdf/PH910105

5. D.J. Gross, The discovery of asymptotic freedom and the emergence of QCD, Reviews of Modern Physics, vol. 77, pp. 837–860, 2005, https://journals.aps.org/rmp/pdf/10.1103/RevModPhys.77.837

6. S. Bethke, Experimental Tests of Asymptotic Freedom, Progress in Particle and Nuclear Physics, vol. 58, pp. 351–386, 2007, https://arxiv.org/abs/hep-ex/0606035

7. P. Foka and M.A. Janik, An overview of experimental results from ultra-relativistic heavy-ion collisions at the CERN LHC: hard probes, Reviews in Physics, vol. 1, pp. 172–194, 2016, https://arxiv.org/abs/1702.07231

8. A. Monnai, G. Pihan, B. Schenke, and C. Shen, Four-dimensional QCD equation of state with multiple chemical potentials, Physical Review C, vol. 101, no. 6, 064902, 2020, https://arxiv.org/abs/2406.11610v2

9. M.H. Nielsen, What "is" an Equation of State?, Journal of Petroleum Technology, July 21, 2020, https://jpt.spe.org/twa/what-equation-state

10. Z. Ji, J. Chen, and G. Wu, The Equation of State of Neutron Stars: Theoretical Models, Observational Constraints, and Future Perspectives, arXiv:2505.05241v3 [nucl-th], 5 July 2025, https://arxiv.org/pdf/2505.05241

11. R. Kumar, V. Dexheimer, and J. Jahan, Neutron stars and Constraints for the Equation of State of Dense Matter, arXiv:2503.23413v1 [nucl-th], 30 Mar 2025, https://arxiv.org/pdf/2503.23413

12. A. Bauswein, O. Just, H.-T. Janka, and N. Stergioulas, Neutron-star Radius Constraints from GW170817 and Future Detections, https://iopscience.iop.org/article/10.3847/2041-8213/aa9994

13. N. Chamel, A.F. Fantina, J.M. Pearson, and S. Goriely, Phase transitions in dense matter and the maximum mass of neutron stars, Astronomy Astrophysics, vol. 553, A22, 2013, https://arxiv.org/abs/1205.0983

14. J. Li, T. Guo, J. Zhao, and L. He, Do we need dense matter equation of state in curved spacetime for neutron stars?, *Physical Review D*, vol. 106, no. 8, 083021, 2022, https://arxiv.org/pdf/2206.02106

15. F. Özel, A. Psaltis, D. Narayan, and J. Santos, Masses, radii, and the equation of state of neutron stars, 2016, https://arxiv.org/pdf/1205.6871

16. M. Vivas Albornoz, The First Release of ATLAS Open Data for Research, PoS(ICHEP2024)1172, https://pos.sissa.it/476/1172/pdf

17. ATLAS Collaboration, Introduction to heavy-ion physics, CERN Open Data Portal, https://opendata.atlas.cern/docs/documentation/introduction/heavy_ions

18. U.S. Department of Energy. (n.d.). DOE Explains...Quarks and Gluons. https://www.energy.gov/science/doe-explainsquarks-and-gluons

19. CERN, Heavy ions and quark-gluon plasma, https://home.cern/science/physics/heavy-ions-and-quark-gluon-plasma

20. MIT News, Experimental recreation of quark-gluon plasma, https://news.mit.edu/2010/exp-quark-gluon-0609

21. J. Rafelski, Connecting QGP-Heavy Ion Physics to the Early Universe, https://arxiv.org/abs/1306.2471

22. Brookhaven National Laboratory, Relativistic Heavy Ion Collider (RHIC), https://www.bnl.gov/rhic

23. CERN, Large Hadron Collider (LHC), https://home.cern/science/accelerators/large-hadron-collider

24. V. Kekelidze et al., Heavy ion collision experiments at NICA, Proceedings of Science, ICHEP2018, 493, 2019, https://pos.sissa.it/340/493/pdf

25. P. Senger, Astrophysics in the laboratory the CBM experiment at FAIR, Particles, vol. 3, no. 2, pp. 320–335, 2020, https://doi.org/10.3390/particles3020024

26. S. Sarkar, H. Satz, and B. Sinha (Eds.), The physics of the quark-gluon plasma: Introductory lectures, Lecture Notes in Physics, vol. 785, Springer, 2010, https://doi.org/10.1007/978-3-642-02286-9

27. P. Braun-Munzinger and J. Wambach, Colloquium: Phase diagram of strongly interacting matter, Rev. Mod. Phys., vol. 81, pp. 1031–1050, 2009, https://doi.org/10.1103/RevModPhys.81.1031

28. T. Ablyazimov et al., Challenges in QCD matter physics – The scientific programme of the Compressed Baryonic Matter experiment at FAIR, Eur. Phys. J. A 53, 60 (2017), https://arxiv.org/pdf/1607.01487

29. T. Galatyuk, Present and future perspectives in hadron physics at GSI/FAIR, STRONG-2020, GSI/FAIR, 18 June 2024, slides

30. E. Bechtel, Investigation of charm and strangeness production in the CBM experiment, Doctoral dissertation, Goethe University Frankfurt, 2021.

31. A. Meyer-Ahrens, CBM physics program: Strangeness and hypernuclei studies at FAIR, Doctoral dissertation, University of Münster, 2025.

32. H. H. Gutbrod et al., FAIR Baseline Technical Report, GSI Helmholtz Centre for Heavy Ion Research, 2006, report

33. P. J. Spiller et al., Technological Features and Status of the New Heavy-Ion Synchrotron SIS100 at FAIR, Proceedings of IPAC'23, Venice, Italy, May 2023, DOI

34. CBM Collaboration, Technical Design Report for the Compressed Baryonic Matter (CBM) Experiment, GSI Helmholtz Centre for Heavy Ion Research, 2015, report

35. S. Reimann, H. Albers, R. W. Assmann, et al., FAIR Commissioning - Towards First Science, 2025, https://arxiv.org/abs/2510.14948

36. P. Senger, for the CBM Collaboration, Astrophysics in the Laboratory: The CBM Experiment at FAIR, Particles 2020, 3(2), 320–335, https://doi.org/10.3390/particles3020024

37. P. Senger, Astrophysics in the Laboratory - The CBM Experiment at FAIR, 2020, https://arxiv.org/pdf/2004.11214

38. CBM Collaboration, Compressed baryonic matter (CBM), GSI Helmholtz Centre for Heavy Ion Research, site

39. I. Kisel (for CBM STAR Collaborations), Real-Time Event Reconstruction and Analysis in CBM and STAR Experiments, Journal of Physics: Conference Series, vol. 1602, 012006, 2020, paper

40. M. Teklishyn (for the CBM Collaboration), Detectors and Electronics for the CBM Experiment at FAIR, 2025, https://arxiv.org/pdf/2506.20545

41. GSI/FAIR, Compressed Baryonic Matter (CBM), https://www.cbm.gsi.de/

42. A. Rost et al., Beam-Diagnostic and T0 System for the mCBM and CBM Experiments at GSI and FAIR, paper

43. P. Kurilkin, Superconducting dipole magnet for the CBM experiment at FAIR, EPJ Web of Conferences, vol. 138, 12001, 2017, paper

44. P. Gasik, Towards the CBM Experiment at FAIR, CERN Detector Seminar, 24 November 2023, slides

45. P. Klaus, The Micro Vertex Detector of the CBM Experiment, Presentation at the XIIth Quark Confinement and the Hadron Spectrum Conference, 1 September 2016, slides

46. P. Klaus et al., Status of the vertex detector program of the CBM experiment at FAIR, Nuclear Instruments and Methods in Physics Research Section A, vol. 936, 2019, pp. 705-706, paper

47. C. Höhne et al., Technical Design Report for the CBM: Ring Imaging Cherenkov Detector (RICH), GSI, Darmstadt, 2013,https://repository.gsi.de/record/65526

48. C. Höhne (CBM Collaboration), The RICH detector for the CBM experiment at FAIR, Poster presentation, Justus-Liebig University Giessen, Germany, and GSI, Darmstadt, Germany, Poster

49. S. Chattopadhyay et al., Technical Design Report for the CBM: Muon Chambers (MuCh), GSI, Darmstadt, 2015, available online: https://repository.gsi.de/record/161297

50. C. Blume et al., Technical Design Report for the CBM: Transition Radiation Detector (TRD), GSI, Darmstadt, 2018, available online: https://repository.gsi.de/record/217478

51. N. Herrmann et al., Technical Design Report for the CBM: Time Of Flight (TOF), GSI, Darmstadt, 2014, available online: https://repository.gsi.de/record/109024

52. F. Guber and I. Selyuzhenkov et al., Technical Design Report for the CBM: Projectile Spectator Detector (PSD), GSI, Darmstadt, 2015, available online: https://repository.gsi.de/record/109059

53. D. A. Ramirez Zaldivar (for the CBM Collaboration), Performance of the prototype Silicon Tracking System of the CBM experiment tested with heavy-ion beams at SIS18, arXiv:2505.20517 [physics.ins-det], 2025, https://arxiv.org/abs/2505.20517

54. J. M. Heuser et al., Technical Design Report for the CBM Silicon Tracking System (STS), GSI, Darmstadt, 2013, available online: https://repository.gsi.de/record/54798

55. W. F. J. Müller et al., The CBM Silicon Tracking System: Detector design and performance, Nuclear Physics A, vol. 931, pp. 1–10, 2015.

56. W. Müller et al., Integration and commissioning of the CBM Silicon Tracking System, Journal of Instrumentation, vol. 13, no. 10, P10014, 2018.

57. U. Frankenfeld et al., The design and performance of the CBM Silicon Tracking System, Nuclear Instruments and Methods in Physics Research Section A, vol. 763, pp. 1–7, 2014.

58. A. R. Rodríguez et al., Functional characterization of modules for the Silicon Tracking System of the CBM experiment, Nuclear Instruments and Methods in Physics Research Section A, 2024, paper

59. C. J. Schmidt et al., The CBM Silicon Tracking System: Integration and commissioning, Journal of Instrumentation, vol. 12, no. 02, P02023, 2017.

60. U. Frankenfeld et al., Front-end electronics for the CBM Silicon Tracking System, Journal of Instrumentation, vol. 14, no. 03, C03012, 2019.

61. P. Senger et al., Thermal management of the CBM Silicon Tracking System, Journal of Instrumentation, vol. 15, no. 04, C04002, 2020.

62. C. Sturm et al., Radiation hardness of the CBM Silicon Tracking System, Nuclear Instruments and Methods in Physics Research Section A, vol. 888, pp. 1–6, 2018.

63. K. Agarwal, Thermal management (cooling) of the CBM Silicon Tracking System, DPG Bochum 2018, slides

64. I. Panasenko, Development of Electrical Quality Assurance Procedures and Methods for the Silicon Tracking System of the CBM Experiment, Doctoral dissertation, University of Tübingen, 2023.

65. P. Ghosh, Quality Assurances for Silicon Double-Sided Sensors in Silicon Tracker System for CBM Experiment at FAIR, Proceedings paper, PoS (SIS2013) 018, 2013, https://pos.sissa.it/184/018/pdf

66. E. Lavrik et al., Advanced optical quality assurance of silicon micro-strip sensors for the CBM experiment, 2019, https://arxiv.org/pdf/1807.00211

67. M. Teklishyn et al., From 3D to 5D tracking: SMX ASIC-based Double-Sided Micro-Strip detectors for comprehensive space, time, and energy measurements, 2023, https://arxiv.org/pdf/2311.02140

68. M. Teklishyn et al., Minimal material, maximum coverage: Silicon Tracking System for high-occupancy conditions, 2025, https://arxiv.org/pdf/2503.15721

69. J. M. Heuser et al., The high count-rate self-triggering Silicon Tracking System of the CBM experiment, Nuclear Instruments and Methods in Physics Research Section A, 2024, paper

70. Private Conversation with Adrian Rodríguez Rodríguez

71. A. Rodríguez Rodríguez, The CBM Silicon Tracking System front-end electronics, Doctoral dissertation, Johann Wolfgang Goethe University, Frankfurt am Main, 2020.

72. D. Borshchov, Improvement of ultra-light microcables production at LTU, GSI Report Part-NQM-GSI-Report-2016-1, GSI Helmholtz Centre for Heavy Ion Research, 2016, paper

73. A. R. Rodríguez et al., Advancements in the Silicon Tracking System of the CBM experiment: Series production, testing and operational insights, JINST, 20, C03020, 2025, paper

74. J. M. Heuser, Progress with system integration of the CBM Silicon Tracking Detector, DPG Frühjahrstagung, Münster, Germany, 2017.

75. O. Vasylyev, CAD images of CBM components, private communication.

76. S. Mehta et al., Ladder assembly for the Silicon Tracking System of the CBM experiment at FAIR, HADES at FAIR Measurement of di-lepton pairs (e+e-) A, GSI Indico, 2018, poster

77. S. Mehta, Investigation of thermal and structural integrity of modules and ladders of Silicon Tracking System of CBM experiment, doctoral dissertation, Eberhard Karls Universität Tübingen, 2024.

78. V. Kleipa et al., A front-end electronics board to test the assembly procedure of modules for the CBM Silicon Tracking System, GSI Scientific Report 2014-1, NQM-CBM-18, 2014, paper

79. K. Agarwal, Thermal management of the CBM-FAIR's Silicon Tracking System, FTDMT, Tübingen, Germany, 2023, presentation

80. K. Agarwal, Thermal Management of the Silicon Tracking System of the CBM Experiment at FAIR, Eberhard Karls Universität Tübingen doctoral dissertation, 2024.

81. L.M. Collazo Sánchez et al., Module and ladder characterization and burn-in tests of the Silicon Tracking System for the CBM experiment, FAIRNESS 2024, slides

82. L.M. Collazo Sánchez, Module and ladder characterization of the Silicon Tracking System for the CBM experiment, QM2025, poster

83. A. R. Rodríguez Rodríguez, Ladders operation and tests: Production readiness review of CBM-STS modules and ladders, GSI Indico 2024, slides

84. M. Teklishyn and O. Vasylyev, Subsequent STS integration steps, GSI Darmstadt, 2024, slides

85. O. Vasylyev, Mechanical concept, design, and prototyping of the STS for the CBM Experiment at FAIR, Forum on Tracking Detector Mechanics, Marseille, France, 2017, slides

86. M. Teklishyn, O. Vasylyev, and G. Sindhu, Assembly, integration, and testing of the CBM STS half-unit, CBM STS technical note (ongoing), 2025.

87. O. Vasylyev, Building blocks of the STS and its upgradability, STS Collaboration Meeting, GSI Helmholtz Centre for Heavy Ion Research, WUT, Warsaw, 11 October 2022, slides

88. J. M. Heuser, The Silicon Tracking System of the CBM experiment at FAIR, CBM Collaboration, QM 2017, GSI, Darmstadt, poster

89. I. Elizarov et al., Large-Scale Comprehensive Thermal Simulation of the CBM Silicon Tracking System (STS), CBM Collaboration, GSI, 2024, slides

90. K. Agarwal et al., Progress towards the development of cooling demonstrator for the STS detector of the CBM experiment at FAIR, CBM Progress Report 2019, paper

91. Agarwal, K., et al (2016). Development of a CO2-based cooling demonstrator for the CBM - Silicon Tracking System (Tech. Rep.). CBM Progress Report 2016.

92. J. Lehnert et al., GBT-based readout in the CBM experiment, Topical Workshop on Electronics for Particle Physics, KIT, Karlsruhe, Germany, 2016, paper

93. J. Lehnert, The GBT-based readout concept for the Silicon Tracking System of the CBM experiment, GSI, Darmstadt, 2015, paper

94. CERN, FEASTMP: Radiation and magnetic field tolerant 10 W DC/DC converter module, Geneva, Switzerland, 2016, datasheet

95. Private Conversation with Joerg

96. A. Lymanets et al., Power board v4 for the STS, GSI, Darmstadt, Germany, from pages 49–50, report

97. Sumida FLEXCON, PANTA® FIX POWER technical datasheet, https://sumida-flexcon.com/en-gb/products/panta-fix-jumper-panta-fix-power-jumper-7141523/

98. 3D-printed components provided by O. Vasylyev, 2025, used in this work.